Title
Spectroscopic Studies of the Primary Photochemical Dynamics of Phytochrome Cph1 and Rhodopsin

Author
Spillane, Katelyn Marie

Publication Date
2011

Peer reviewed|Thesis/dissertation

Spectroscopic Studies of the Primary Photochemical Dynamics of Phytochrome Cph1 and Rhodopsin

by

Katelyn Marie Spillane

A dissertation submitted in partial satisfaction of the

requirements for the degree of

Doctor of Philosophy

in

Chemistry

in the

Graduate Division

of the

University of California, Berkeley

Committee in charge:

Professor Richard A. Mathies, Chair
Professor Graham R. Fleming
Professor Roger Falcone

Spring 2011

Spectroscopic Studies of the Primary Photochemical Dynamics of Phytochrome Cph1 and Rhodopsin

Katelyn Marie Spillane

Abstract

Spectroscopic Studies of the Primary Photochemical Dynamics of Phytochrome Cph1 and Rhodopsin

by

Katelyn Marie Spillane

Doctor of Philosophy in Chemistry

University of California, Berkeley

Professor Richard A. Mathies, Chair

Biological photoreceptors are molecules that harvest light and convert it into chemical energy, ultimately driving a physiological response. They typically consist of a protein moiety and a strongly light-absorbing chromophore, and respond to the absorption of a photon with an elementary chemical reaction such as electron/proton transfer or *cis-trans* isomerization. The process of light-information conversion is of fundamental importance in biology, but it is not well understood at the molecular level. In this dissertation I investigate the primary photochemistry of two important photoreceptors, phytochrome Cph1 and rhodopsin. Although these proteins vary greatly in composition, architecture and function – phytochrome Cph1 drives a phototactic response in the cyanobacterium *Synechocystis* and rhodopsin initiates the visual process in vertebrates – they both respond to light stimuli through the isomerization of a carbon-carbon double bond in a covalently bound, extended conjugated chromophore. The primary purpose of my study is to understand the mechanism of the initial photoisomerization event that harnesses light energy for the purpose of driving biological function.

In my primary study, resonance Raman intensity analysis is used to investigate the structure and excited-state dynamics of the P_r and P_{fr} forms of phytochrome Cph1. I have accurately modeled the experimental absorption spectra of each conformer with a unique set of vibronic parameters, showing that both P_r and P_{fr} are structurally homogeneous in the ground state. The excited-state dynamics of the bilin chromophore are interesting because, although the low fluorescence quantum yield ($\phi_f < 10^{-3}$–10^{-4}) suggests fast excited-state dynamics, the isomerization is relatively slow (~1-3 ps) and inefficient ($\phi \sim 0.15$). I investigate this discrepancy and find that, although torsional Franck-Condon analysis predicts a <200 fs *Z*/*E* isomerization for both the $P_r \rightarrow P_{fr}$ and $P_{fr} \rightarrow P_r$ reactions, the reaction does not proceed as rapidly as predicted due to steric interaction between the D-ring of the chromophore and the protein.

In collaboration with researchers at Politecnico di Milano, Università di Bologna, Universität Duisburg-Essen, and The University of Oxford, we investigated the 11-*cis* → all-*trans* isomerization of rhodopsin using ultrafast pump-probe spectroscopy with sub-20-fs time resolution and a spectral coverage from the visible to the near-infrared. We tracked the coherent wavepacket motion from the initial photoexcited state to the

photoproduct and observed a pattern consistent with the presence of a conical intersection. During the first ~80 fs, we observed the loss of stimulated emission from the reactant and a decrease in the energy gap as the ground- and excited-state potential energy surfaces approached each other. Once the molecules pass through the conical intersection, we saw the rise of photoproduct absorption and an increase in the probed energy gap. These results provide the first experimental observation of a conical intersection in the unique reactivity of rhodopsin.

These studies demonstrate that although phytochrome Cph1 and rhodopsin are very different proteins, their primary photochemistry is surprisingly similar. By responding to light stimuli through the isomerization of a carbon-carbon double bond, they are able to very efficiently mediate light-information conversion for the purpose of driving biological function.

To mom and dad –
I couldn't be more grateful or proud to be your daughter

Table of Contents

List of Figures

List of Tables

Acknowledgments

I would like to start by acknowledging the people who sparked my initial interest in chemistry: Professors David L. Adams, Gregory N. Tew, and Scott M. Auerbach. Professor Adams was my first chemistry instructor at UMass Amherst, and his love and enthusiasm for the subject were contagious. He was a truly exceptional teacher, and it was because of him that I decided to become a scientist. Greg was my first research advisor, and I couldn't have asked for a better one. The three years I spent working in his lab were a truly wonderful time for me. I owe my sincerest thanks to Scott, a great PChem teacher who is, more importantly, a mentor and friend. He has supported me over the years by offering a kind ear and much needed advice, and even a push in the right direction when necessary. I have leaned on him during some very difficult times and I credit him with keeping me in graduate school.

I am grateful to my graduate research advisor, Professor Richard A. Mathies, for teaching me how to approach scientific problems, think critically, and write clearly and straightforwardly. His enthusiasm for uncovering scientific truth and his high standard for thoroughness and quality of research are inspiring. I also owe a great deal of thanks to Mary Hammond who, in addition to keeping the lab running smoothly, has always found time in her hectic day to provide assistance and support. She has given me a lot of advice and perspective over the past four and a half years, for which I am so thankful.

While at Berkeley I have had the opportunity to work with a group of very talented scientists. In particular, I would like to acknowledge Dr. Jyotishman Dasgupta, both for his friendship and for his contribution to the phytochrome project. Our scientific discussions are always exciting and thought provoking, and I am a much better scientist because of them. I must also acknowledge my co-authors for the work presented in this dissertation. In addition to JD, they are: J. Clark Lagarias, Dario Polli, Piero Altoè, Oliver Weingart, Cristian Manzoni, Daniele Brida, Gaia Tomasello, Giorgio Orlandi, Philipp Kukura, Marco Garavelli and Giulio Cerullo. It has been a pleasure to work with my Raman side labmates: Christina Stuart, Renee Frontiera, Mark Creelman, Dan Wandschneider, Rosalie Tran, David Hoffman, Ryan Leverenz, Sangdeok Shim, Chong Fang and Tomotsumi Fujisawa.

On a more personal note, I would like to thank Ashley Russell, who is the best friend a girl could ask for. We have had a lot of fun together over the past several years, and it is because of her that I have maintained a life outside the lab. Then there is Mark Crimmin, who brings so much joy to my life. I couldn't ask for a better partner, and I look forward to our post-Berkeley life together.

Finally, I would like to acknowledge the people who made this all possible. I really do have the best family imaginable. They are my safety net, giving me the courage to take risks I otherwise wouldn't because I know they will be there to support me no matter what. My parents have worked so hard to give my siblings and me every opportunity, and I could never fully express my gratitude. My sisters and brother are equally supportive, and never fail to make me laugh with a well-timed joke, which is often at my own expense. To Grandma, Grandpa, Meme, and the rest of my extended family, thank you for always welcoming me home with open arms and humoring me

while I told you all about my latest adventures in the lab. Last, but certainly not least, I couldn't have done this without Papa. He has always challenged me intellectually and inspired me to be the best person I could be, both academically and otherwise. Although he never got to see this final product, I know he would be proud.

Chapter 1
Introduction

1.1 Motivation

Light plays a fundamentally important role in biology. Nearly all life on earth draws energy from sunlight, either directly in the case of photosynthetic organisms or indirectly through the consumption of food. Living organisms have evolved to detect, interpret and respond to light in order to maximize their chances of survival. In the case of plants, this is reflected in growth and development; in the case of humans, this is demonstrated in our ability to see, and therefore respond to, our environment.

Biological photoreceptors are molecules that harvest light and convert it into chemical energy, ultimately driving a physiological response. They typically consist of a protein moiety and a strongly light-absorbing chromophore, but the composition, architecture and function of different photoreceptors vary greatly. Regardless, the methods of light-energy conversion in these systems are surprisingly similar. The light receptors and their environments are specifically designed so that the desired molecular response occurs on the picosecond or sub-picosecond timescale, which is orders of magnitude faster than competing relaxation and energy dissipation processes, and along the reaction pathway that triggers the desired physiological response. Upon absorption of light, the chromophore undergoes a change in structural configuration that communicates the information gained from photon absorption to a downstream signal transduction partner. The primary photochemistry is typically an elementary chemical reaction such as electron/proton transfer or *cis-trans* isomerization, and the nature of these reactions generally makes them very fast and efficient. Because the activation of a biological response is the result of a photophysical process, living organisms can adjust to their environmental conditions by continuously reading and responding to external light signals. In order to understand the complex relation between photon absorption and the triggering of a biological response, it is necessary to determine the structural changes immediately following light activation.

This thesis focuses on the primary photochemical events in two photoreceptors: phytochrome Cph1 and rhodopsin. Although these proteins serve very different functions – phytochrome Cph1 drives a phototactic response in the cyanobacterium *Synechocystis* and rhodopsin initiates the visual process in vertebrates – they both respond to light stimuli through the isomerization of a carbon-carbon double bond in a covalently bound, extended conjugated chromophore. The primary purpose of this study is to understand the role of the initial photoisomerization event in harnessing light energy for the purpose of driving biological function.

1.2 The Phytochrome Photoreceptor

Organisms that rely directly on sunlight for energy must be able to monitor and adjust to a continuously changing light environment. Photosynthetic organisms possess numerous photoreceptors for the perception of and adaptation to fluctuation in light intensity, duration, direction, polarization and spectral quality. The most well known of these photoreceptors are phytochromes, which were first discovered in plants [1]. Phytochromes sense ambient light conditions by their ability to photoconvert between red (P_r) and far-red absorbing (P_{fr}) forms, and this sampling of the light environment is responsible for triggering an array of developmental functions such as photomorphogenesis and shade avoidance. Phytochromes have also been found in cyanobacteria, nonoxygenic bacteria and fungi, demonstrating that this class of photoreceptors is not limited to photosynthetic organisms [2,3].

All phytochromes utilize covalently attached bilin chromophores that enable photoconversion between the P_r and P_{fr} forms. The exact nature of the chromophore varies for different subfamilies of phytochrome – plant phytochromes use phycochromobilin (PΦB) and cyanobacterial phytochromes use phycocyanobilin (PCB) – but in all cases, upon light absorption the bilin undergoes *Z/E* isomerization about the C_{15}=C_{16} bond between the C and D tetrapyrrole rings (Figure 1.1) [4]. The chromophore is buried deep within the GAF domain, which together with the PAS domain forms the chromophore binding pocket (Figure 1.2). This structure serves to limit the flexibility of the molecule during photoisomerization, restricting the chromophore to the biologically desirable reaction pathway.

The photochemical reaction scheme for phytochrome is shown in Figure 1.3. Illumination of P_r with red light produces lumi-R as the primary photoproduct, which is subsequently converted to P_{fr} via multiple light-independent steps. P_{fr} can be converted into P_r either by illumination with far-red light, producing lumi-F and then P_r via subsequent thermal steps, or by an entirely thermal process known as dark reversion. Ultrafast pump-probe electronic spectroscopy has been used to study the photochemical dynamics of the phytochrome photocycle, showing that the *Z*-to-*E* isomerization takes place in ~3 ps (ϕ ~ 15%) [6-8] while the *E*-to-*Z* isomerization occurs in ~700 fs (ϕ ~ 15%) [8-10]. Two excited-state intermediates (I* and Lumi-R*) have been identified in the $P_r \rightarrow P_{fr}$ conversion, leading to the first ground-state photoproduct Lumi-R. For the $P_{fr} \rightarrow P_r$ reaction, at least three kinetic components have been observed, but the intermediate and photoproduct states remain poorly characterized [9]. Dasgupta et al.

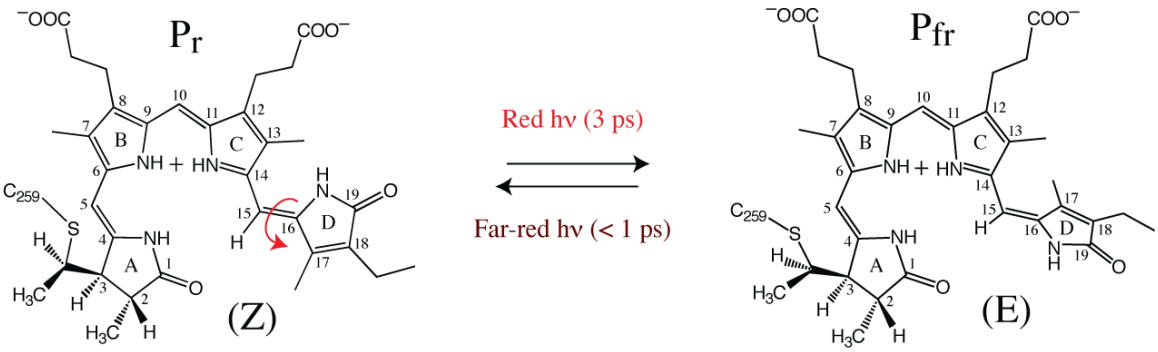

Figure 1.1. Structural changes of the bilin chromophore during the P_r-to-P_{fr} photocycle in phytochrome. The ground-state P_r chromophore structure is depicted as *ZZZ*ssa at the AB, BC and CD rings, respectively. Photoexcitation results in isomerization of the C_{15}=C_{16} methine bridge between the C and D rings, yielding the red-shifted *ZZE*ssa product P_{fr}.

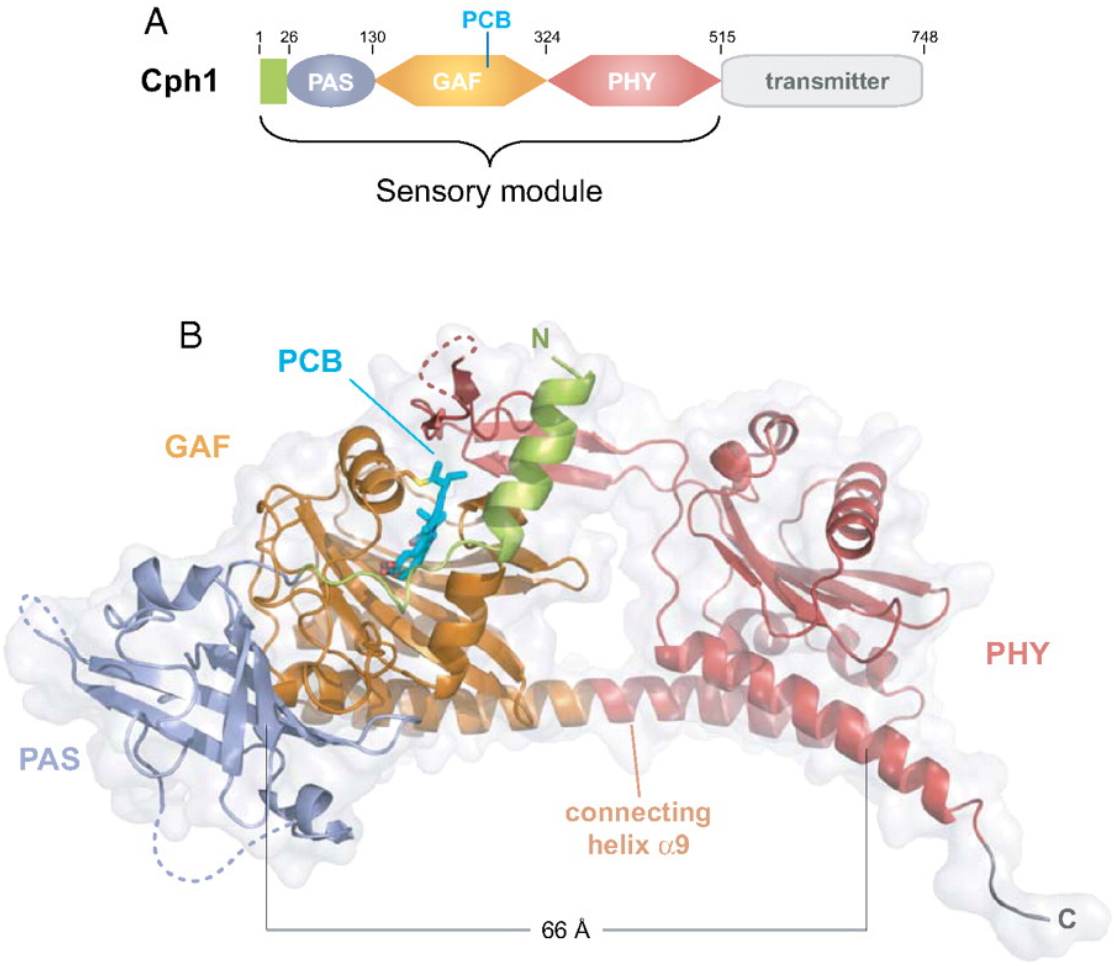

Figure 1.2. Structure and spectral characteristics of the Cph1 phytochrome sensory module from *Synechocystis* 6803. (A) Domain boundaries of Cph1 phytochrome. (B) Ribbon representation of the sensory module structure showing the N-terminal α-helix (green) and PAS (blue), GAF (orange) and PHY (red) domains. The PCB chromophore (cyan) is covalently attached to Cys-259. (Figure from Essen et al. [5])

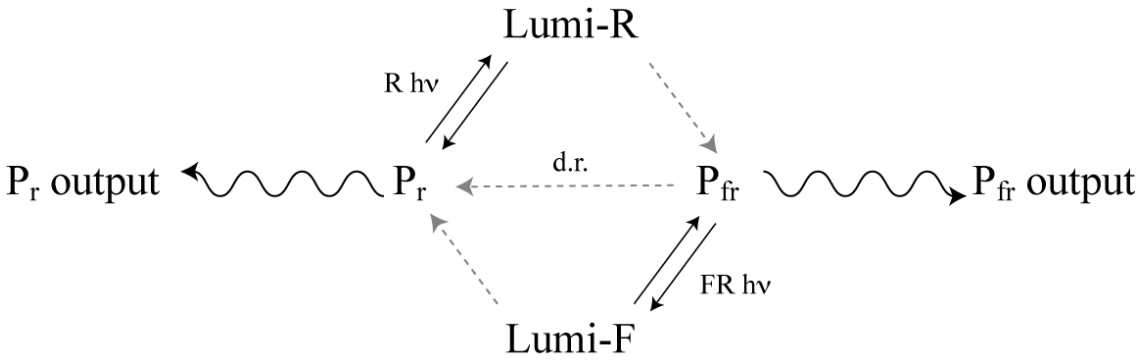

Figure 1.3. The phytochrome photocycle. Illumination of P_r phytochrome with red light (R) produces lumi-R as the primary photoproduct. This is subsequently converted to P_{fr} via multiple light-independent steps. P_{fr} can be converted into Pr either by illumination with far-red light (FR), producing lumi-F and then P_r via subsequent thermal steps, or by an entirely thermal process known as dark reversion (d.r.).

recently used femtosecond stimulated Raman spectroscopy to show that the P_r form of phytochrome Cph1 isomerizes on the excited state, forming the first formally isomerized excited-state intermediate Lumi-R* by 3 ps [6], but the first isomerized intermediate in the $P_{fr} \rightarrow P_r$ reaction has not yet been identified.

A second major point currently under investigation is the ground-state structural composition of the P_r and P_{fr} chromophores. The multiple excited-state lifetimes [9,11] and the presence of a distinct shoulder on the blue edge of the electronic absorption profiles (Figure 1.4) [12-14] have been interpreted by some as evidence of multiple ground-state populations. Also, using magic-angle spinning NMR spectroscopy, Song et al. recently concluded that the P_r ground state consists of two distinct isoforms that havedifferent hydrogen bonding networks in the chromophore binding domain [15]. However, Dasgupta found that the P_r structural dynamics are consistent with a homogeneous branching mechanism on the excited-state surface and saw no evidence of chromophore heterogeneity [6].

In order to more fully understand the phytochrome photocycle, it is necessary to examine the molecular structure of the bilin chromophore with a high-resolution structural technique. Resonance Raman (RR) spectroscopy is particularly well suited for this task as it can simultaneously provide structural and dynamical information about a molecule. RR exploits the resonance enhancement that arises when the excitation wavelength falls within or near an electronic absorption band, which is particularly useful when studying a chromophore embedded within a protein. While the vibrational frequencies of the Raman bands provide detailed information about the ground-state molecular structure, the Raman band intensities are indicative of the initial excited-state dynamics in the Franck-Condon region [16]. The excited-state dynamical information is obtained from RR intensity analysis, which involves modeling the electronic absorption spectrum and RR cross-sections to produce a model of the excited-state potential energy surface. The intensity of a mode is directly proportional to the square of the slope of the excited-state potential energy surface, suggesting faster dynamics along particular vibrational coordinates. Given that the timescale of RR scattering is limited by the electronic dephasing of a molecule [17], which is on the order of tens of femtoseconds [18], RR spectroscopy is a useful method for probing very early-time excited-state dynamics that are still not routinely accessible by ultrafast techniques. Thus, information gained from RR spectroscopy is complementary to the best time-resolved techniques currently available.

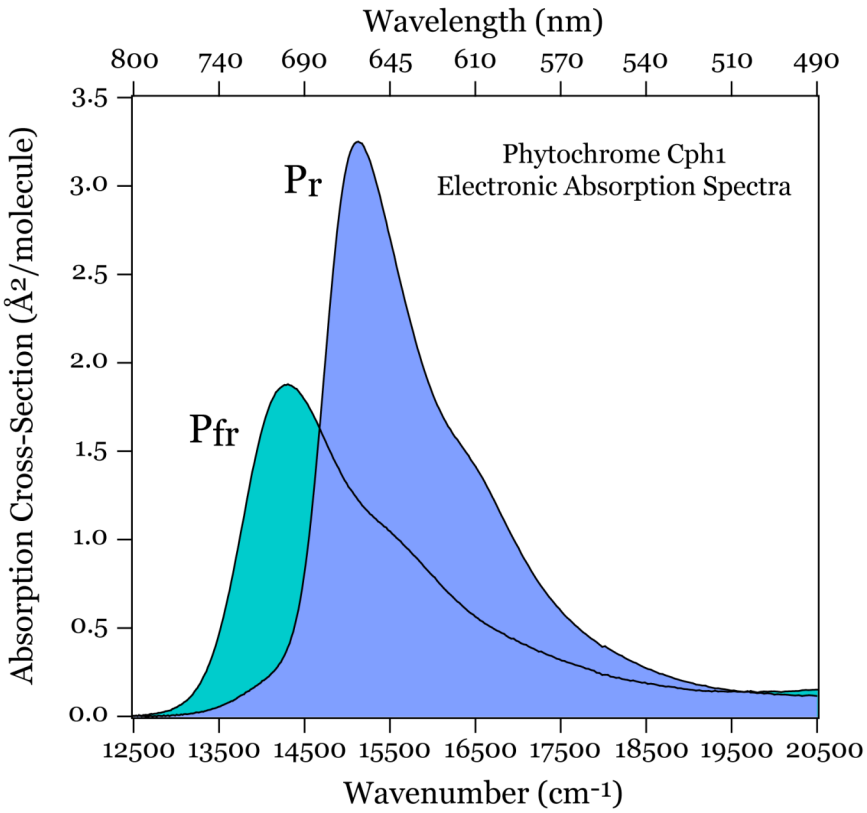

Figure 1.4. Electronic absorption spectra of the P_r and P_{fr} forms of phytochrome Cph1 at 295 K.

1.3 Rhodopsin: The Vertebrate Visual Pigment

The visual process in vertebrates is initiated by two types of photoreceptor cells: cones and rods. Cones function at high light levels, providing detailed spatial and temporal information as well as the perception of color [19]. As the light level decreases, vision switches from photopic to scotopic, which is produced exclusively in the rod cells (Figure 1.5). Rhodopsin is the photosensitive protein responsible for dim-light vision. It is a 41-kDa integral membrane protein comprising 348 amino acids residues. It belongs to the large family of G-protein coupled receptors (GPCRs), which facilitate communication between a cell and its environment through a GTP-activated heterotrimeric G-protein [20].

Rhodopsin consists of the opsin apoprotein and the 11-*cis* retinal chromophore which is covalently bound to opsin via a protonated Schiff base linkage with Lysine 296. All known visual pigments utilize the 11-*cis* retinal chromophore or a closely related derivative, making retinal universal among imaging photoreceptors [21]. The visual process in rhodopsin begins with the absorption of a visible photon, at which point the chromophore isomerizes to the all-*trans* form. Over 60% of the incident energy is stored in the first thermally stable, all-*trans* photoproduct bathorhodopsin, and this energy is used to drive subsequent structural changes that eventually result in visual sensation [22].

The photobleaching intermediates and their structures are shown in Figure 1.6. Meta II is the signaling state that causes rhodopsin to interact with the G-protein transducin, which initiates the neural response. Each Meta II molecule activates ~500 transducin molecules, which in turn initiate an enzymatic cascade which ultimately results in hyperpolarization of the rod cell [24]. This amplification process results in ultimate sensitivity – a rod cell in the human retina is capable of discerning a *single photon* [25]. Meta II is deactivated upon the phosphorylation of rhodopsin and subsequent binding of arrestin [26]. At this stage, the chromophore is converted to all-*trans* retinal and released from the protein. The orientation of rhodopsin, transducin and the membrane are shown in Figure 1.7.

The primary photochemical event in vision is truly remarkable: the 11-*cis* → all-*trans* isomerization occurs within only 200 fs [27] with a high quantum yield of 0.65 [28], and 60% of the input photon energy (~35 kcal/mol for a 500 nm photon) is stored in the first stable bathorhodopsin intermediate. This suggests an unusually fast and efficient photoactivated one-way reaction that has been of great interest to researchers since its discovery in 1963 [29]. Rhodopsin's unique reactivity is generally attributed to a conical intersection between the potential energy surfaces of the ground and excited electronic states, which enables efficient and ultrafast conversion of photon energy into chemical energy. Experimental evidence of a conical intersection has escaped researchers, however, due to the difficulty of probing the energy gap between the electronic states of the reacting molecule on an ultrashort timescale. The observation of the conical intersection in rhodopsin thus requires a spectroscopic technique that combines high temporal resolution with a broad spectral window that extends into the near-infrared region.

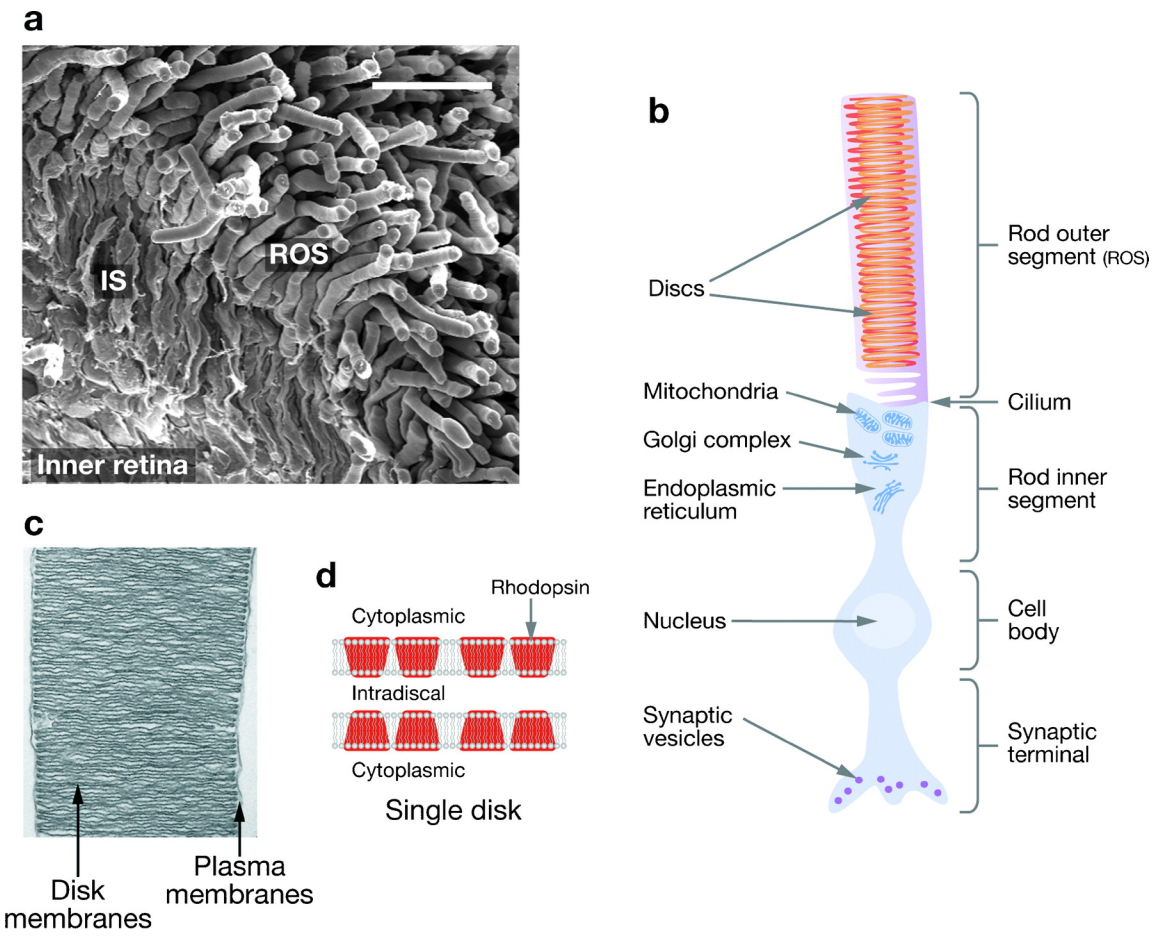

Figure 1.5. Vertebrate retina and rod cell. (a) Scanning electroretinogram of mouse retina. (b) Diagram depicting the rod cell. (c) Electron micrograph of isolated ROS from the mouse retina. (d) Diagram of disk membranes. (Figure from Palczewski [23])

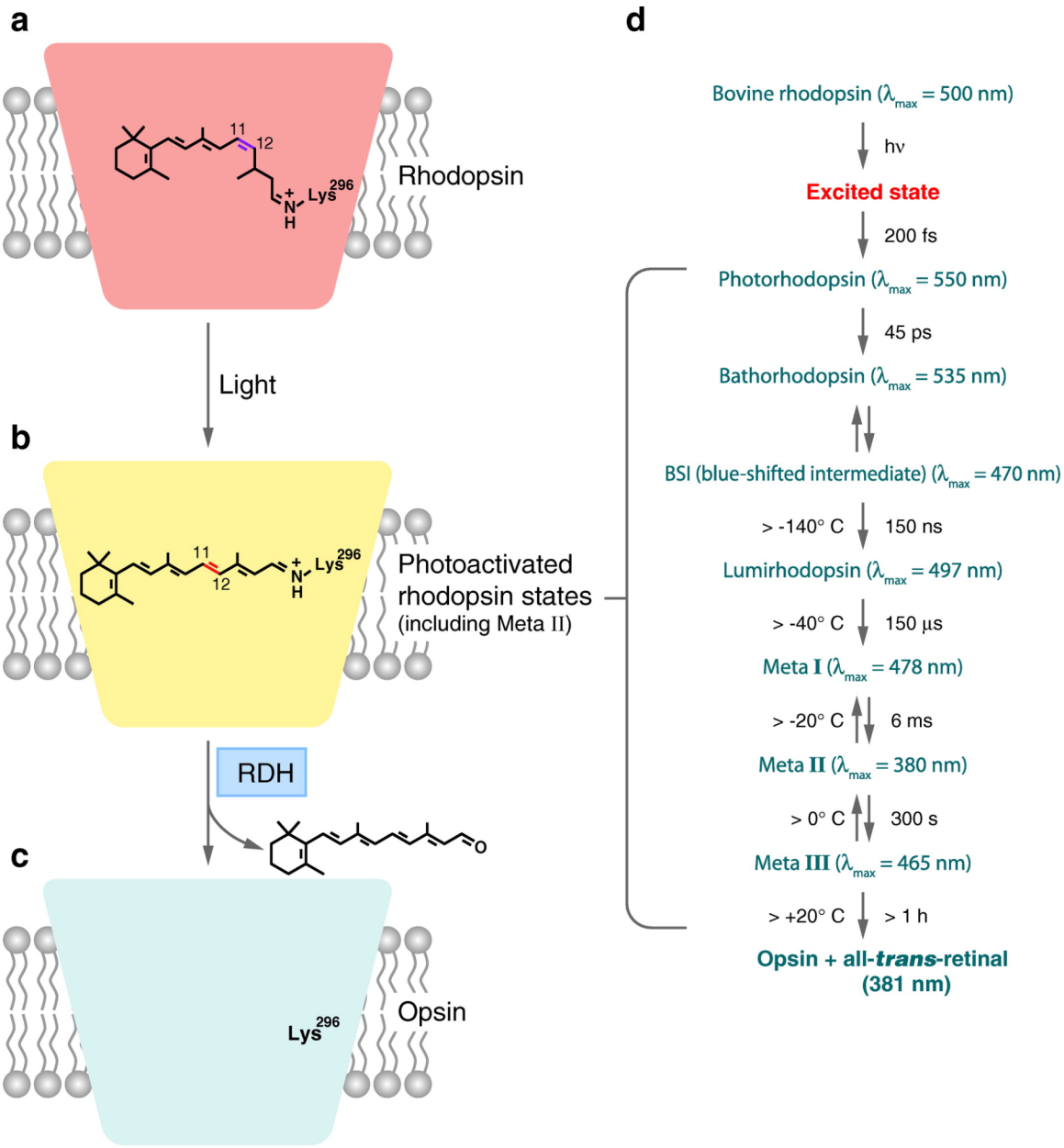

Figure 1.6. Light cycle of rhodopsin. (a) Rhodopsin and 11-*cis* retinal. (b) Photoactivated rhodopsin, showing the multiple intermediates that culminate in the formation of the G protein–activating state, Meta II. (c) Opsin without chromophore. (d) Reaction scheme of rhodopsin photoactivation. On the left are maximal temperatures at which indicated intermediates can be trapped, and on the right is time required for that particular transformation. In the brackets are λ_{max} of absorption for different intermediates. (Figure from Palczewski [23])

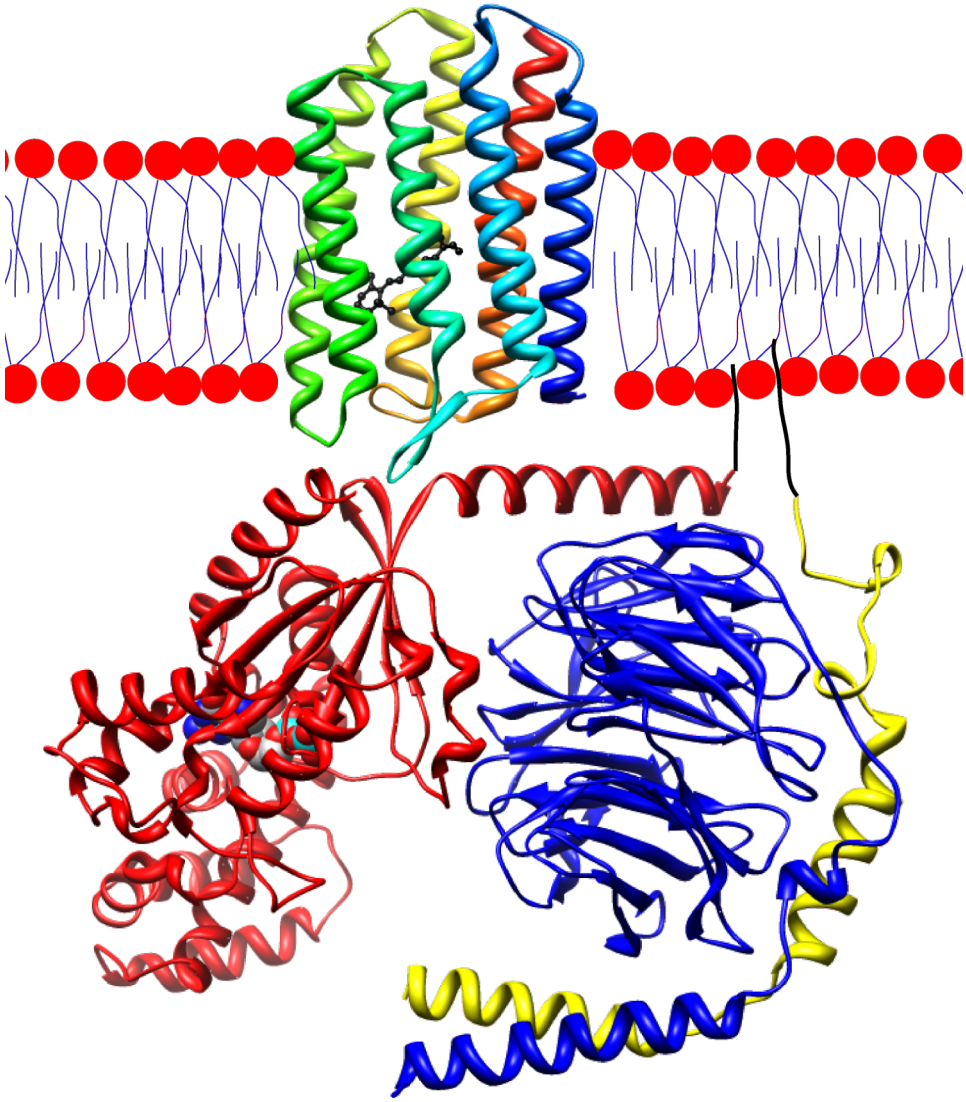

Figure 1.7. Orientation of rhodopsin, transducin, and the membrane. Rhodopsin is embedded in the membrane with the N-terminus colored red and the C-terminus blue. The retinal chromophore (black) is embedded in the protein. Transducin is below the membrane.

The primary focus of this thesis is the relationship between molecular structure and isomerization dynamics in the extended conjugated chromophores of rhodopsin and phytochrome Cph1. In Chapters 3 and 4, I use RR intensity analysis to analyze the ground-state composition of the P_r and P_{fr} chromophores in phytochrome Cph1. In addition, the RR intensity analysis of the early-time (0-50 fs) structural dynamics reveals the multidimensional nature of the initial photochemical dynamics in phytochrome. In Chapter 5, ultrafast pump-probe spectroscopy is used to monitor rhodopsin photochemistry from 0-300 fs, revealing the crossing of the wavepacket through the conical intersection to the ground-state photoproduct.

1.4 Outline

The experimental and theoretical methods used in the studies presented in this thesis are reviewed in Chapter 2. This chapter presents an overview of resonance Raman intensity analysis using the time-dependent wavepacket formalism as described by Heller [19]. I discuss in detail the quantification of absolute Raman cross-sections and excited-state normal mode displacements for each Raman-active mode, as well as the distribution of broadening effects into homogeneous and inhomogeneous contributions. Also included is the method for isolating and purifying rhodopsin samples from bovine retinas.

I apply resonance Raman intensity analysis to the study of the P_r form of phytochrome Cph1 in Chapter 3. The absorption spectrum of P_r has a maximum at 660 nm and a distinct shoulder on the blue edge at ~620 nm, and many have assigned this feature to a second conformer in the ground state. By performing a full vibronic analysis I show instead that the shoulder is caused by the 0–1 vibronic transition, indicating that P_r ground-state population is homogeneous. This finding is of fundamental importance in elucidating the photochemical reaction pathway because it supports a homogeneous branching mechanism on the excited-state surface.

The work on phytochrome Cph1 continues in Chapter 4 with a Franck-Condon analysis of the P_{fr} form. From this analysis I show that P_{fr} also exists as a single species in the ground state. The Franck-Condon displacements of both the P_r and P_{fr} forms reveal the initial atomic motions in the excited state, and hence the initial photochemical dynamics. I show that the bilin chromophore has fast torsional Franck-Condon dynamics that predict a ~200 fs isomerization time, but non-bonded interactions in the chromophore binding pocket prevent the D-ring from rotating on that timescale. As a result, the phytochrome *Z*/*E* isomerizations occur in ~1-3 ps with a low quantum yield of 15% due to the relatively long time required to reach the conical intersection. This is in contrast to rhodopsin, in which an unhindered reaction pathway allows fast Franck-Condon dynamics to carry the 11-*cis* retinal chromophore directly to the conical intersection in only 200 fs.

In Chapter 5, in collaboration with researchers at Polytechnic di Milano, Universita di Bologna, Universität Duisburg-Essen, Max Planck Institute and The University of Oxford, we investigate rhodopsin photoreceptor chemistry beyond the Franck-Condon region by using ultrafast pump-probe spectroscopy to track the coherent wavepacket motion from the initial photoexcited state to the photoproduct. By monitoring

the loss of reactant emission and the subsequent appearance of photoproduct absorption, we provide the most compelling evidence to date for the existence and importance of conical intersections in visual photochemistry.

Finally, Chapter 6 summarizes the contributions of this dissertation and presents recommendations for future studies to further elucidate the mechanism of light-energy conversion in phytochromes and rhodopsin.

1.5 References

[1] W. L. Butler, K. H. Norris, H. W. Siegelman and S. B. Hendricks, *Proc. Natl. Acad. Sci. U.S.A.* **45,** 1703 (1959).

[2] L. H. Pratt, *Photochem. Photobiol.* **61,** 10 (1995).

[3] B. L. Montgomery and J. C. Lagarias, *Trends Plant Sci.* **7,** 357 (2002).

[4] L. Taiz and E. Zeiger, *Plant Physiology* (Sinauer Associates, Inc., Sunderland, MA, 2010), 5th ed.

[5] L. –O. Essen, J. Mailliet and J. Hughes, *Proc. Natl. Acad. Sci. U.S.A.* **105,** 14709 (2008).

[6] J. Dasgupta, R. R. Frontiera, K. C. Taylor, J. C. Lagarias and R. A. Mathies, *Proc. Natl. Acad. Sci. U.S.A.* **106,** 1784 (2009).

[7] J. J. van Thor, K. L. Ronayne and M. Towrie, *J. Am. Chem. Soc.* **129,** 126 (2007).

[8] T. Lamparter, F. Mittmann, W. Gärtner, T. Börner, E. Hartmann and J. Hughes, *Proc. Natl. Acad. Sci. U.S.A.* **94,** 11792 (1997).

[9] M. Bischoff, G. Hermann, S. Rentsch and D. Strehlow, *Biochemistry* **40,** 181 (2001).

[10] M. Bischoff, G. Hermann, S. Rentsch and D. Strehlow, *J. Phys. Chem. A* **102,** 4399 (1998).

[11] A. R. Holzwarth, E. Venuti, S. E. Braslavsky and K. Schaffner, *Biochim. Biophys. Acta* **1140,** 59 (1992).

[12] J. B. Nieder, M. Brecht and R. Bittl, *J. Am. Chem. Soc.* **131,** 69 (2009).

[13] P. Schmidt, T. Gensch, A. Remberg, W. Gärtner, S. E. Braslavsky and K. Schaffner, *Photochem. Photobiol.* **68,** 754 (1998).

[14] D. von Stetten, M. Gü nther, P. Scheerer, D. H. Murgida, M. A. Mroginski, M. Krauβ, T. Lamparter, J. Zhang, D. M. Anstrom, R. D. Vierstra, K. T. Forest and P. Hildebrandt, *Angew. Chem. Int. Ed.* **47,** 4753 (2008).

[15] C. Song, G. Psakis, C. Lang, J. Mailliet, W. Gärtner, J. Hughes and J. Matysik, *Proc. Natl. Acad. Sci. U.S.A.* **108,** 3842 (2011).

[16] A. B. Myers and R. A. Mathies, in *Biological Applications of Raman Spectroscopy*; T. G. Spiro, Ed. (John Wiley & Sons, New York, 1987), Vol. 2, p. 1.

[17] L. D. Ziegler, *Acc. Chem. Res.* **27,** 1 (1994).

[18] M. K. Lawless and R. A. Mathies, *J. Chem. Phys.* **96,** 8037 (1992).

[19] M. Livingstone and D. Hubel, *Science* **240,** 740 (1988)

[20] E. J. M. Helmreich and K. P. Hofmann, *Biochim. Biophys. Acta* **1286,** 285 (1996).

[21] W. Gärtner and P. Towner, *Photochem. Photobiol.* **62,** 1 (1995).

[22] A. Cooper, *Nature* **282,** 531 (1979).

[23] K. Palczewski, *Annu. Rev. Biochem.* **75,** 743 (2006).

[24] G. L. Zubay, *Biochemistry* (Addison-Wesley, Reading, MA, 1983) 3rd ed.

[25] R. Zuckerman, G. J. Schmidt and S. M. Dacko, *Proc. Natl. Acad. Sci. U.S.A.* **79,** 6414 (1982).

[26] N. Bennett and A. Sitaramayy, *Biochemistry* **27,** 1710 (1988).

[27] R. W. Schoenlein, L. A. Peteanu, R. A. Mathies and C. V. Shank, *Science* **254,** 412 (1991).

[28] J. E. Kim, M. J. Tauber and R. A. Mathies, *Biochemistry* **40,** 13774 (2001).

[29] T. Yoshizawa and G. Wald, *Nature* **197,** 1279 (1963).

[30] S. Y. Lee and E. J. Heller, *J. Chem. Phys.* **71,** 4777 (1979).

Chapter 2
Experimental and Theoretical Methods

2.1 Resonance Raman intensity analysis

Resonance Raman spectroscopy is a powerful method for studying the vibrational structure and dynamics of a molecule. When the excitation wavelength falls within an electronic absorption band, scattering from the absorbing species is selectively enhanced. This allows the direct probing of a chromophore without interference from the solvent or surrounding non-resonant molecules. The Raman spectrum provides detailed information about the ground-state geometry and can also provide structural snapshots of a chromophore as it evolves along a reaction coordinate. The Raman line intensities give information about the molecular evolution on the excited state; those bands in a resonance Raman spectrum that are intense correspond to nuclear coordinates along which the electronically excited molecule rapidly distorts. This is particularly pertinent for ultrafast reactions, as initial movement out of the Franck-Condon region is likely along the reaction coordinate. Given that the timescale of resonance Raman scattering is limited by the electronic dephasing of a molecule [1], and this dephasing is on the order of tens of femtoseconds [2], resonance Raman spectroscopy is a useful method for probing very early-time excited-state dynamics that can be difficult or impossible to observe with other experimental techniques.

The above-described information can be gained through resonance Raman intensity analysis using the time-dependent wavepacket formalism as described by Heller and shown schematically in Figure 2.1 [3]. This analysis involves the simultaneous modeling of the absorption profile and resonance Raman cross-sections of the molecule. In the harmonic approximation, this yields the dimensionless excited-state displacement, Δ, in each Raman-active mode. These Δ values, in turn, reveal the slopes of the harmonic excited-state surfaces in the Franck-Condon region, where the slope of the potential energy surface is $\hbar\omega\Delta$. In addition, the distribution of broadening effects into homogeneous and inhomogeneous contributions can be discerned.

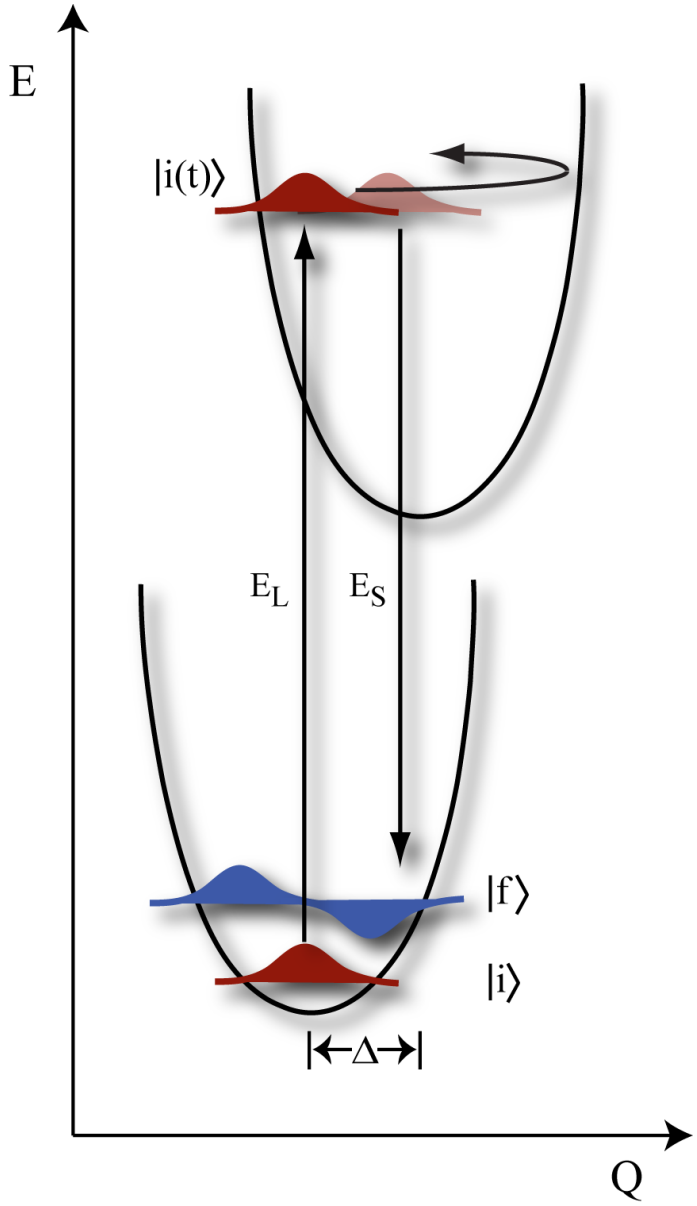

Figure 2.1 Schematic of the time-dependent wavepacket overlap and vibronic coupling in resonance Raman scattering. The unitless displacement, Δ, represents the shift in the harmonic minimum of the excited state relative to the harmonic minimum of the ground state potential energy surface along the normal coordinate, Q. E_L and E_S represent the excitation and scattering photon energies, respectively.

The absorption cross-section, σ_A, is determined by the Fourier transform of $\langle i|i(t)\rangle$, where $|i\rangle$ is the initial vibrational wavefunction on the ground electronic surface and $|i(t)\rangle = e^{i\hat{H}t/\hbar}|i\rangle$ is the projection of this initial wavefunction propagating on the excited electronic surface. The Raman cross-sections, σ_R, are determined by the square of the half Fourier transform of $\langle f|i(t)\rangle$, where $|f\rangle$ is the final vibrational wavefunction in the ground electronic state. In the case of harmonic ground- and excited-state surfaces that differ only in their equilibrium positions, the time-dependent equations for the absorption and Raman cross-sections are [4]:

$$\sigma_A = \frac{4\pi E_L e^2 M^2}{6\hbar^2 cn\left(\theta\sqrt{2\pi}\right)} \int_0^\infty \mathrm{dE} \exp\left[\frac{-\left(E-E_0\right)^2}{2\theta^2}\right] \int_{-\infty}^{\infty} dt \langle i|i(t)\rangle e^{-\Gamma_G^2 t^2/\hbar^2} e^{i(E_L+\varepsilon_i)t/\hbar} \qquad (2.1)$$

$$\sigma_R = \frac{8\pi E_S^3 E_L e^4 M^4}{9\hbar^6 c^4\left(\theta\sqrt{2\pi}\right)} \int_0^\infty \mathrm{dE} \exp\left[\frac{-\left(E-E_0\right)^2}{2\theta^2}\right] \left| \int_0^{\infty} dt \langle f|i(t)\rangle e^{-\Gamma_G^2 t^2/\hbar^2} e^{i(E_L+\varepsilon_i)t/\hbar} \right|^2 \qquad (2.2)$$

In the above expressions, E_0 represents the zero-zero transition energy (cm^{-1}), M is the transition length (Å), Γ_G is the Gaussian homogeneous linewidth (cm^{-1}) and θ is the inhomogeneous linewidth (cm^{-1}). If instead the homogenous linewidth should be modeled with a Lorentzian lineshape, the $e^{-\Gamma_G^2 t^2/\hbar^2}$ term is replaced with $e^{-\Gamma|t|/\hbar}$. The Raman intensity calculations presented in this thesis were performed using the program RRModel.f (written in Fortran 77), which was provided by Anne Myers Kelley from the University of California Merced (Appendix C). The program calculates absorption and Raman excitation profiles and is capable of including excited-state frequency changes and thermally populated states. To use the program, Δ values are initially estimated from the Raman spectrum by assuming that the integrated Raman intensity of each band is directly proportional to $\omega^2\Delta^2$ if short-time dynamics are expected, where ω is the vibrational frequency and Δ is the unitless normal mode displacement. The intensity is frequency-dependent in the short-time limit because lower frequency modes require more time for $\langle f|i(t)\rangle$ to reach maximal overlap. Thus, early truncation of this overlap (e.g., due to fast dynamics along a dissociative reaction coordinate) will result in lessened intensities for low frequency modes. Because the absorption profile contains underlying vibronic progressions, its breadth depends on the value of Δ, particularly in high-frequency modes. Delta values are scaled to fit the width of the absorption profile – delta values that are too large result in a calculated absorption profile that is too broad, whereas small delta values underestimate the breadth. Next, E_0 and M are adjusted to best fit the absorption peak frequency and amplitude, respectively, of the experimental absorption spectrum. The magnitude of the inhomogeneous broadening parameter determines the degree of vibronic structure present in the calculated absorption profile. The value of the homogeneous broadening parameter is adjusted to model the correct shape of the red edge of the absorption spectrum, and its magnitude is constrained by the absolute Raman cross-sections. Iterative adjustment of these parameters is performed until a good fit is

obtained for both the absorption spectrum and the Raman cross-sections. Additional notes on how to use the RRModel program are included in Appendix C.

2.2 Quantification of absolute Raman cross-sections

In the case of the phytochrome studies presented in Chapters 3 and 4, absolute Raman cross-sections were determined by comparing the integrated phytochrome peak areas to that of a known standard: the 1049 cm^{-1} NO_3^- symmetric stretch, which has a differential cross-section of $\partial\sigma_{std}/\partial\Omega$ = 10.9 × 10^{-30} cm^2 $molecule^{-1}$ sr^{-1} at 514.5 nm excitation [5]. This value is dependent on the excitation wavelength as shown in Figure 2.2 and defined by the Albrecht A term expression:

$$\frac{\partial\sigma_R}{\partial\Omega} = K_2\nu_0\left(\nu_0 - \nu_{mn}\right)^3\left[\frac{\nu_e^2 + \nu_0^2}{\left(\nu_e^2 - \nu_0^2\right)^2}\right]^2 \tag{2.3}$$

where, for nitrate, the constant K_2 is 1.56 × 10^{-28} cm^2 $molecule^{-1}$ sr^{-1} and the frequency of the transition to the resonant electronic excited state (ν_e) is 52,300 cm^{-1} [5]. In this expression, ν_{mn} represents the frequency of the vibrational band of interest and ν_0 represents the excitation frequency. Using this expression, the differential cross-section of the NO_3^- symmetric stretch at the excitation wavelength 790.4 nm was found to be 5.87 × 10^{-31} cm^2 $molecule^{-1}$ sr^{-1}.

Because nitrate can be damaging to a protein sample, the Raman cross-sections of phytochrome were compared indirectly to that of nitrate. To do this, the differential cross-section of the 1049 cm^{-1} nitrate symmetric stretch at 790.4 nm was used to determine that of the C–OH glycerol stretch at 790.4 nm, and then this value was used to determine the differential and absolute cross-sections of the phytochrome Raman bands. First, the integrated Raman peak areas of the nitrate symmetric stretch and the 1049 cm^{-1} glycerol C–OH stretch were compared directly in a TES–buffer solution containing 250 mM nitrate and 1.233 M glycerol. Because the Raman bands of interest directly overlap, the TES–glycerol buffer spectrum was measured separately and then subtracted to reveal the pure nitrate spectrum, as shown in Figure 2.3. Using Equation 2.4, the differential cross-section of the 1049 cm^{-1} C–OH glycerol stretch (λ_{ex} = 790.4 nm) was then determined to be 1.31 × 10^{-31} cm^2 $molecule^{-1}$ sr^{-1} from

$$\left(\frac{\partial\sigma_R}{\partial\Omega}\right) = \left(\frac{\nu_R}{\nu_{std}}\right)\frac{A_R}{A_{std}}\frac{c_{std}}{c_R}\left(\frac{\partial\sigma_{std}}{\partial\Omega}\right) \tag{2.4}$$

where ν_R and ν_{std} are the frequencies of the scattered photons, A_R and A_{std} are the integrated Raman peak areas, and c_R and c_{std} are the concentrations of glycerol and the nitrate standard, respectively.

By the same method, the differential cross-sections of the phytochrome bands were determined using the C–OH glycerol stretch as an internal standard. Figure 2.4

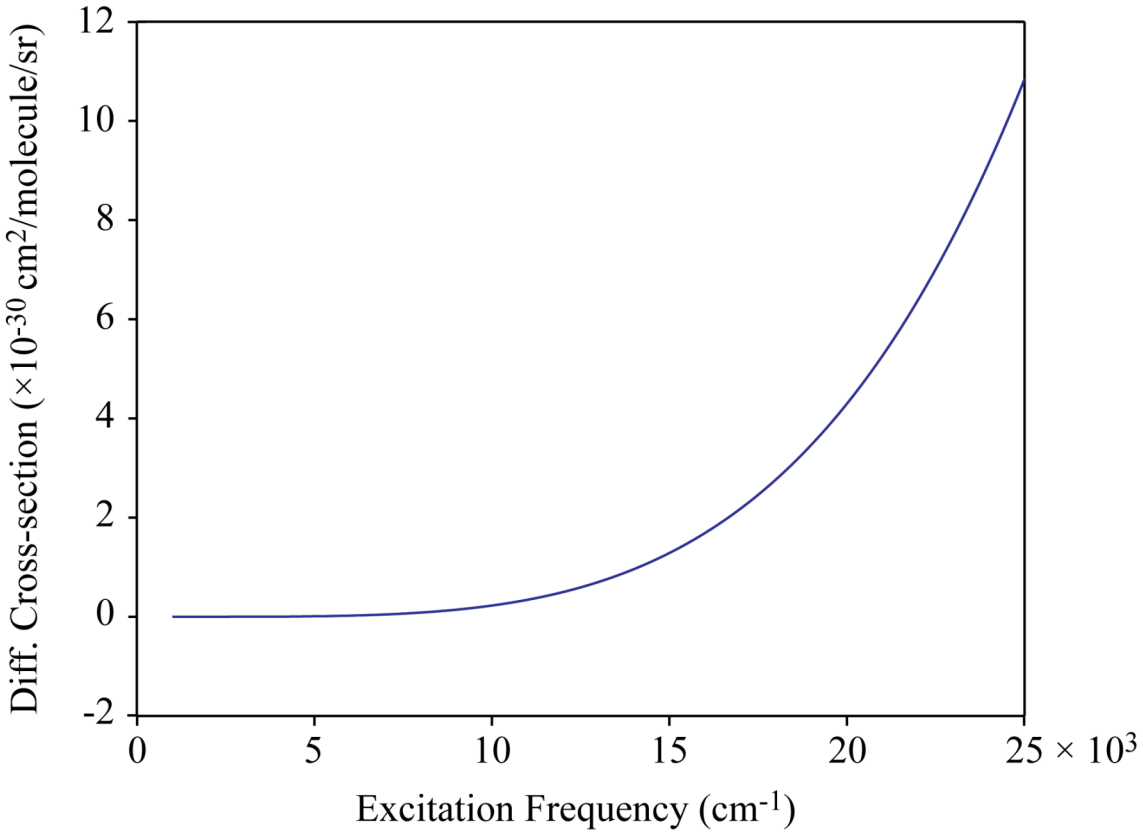

Figure 2.2 Dependence of the differential cross-section of the 1049 cm^{-1} NO_3^- stretch on excitation frequency as defined by the Albrecht A-term expression given in Equation 2.3.

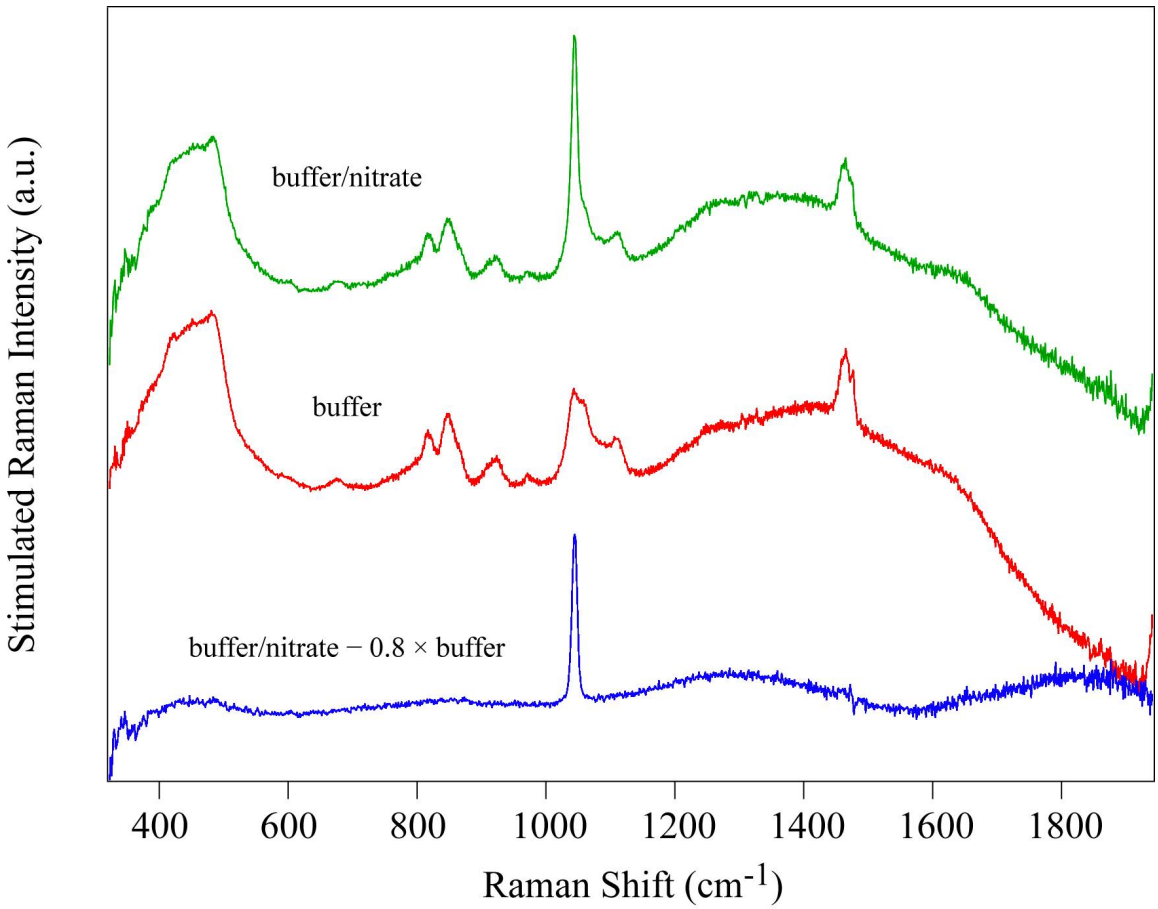

Figure 2.3 Stimulated Raman spectra of the TES–glycerol buffer and nitrate solutions used as standards in the calibration of the absolute Raman cross-sections of phytochrome Cph1. The green spectrum is that of TES–buffer containing 1.233 M glycerol and 250 mM nitrate, the red spectrum is that of TES–glycerol buffer alone and the blue spectrum is that of nitrate alone (250 mM).

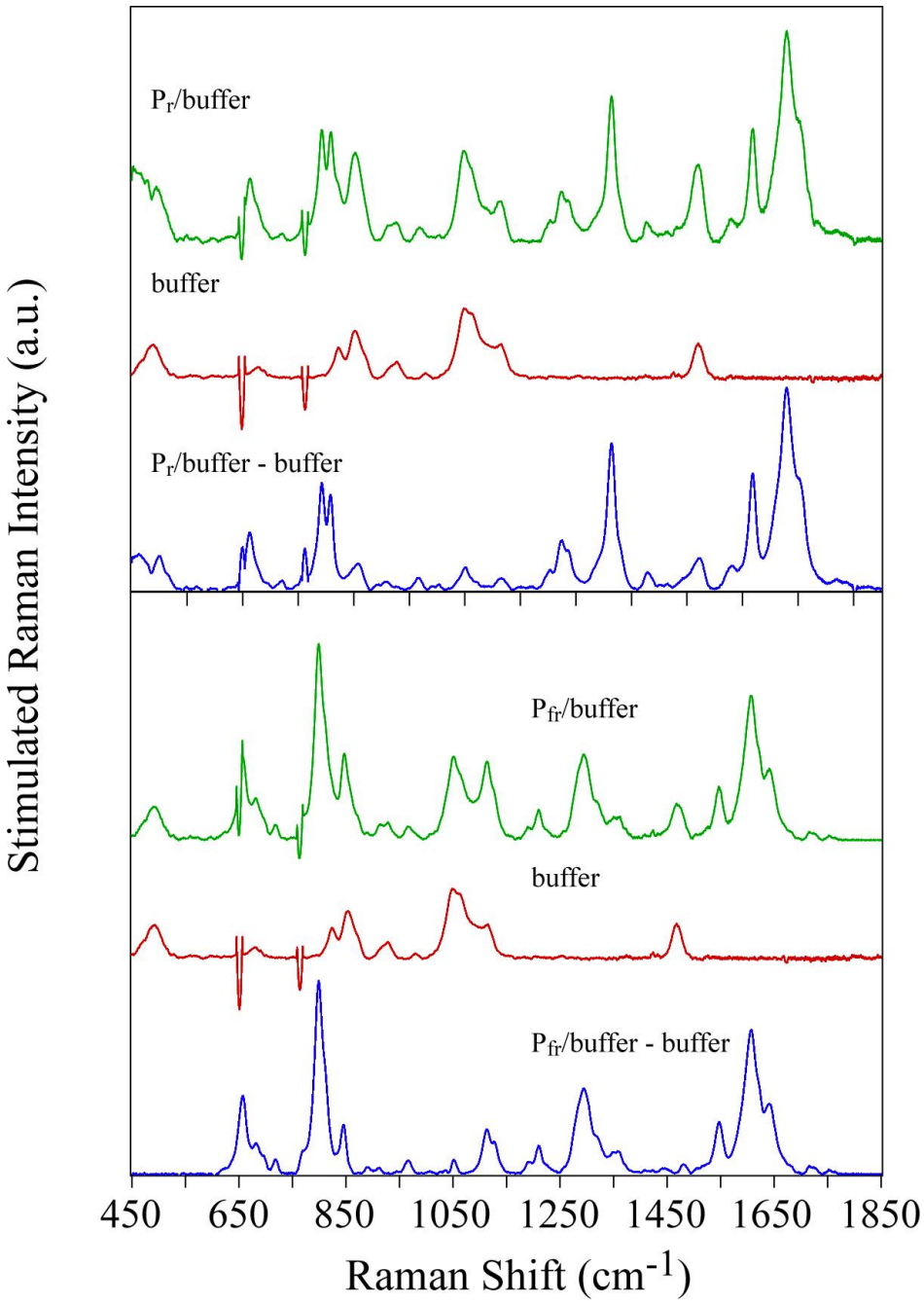

Figure 2.4 Stimulated Raman spectra used in the quantification of the absolute Raman cross-sections of phytochrome Cph1. Top panel: Raman spectra of 1.25×10^{-4} M P_r in TES–buffer containing 1.096 M glycerol (green), TES–glycerol buffer (red) and the P_r form of phytochrome Cph1 minus the buffer contribution (blue). Bottom panel: Raman spectra of 8.75×10^{-5} M P_{fr} in TES–buffer containing 1.096 M glycerol (green), TES–glycerol buffer (red) and the P_{fr} form of phytochrome Cph1 with the buffer contribution subtracted out (blue).

shows the Raman spectra used in this analysis, which include spectra of 1.25×10^{-4} M P_r and 8.75×10^{-5} M P_{fr} in buffer containing 1.096 M glycerol, and the pure phytochrome spectra after subtraction of the TES–glycerol buffer contribution. The phytochrome Raman bands were fit as shown in Figure 2.5 and then integrated to determine their relative areas. The differential cross-section of each Raman band was then found using Equation 2.4, where ν_R and ν_{std} are the scattered photon frequencies, A_R and A_{std} are the integrated Raman peak areas, and c_R and c_{std} are the concentrations of phytochrome and glycerol, respectively. The absolute Raman cross-sections were then determined using Equation 2.5:

$$\sigma_R = \frac{8\pi}{3}\left(\frac{1+2\rho}{1+\rho}\right)\left(\frac{\partial\sigma_R}{\partial\Omega}\right) \tag{2.5}$$

where the depolarization ratio, ρ, for all Cph1 bands was measured and found to be ~1/3.

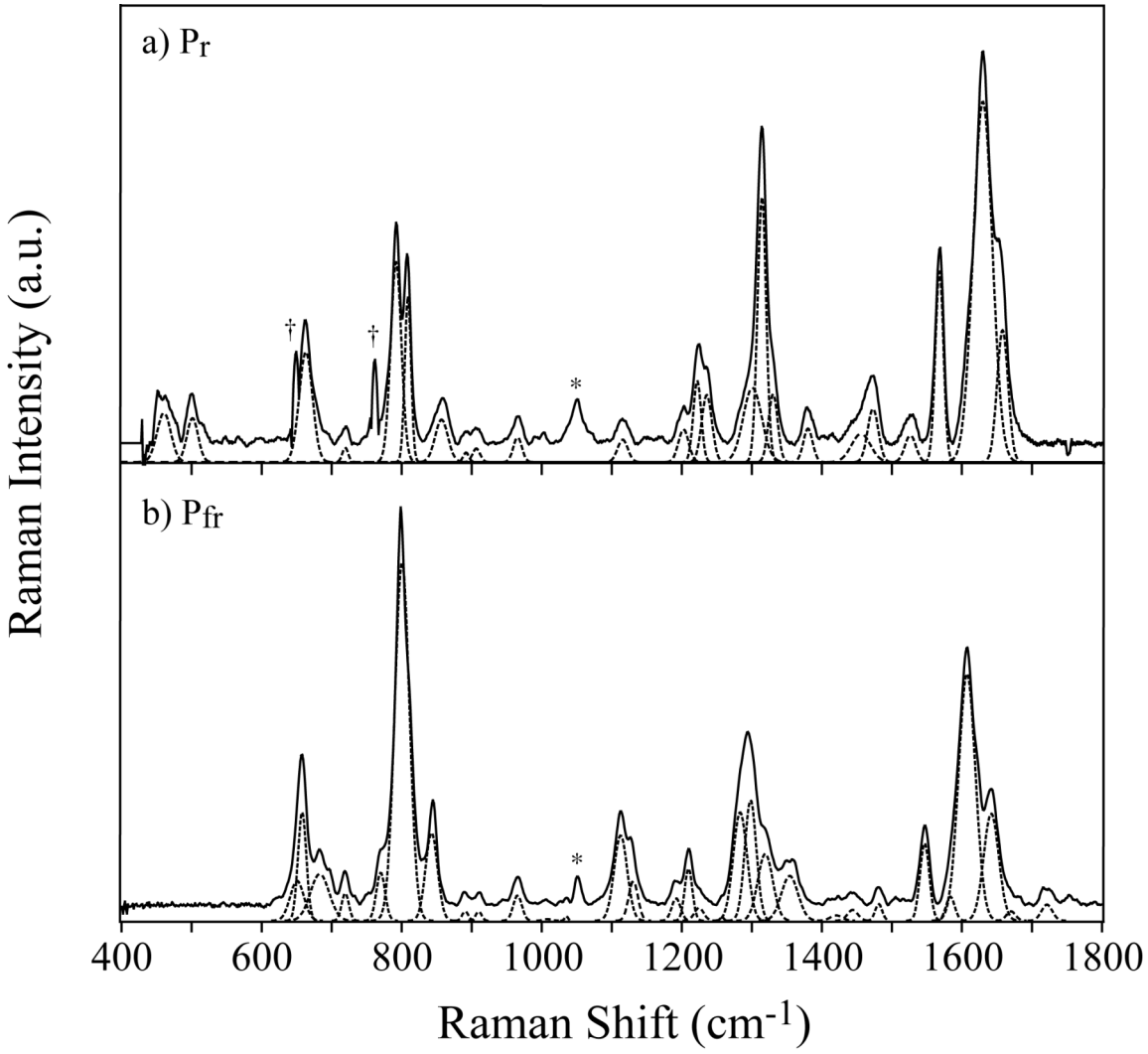

Figure 2.5 Stimulated Raman spectra (solid lines) of **a)** 1.25×10^{-4} M Cph1 P_r and **b)** 8.75×10^{-5} M Cph1 P_{fr} phytochrome obtained with a 3 μJ Raman pump pulse centered at 790.4 nm. Integrated areas of peak fits (dashed lines) were used to determine the absolute Raman cross-sections using the 1049 cm^{-1} NO_3^- symmetric stretch as an external standard. The residual peak at 1049 cm^{-1} indicated by an asterisk is due to the glycerol internal standard, and the features at 650 and 760 cm^{-1} indicated by a † are detector artifacts.

2.3 Rhodopsin sample preparation

A. Introduction

Rhodopsin is a visual pigment found in the vertebrate retina that is responsible for the first events in light perception. It consists of the protein moiety opsin and an 11-*cis* retinal chromophore that is covalently bound to an ε-amino group of the Lysine 296 residue. Upon absorption of light, the 11-*cis* retinal is isomerized to all-*trans*, which is eventually released from the protein [6]. Due to its high photoisomerization quantum yield of 0.65 [7], rhodopsin is extremely sensitive to light and must always be handled in the dark or under dim red light ($\lambda > 630$ nm).

Rhodopsin is an intrinsic membrane glycoprotein that constitutes 80-90% of the total protein content in the membranous disks of the rod cell outer segment [8-11]. Due to their high protein concentration, the photoreceptor membranes are an almost ideal preparation for studies on rhodopsin. Isolation of the photoreceptor membranes is most easily achieved by isolating the rod outer segments (ROS), as these are composed mostly of the membranous disks (>70% dry weight). The isolation and purification procedure is described here. This technique is specific to bovine rhodopsin, from which the results presented in this thesis were obtained, and is derived from that described by W. J. DeGrip [12]. Step-by-step instructions are provided in Appendix D.

B. Isolation of Rod Outer Segments (ROS)

ROS are connected to the rest of the photoreceptor cell by a thin cilium [13], as shown in Figure 2.6. The first step in the ROS isolation procedure is thus the separation of the ROS from the rest of the rod cell body, which is accomplished by homogenization (using a vortex mixer) of the retinas in an ice-cold medium containing 35% sucrose (w/w), 1.5 mM $CaCl_2$, 0.34 mM EDTA, 5 mM DTT and 20 mM MOPS buffer (pH 7.4). DTT is included in the medium to prevent oxidation of sensitive groups (i.e., polyunsaturated lipids and sulfhydryl groups), EDTA to chelate metal ions that may be present and $CaCl_2$ to act as a stabilizing agent. The homogenized solution is then centrifuged (4,340g; 4°C; 30 minutes; SW34 rotor) to remove tissue material (i.e., blood cells and nuclei) that is more dense than the ROS, which float in 35% sucrose [14].

The supernatant (containing ROS) is collected and then purified by density centrifugation, using sucrose as the density medium as it is inexpensive and innocuous to biological material. Continuous sucrose gradients are prepared from ice-cold sucrose (22% and 35% w/w; 6 × 16.5 mL in MOPS buffer) in a two-leg gradient mixer at 4°C. The ROS mixture is loaded carefully onto the top of the gradient using a plastic pipette; <20 mL of material is added to avoid overloading the gradients, which shifts purified ROS to a more dense position, making it more difficult to separate. Following centrifugation (112,400g; 4°C; 2.5 hours; SW28 rotor), the cell components are separated by density, as shown in Figure 2.7. The low-density components, consisting primarily of small membrane fragments and vesicles, are situated at the top of the gradient. The second, heavy band is almost pure ROS. The band below the ROS is a cytoplasm layer,

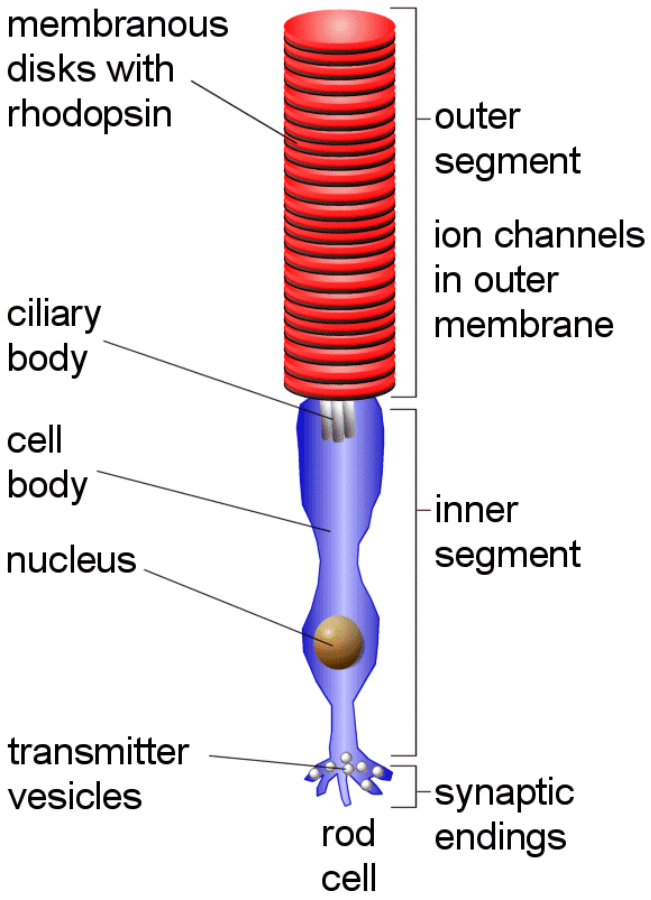

Figure 2.6 Rod cell structure. Rhodopsin is confined to the membranous disks in the outer segment.

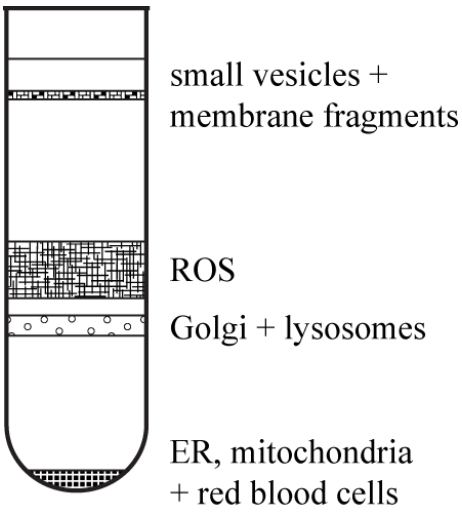

Figure 2.7 Band distribution following centrifugation of retinal filtrate on a continuous sucrose (22 to 35%) gradient.

containing Golgi and lysosomes. Finally, the pelleted sediment contains all larger organelles, such as the mitochondria, endoplasmic reticulum and red blood cells.

The upper, clear part of the gradient is collected with a glass pipette and discarded. The ROS bands are then collected and diluted 1:1 with MOPS buffer and centrifuged (39,000g; 4°C; 20 minutes; SS34 rotor). The pelleted ROS are lysed by suspending in ice-cold water and centrifuging (39,000g; 4°C; 45 minutes; SS34 rotor) to remove any water-soluble material.

C. Purification of Rhodopsin

Purification of rhodopsin necessitates solubilization with a mild detergent such as Ammonyx-LO. The process of solubilizing a membrane protein such as rhodopsin involves transferring it from its native environment, i.e., a cell membrane, to an artificial environment, such as a protein-detergent complex (micelle) [15]. This is accomplished by replacing lipid molecules present in the sample with detergent molecules. The soluble protein solution is homogeneous and consists of a mono-disperse distribution of rhodopsin molecules that do not sediment spontaneously. Membrane protein solubilization is a prerequisite for purification employing chromatographic methods.

The homogeneous rhodopsin solution is purified with hydroxyapatite (HA) chromatography. HA is a crystalline form of calcium phosphate with the molecular formula $Ca_{10}(PO_4)_6(OH)_2$ and is a multimodal chromatography support. In contrast to ion exchangers, which primarily exploit biomolecule interactions with a single type of chemical surface, HA binds both by nonspecific attraction with protein positive charges and specific complexing of protein carboxyl groups with HA calcium.[16] The calcium interactions can be eluted only by ions with a high calcium affinity, such as phosphate. In the case of rhodopsin, HA is equilibrated with phosphate buffer, with the phosphate ions complexing with the HA calcium and effectively neutralizing it, thus allowing the protein to elute from the column. The yield of rhodopsin from the column based on the amount loaded is typically 95-100%. The eluate is then concentrated as desired using Amicon centrifugal filter units (10 kDa MWCO). The sample purity is determined using UV/Visible spectroscopy and is indicated by the ratios of the extinction coefficient at 400 and 500 nm (A_{400}:A_{500}) and at 280 and 500 nm (A_{280}:A_{500}). Lower values for these ratios indicate higher sample purity. Typical ratios of A_{400}:A_{500} and A_{280}:A_{500} pre-column are 0.3 and 3, and for purified rhodopsin are 0.18 and 1.8, respectively. Typical absorption spectra of solubilized rhodopsin both pre- and post-column are shown in Figure 2.8.

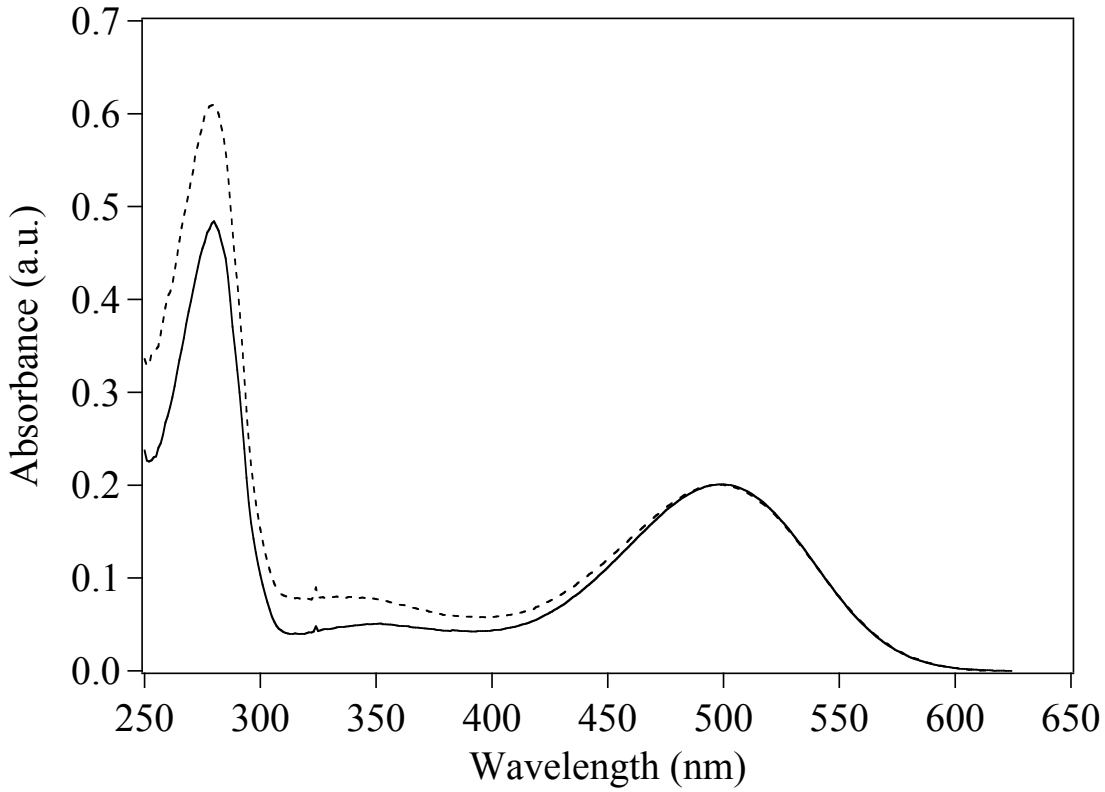

Figure 2.8 Absorption spectra of rhodopsin taken prior to (dashed) and after (solid) purification by hydroxyapatite chromatography. The spectra were normalized to 0.21 OD/cm at 500 nm.

2.4 References

[1] L. D. Ziegler, *Acc. Chem. Res.* **27,** 1 (1994).

[2] M. K. Lawless and R. A. Mathies, *J. Chem. Phys.* **96,** 8037 (1992).

[3] S. Y. Lee and E. J. Heller, *J. Chem. Phys.* **71,** 4777 (1979).

[4] A. B. Myers and R. A. Mathies, in *Biological Applications of Raman Spectroscopy*, T. G. Spiro, Ed. (John Wiley & Sons, New York, 1987), Vol. 2, p. 1.

[5] J. M. Dudik, C. R. Johnson and S. A. Asher, *J. Chem. Phys.* **82,** 1732 (1985).

[6] G. Wald, *Science* **162,** 230 (1968).

[7] J. E. Kim, M. J. Tauber and R. A. Mathies, *Biochemistry* **40,** 13774 (2001).

[8] F. J. M. Daemen, *Biochim. Biophys. Acta* **300,** 255 (1973).

[9] F. J. M. Daemen, W. J. DeGrip and P. A. A. Jansen, *Biochim. Biophys. Acta* **271,** 419 (1972).

[10] D. S. Papermaster and W. J. Dreyer, *Biochemistry* **13,** 2438 (1974).

[11] M. Makino, T. Hamanaka, Y. Orii and Y. Koto, *Biochim. Biophys. Acta* **495,** 299 (1977).

[12] W. J. DeGrip, F. J. M. Daemen and S. L. Bonting, *Methods Enzymol.* **67,** 301 (1980).

[13] D. G. McConnell, *J. Cell Biol.* **27,** 459 (1965).

[14] F. D. Collins, R. M. Love and R. A. Morton, *Biochem. J.* **47,** 3 (1950).

[15] A. Helenius and K. Simons, *Biochim. Biophys. Acta* **415,** 29 (1975).

[16] M. J. Gorbunoff, *Methods Enzymol.* **182,** 329 (1990).

Chapter 3

Homogeneity of Phytochrome Cph1 Vibronic Absorption Revealed by Resonance Raman Intensity Analysis

Reprinted with permission from the manuscript by Katelyn M. Spillane, Jyotishman Dasgupta, J. Clark Lagarias and Richard A. Mathies, *Journal of the American Chemical Society* **131,** 13946-13948 (2009).

3.1 Abstract

Phytochromes are an important class of red/far-red responsive photoreceptors that act as light-activated biological switches, ultimately driving growth and development in plants, bacteria, and fungi. The composition of the red-absorbing ground-state has been widely debated due to the presence of a shoulder feature on the blue edge of electronic absorption spectra, which many have attributed to the presence of multiple ground-state conformers. Here we use resonance Raman intensity analysis to calculate the vibronic absorption profile of cyanobacterial phytochrome Cph1 and show that this shoulder feature is due simply to vibronic transitions from a single species, thus reflecting a homogeneous ground-state population.

3.2 Introduction

Phytochromes are a family of photoreceptors found in plants, bacteria, and fungi that act as light-activated biological switches. They utilize covalently bound bilin chromophores that interconvert between two spectrally distinct conformers, a red (P_r) and far-red (P_{fr}) light-absorbing form [1], to drive signal transduction that ultimately controls growth and development [2]. The phototransformation is both rapid and reversible, and is driven by a *Z*-to-*E* isomerization about the C_{15}=C_{16} methine bridge between the C and D

rings of the linear tetrapyrrole chromophore (see Figure 3.1) [1,3]. However, the molecular structural evolution along the P_r-to-P_{fr} reaction coordinate is not yet fully understood.

Ultrafast transient absorption measurements on the cyanobacterial phytochrome Cph1, the plant phytochrome phyA, and the bacteriophytochrome Agp1 have been used to characterize the electronic changes in the P_r-to-P_{fr} transition [4-7]. These studies revealed two excited-state lifetimes characterized by a short (5-16 ps) and a long (25-40 ps) time constant, indicating at least two P_r excited states, but it is unknown whether these multiple states originate from a heterogeneous ground-state population or multiple reaction intermediates formed from a single initial conformer. The shape of the absorption band (λ_{max} = 660 nm), which features a distinct shoulder on the blue edge at ~620 nm (see Figure 3.1), has also attracted attention and has been interpreted by many as evidence for conformational heterogeneity of the ground state bilin chromophore population [8-10]. Resolution of the ground-state bilin conformer population is of fundamental importance in elucidating the excited-state reaction pathway and ultimately the cause of the low 15% photoisomerization quantum yield [11].

Here we investigate the P_r ground state of the cyanobacterial phytochrome Cph1 chromophore using resonance Raman intensity analysis to calculate the vibronic absorption profile. Measured resonance Raman intensities can be used to quantify the individual vibronic displacements that make up the Franck-Condon vibronic absorption spectrum. In this paper, we show that the absorption band profile including the prominent blue shoulder is due simply to vibronic transitions resulting from the absorption of a single P_r conformer of Cph1.

3.3 Methods

Recombinant Cph1 phytochrome (N514) was expressed and purified as described previously [12]. Prior to spectroscopic studies, samples were dialyzed against 1 L buffer (25 mM TES–KOH, pH 8.0, 25 mM KCl, 10% glycerol) and then concentrated to 10.6 OD_{660}/cm. For absolute Raman cross-section calibration, a standard solution of $NaNO_3$ (250 mM) was used. The protein sample for measurement contained 1.25×10^{-4} M Cph1 in glycerol-containing TES buffer. The stimulated Raman spectrum was obtained using the experimental setup described by McCamant et al [14]. (see Supporting Information (SI)).

The absolute Raman cross-sections of Cph1 were determined as described previously [15]. Briefly, the differential cross sections of the Cph1 bands were calculated using the 1052 cm^{-1} glycerol C–OH stretch mode as an internal standard. The absolute Raman cross-sections were determined from Equation 3.1:

$$\sigma_{Cph1} = \frac{8\pi}{3}\frac{(1+2\rho)}{(1+\rho)}\left(\frac{\partial\sigma}{\partial\Omega}\right)_{Cph1} \tag{3.1}$$

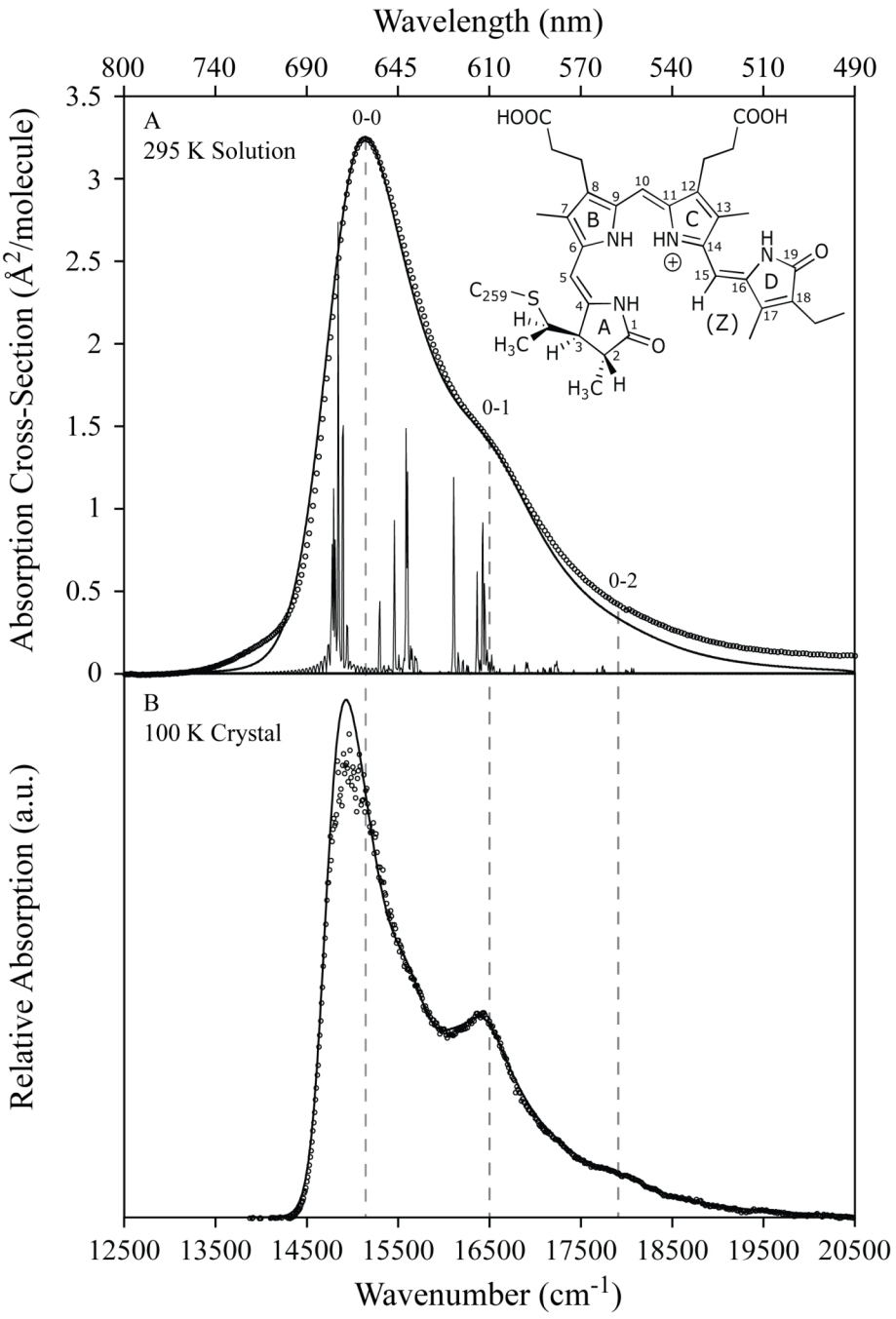

Figure 3.1. Comparison of the experimental and calculated absorption spectra for the P_r form of phytochrome Cph1 at 295 K in solution (A) and at 100 K in crystalline form (B) [13]. Experimental absorption spectra are shown as open circles. Calculated absorption spectra are shown as solid lines and were determined using the parameters listed in Table 1. The absorption FC factors for all modes with $\Delta > 0.2$ are presented (0–0 transition scaled ×0.0025) (see SI) (A). The ground state chromophore structure in the P_r form is *ZZZssa* as shown.

where the depolarization ratios, ρ, for all Cph1 bands were measured and found to be ~1/3.

Raman excitation profiles (REPs) were calculated using the time-dependent wavepacket formalism of resonance Raman scattering [16]. The absorption cross-sections, σ_A, were determined by the Fourier transform of $\langle i|i(t)\rangle$, where $|i\rangle$ is the initial vibrational eigenstate on the ground electronic surface and $|i(t)\rangle$ is the vibrational wavefunction of the initial state propagating on the excited electronic surface. The Raman cross-sections, σ_R, were determined by the square of the half-Fourier transform of $\langle f|i(t)\rangle$, where $|f\rangle$ is the final vibrational eigenstate on the ground electronic surface (see SI). The time-dependent overlaps, $\langle i|i(t)\rangle$ and $\langle f|i(t)\rangle$, depend on the dimensionless parameter Δ, which is the displacement between the ground and excited electronic state harmonic minima. Relative delta values were initially estimated from the intensities of the observed vibrational bands assuming $I \propto \omega^2\Delta^2$ [17]. The overall scaling of Δ, homogeneous broadening Γ_G, inhomogeneous broadening θ, zero-zero transition energy E_0, and electronic transition length M were then adjusted to provide the best fits.

3.4 Results and Discussion

The experimental and calculated absorption spectra of P_r in solution (295 K) are presented in Figure 3.1A. The absorption cross-section is 3.25 $Å^2$/molecule at the maximum, which was calculated based on the molar extinction coefficient e_{660} = 85000 M^{-1} cm^{-1} [18]. The spectrum is dominated by the 0–0 vibronic transition and features a shoulder on the blue edge near 16500 cm^{-1}, which is shown here to be the 0–1 vibronic transition. The absorption profile calculated using parameters derived from a 24-mode Raman intensity vibronic analysis (summarized in Table 3.1) agrees very well with the experimental spectrum. These parameters include an inhomogeneous broadening of 90 cm^{-1}, a homogeneous broadening of 880 cm^{-1} and a zero-zero transition energy of 14800 cm^{-1}. The minor baseline difference to the blue of 17250 cm^{-1} is attributed to a weak transition between the Q_y band and the Soret band at 360 nm that was not taken into account in the calculations [19,20] (see SI Figure A1).

The slight difference to the red of 14375 cm^{-1} is attributed to a population of vibrational modes with energies below k_BT (~200 cm^{-1} at RT) that was not observed experimentally, and accounts for less than 5% of the total integrated area. A highly displaced, 50 cm^{-1} mode was included in the calculations to model motion along these missing torsional coordinates.

The experimental and calculated absorption spectra of the crystalline (100 K) form of P_r are also in excellent agreement (Figure 3.1B). They exhibit the same vibronic features as the solution spectra, evidencing a single chromophore structure. The vibronic transitions are red-shifted by ~100 cm^{-1} relative to those in solution, most likely due to increased density, polarization, and dispersion interactions. In addition, the decreased temperature changes the distribution of transition energies of the individual molecules, thus reducing the overall line broadening and increasing the prominence of the 0–1 vibronic feature [21-23]. The parameters that gave the best fit to the 100 K absorption

Table 1. Resonance Raman Cross-Sections of Cph1 (P_r)

frequency [cm^{-1}]	expt cross section [$Å^2 \times 10^{-11}$][a]	calcd cross-section [$Å^2 \times 10^{-11}$]	delta [unitless][b]
50	–	–	0.80
502	3.11 ± 0.71	2.82	0.22
664	7.77 ± 1.39	7.44	0.29
722	1.05 ± 0.71	0.81	0.09
793	13.9 ± 2.38	13.9	0.35 (0.34)
808	11.9 ± 2.12	11.9	0.32 (0.31)
859	2.84 ± 0.63	2.83	0.15
892	0.73 ± 0.91	0.65	0.07
906	0.97 ± 0.79	0.86	0.08
967	1.69 ± 0.59	1.46	0.10
1116	1.54 ± 0.54	1.40	0.09
1204	2.34 ± 0.82	2.27	0.11
1225	6.26 ± 2.63	6.19	0.18
1235	4.84 ± 1.81	4.93	0.16
1301	6.40 ± 2.52	4.57	0.15
1314	20.0 ± 5.07	19.7	0.31 (0.37)
1331	5.44 ± 1.69	4.08	0.14
1379	2.27 ± 0.61	2.15	0.10
1456	2.17 ± 1.71	1.84	0.09
1474	4.26 ± 3.15	4.49	0.14
1530	1.81 ± 0.53	1.92	0.09
1569	12.4 ± 2.09	12.3	0.23 (0.25)
1630	24.8 ± 4.10	24.8	0.32 (0.35)
1652	12.9 ± 2.29	12.8	0.23 (0.25)

Table 3.1. a) Resonance Raman cross sections for the P_r form of phytochrome Cph1 determined relative to the 1052 cm^{-1} C–OH stretch of glycerol. The glycerol differential cross section at λ_{ex} = 790.4 nm was 5.28 × 10^{-16} $Å^2$ $molecule^{-1}$. b) Delta values for the room temperature structure were determined from Raman intensity calculations with Γ = 880 cm^{-1}, θ = 90 cm^{-1}, E_0 = 14800 cm^{-1} and M = 2.32 Å. Delta values for the crystal structure were determined using Γ = 430 cm^{-1}, θ = 50 cm^{-1}, E_0 = 14690 cm^{-1} and M = 2.32 Å and are shown in parentheses when different from the room temperature values.

spectrum were an inhomogeneous broadening of 50 cm^{-1}, a homogeneous broadening of 430 cm^{-1} and a zero-zero transition energy of 14690 cm^{-1}. The molar extinction coefficient of the crystal structure was not determined, and so the spectrum was scaled such that the electronic transition length matched that of the solution structure (M ~ 2.32 Å).

The Raman spectrum and calculated Raman cross-sections of P_r in solution are presented in Figure 3.2. Experimental cross-sections range from (0.73 ± 0.91) to (24.8 ± 4.10) × 10^{-11} $Å^2$ $molecule^{-1}$ at 892 cm^{-1} and 1630 cm^{-1}, respectively, and were determined by comparison of the P_r integrated peak areas to the integrated area of the glycerol C–OH stretch band at 1052 cm^{-1}. Calculated cross-sections were obtained by adjusting the overall scaling of the delta values to match the experimental peak intensities. The most notable bands are the C_{15}–H hydrogen out-of-plane (HOOP) mode at 793 cm^{-1} (Δ = 0.35), the mixture of the C_5–H and C_{15}–H HOOP modes at 808 cm^{-1} (Δ = 0.32), the N–H in-plane rock at 1314 cm^{-1} (Δ = 0.31), and the C=C stretch at 1630 cm^{-1} (Δ = 0.32) with cross-sections on the order of 10^{-10} $Å^2$/molecule (see Table 3.1). The equality of delta values indicates that the excitation energy is dissipated among multiple displaced modes as opposed to being focused along a small number of normal coordinates. Therefore, the wavepacket dynamics evidence multimodal evolution along the reaction trajectory.

Raman excitation profiles (REPs) for the representative 664, 793, 1314 and 1630 cm^{-1} modes are shown in Figure 3.3. Excitation profiles show the dependence of the Raman cross-section on excitation wavelength and were calculated based on the parameters used to fit the experimental absorption and Raman spectra of P_r in solution. The REPs of the 664 and 793 cm^{-1} bands show a single dominant band near the absorption maximum and a slight contribution at the 0–2 transition. As the vibrational frequency increases, the intensity in the 0–0 transition region decreases slightly and increases significantly in the 0–1 and 0–2 transition regions, as shown for the 1314 cm^{-1} and 1630 cm^{-1} REPs. The REPs show that the relative Raman intensities will change as a function of excitation wavelength, and that pumping at an excitation wavelength closer to resonance would increase these intensities by three orders of magnitude. In our case, due to the significant fluorescence background from the P_r form, we pumped at a single frequency 2500 cm^{-1} to the red of the absorption maximum.

One important observation is the ratio of the absorption cross-sections of the 0–0 and 0–1 vibronic transitions. In solution at 295 K this ratio is A_{0-0}/A_{0-1} = 2.4 (Figure 3.1A). If multiple species existed in the system, a change in temperature should shift the equilibrium, thus modifying the relative population of conformers and the resulting absorption spectrum. We see, however, that at 100 K the ratio of the vibronic transition strengths remains 2.4 (Figure 3.1B), further supporting a homogeneous system.

This observation is contrary to previous suggestions of a structurally heterogeneous population of phytochromes. The fluorescence data of 80 individual Agp1 phytochrome molecules at 100 K presented by Nieder and coworkers showed a series of single-molecule fluorescence emission spectra, each attributed to a different conformer [8]. At low temperatures, however, excited molecules can photoconvert to different

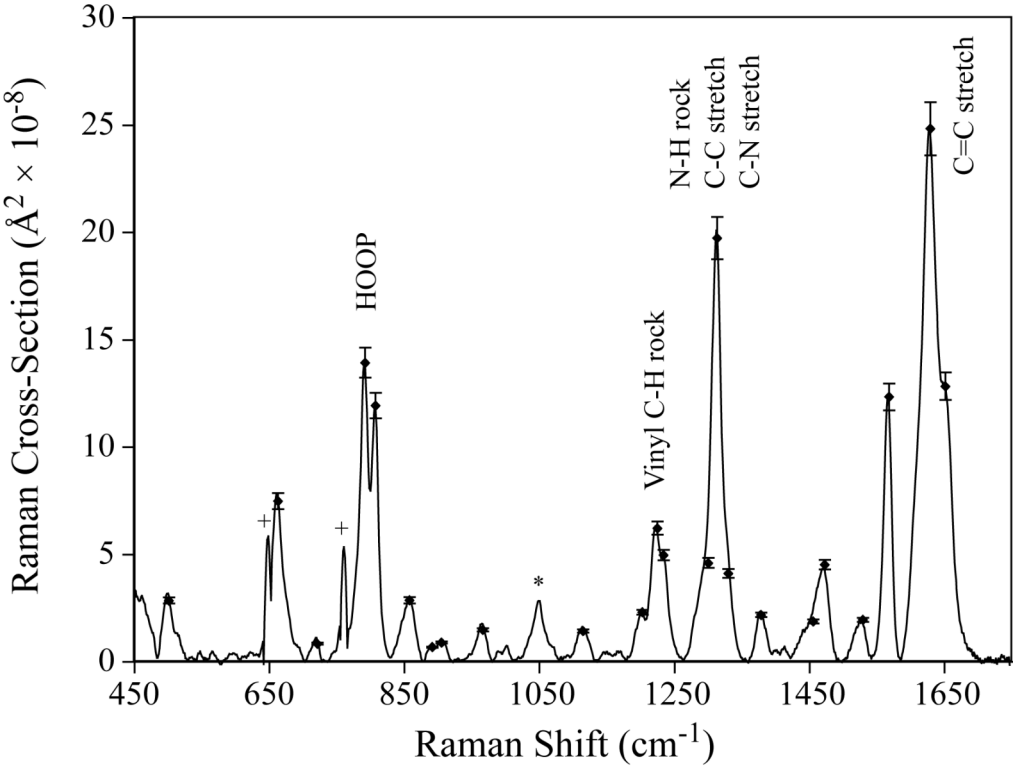

Figure 3.2. Stimulated Raman spectrum (solid line) of 1.25 × 10^{-4} M Cph1 P_r phytochrome obtained using a 3 μJ Raman pump pulse centered at 790.4 nm. Integrated peak areas were used to determine the absolute Raman cross-sections presented in Table 3.1 using the symmetric stretch of NO_3^- at 1045 cm^{-1} as an external standard. The peak at 1052 cm^{-1} indicated by an * is due to the glycerol internal standard, and the features at 650 and 760 cm^{-1} indicated by a + are detector artifacts.

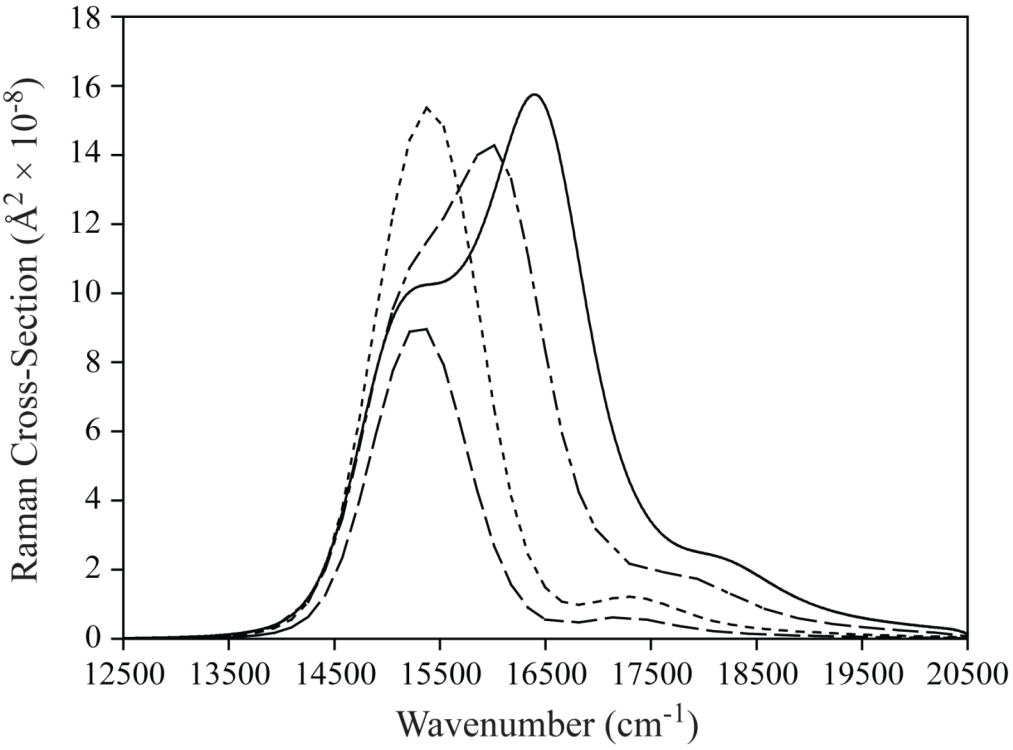

Figure 3.3. Comparison of representative calculated Raman excitation profiles for the 664 (— — — —), 793 (- - - - - -), 1314 (— - — - —), and 1630 cm-1 (———) modes using the parameters listed in Table 3.1.

locally trapped intermediate states with unique absorption profiles, fluorescence spectra, and decay rates that may account for this heterogeneity [3,7].

Temperature dependent measurements of the P_r absorption profile of native PhyA revealed an isosbestic point, which was argued to support the presence of two species in equilibrium [9]. However, recent theoretical and experimental studies have shown that isosbestic points can exist in the inhomogeneously broadened spectra of a homogeneous system due to the slightly different local environments that individual solutes experience [23]. Furthermore, we have successfully modeled the P_r vibronic absorption profiles of phytochrome Cph1 as a function of temperature, including the isosbestic point, by simply changing the temperature from 8 to 40°C in the theory and adjusting the homogeneous contribution to the broadening (see SI Figure A3). Thus, the absorption isosbestic point does not provide definitive evidence for multiple P_r conformers and we can conclude that Cph1's P_r absorption spectrum reflects a single predominant species in solution.

3.5 Acknowledgments

We thank Jon Hughes (University of Giessen) for the 100 K crystal absorption spectrum and Anne Myers Kelley (UC Merced) for the RRModel program. We also thank Lester Hedges for computational assistance. This work was supported by the Mathies Royalty Fund and supported in part by a grant from the National Institutes of Health (GM068552) to J.C.L.

3.6 References

[1] N. C. Rockwell, Y. S. Su and J. C. Lagarias, *Annu. Rev. Plant Biol.* **57,** 837 (2006).

[2] P. H. Quail, *Nat. Rev. Mol. Cell Biol.* **3,** 85 (2002).

[3] J. Dasgupta, R R. Frontiera, K. C. Taylor, J. C. Lagarias and R. A. Mathies, *Proc. Natl. Acad. Sci. U.S.A.* **106,** 1784 (2009).

[4] C. Schumann, R. Groß, N. Michael, T. Lamparter and R. Diller, *ChemPhysChem* **8,** 1657 (2007).

[5] K. Heyne, J. Herbst, D. Stehlik, B. Esteban, T. Lamparter, J. Hughes and R. Diller, *Biophys. J.* **82,** 1004 (2002).

[6] M. G. Müller, I. Lindner, I. Martin, W. Gärtner and A. R. Holzwarth, *Biophys. J.* **94,** 4370 (2008).

[7] A. R. Holzwarth, E. Venuti, S. E. Braslavsky and K. Schaffner, *Biochim. Biophys. Acta* **1140,** 59 (1992).

[8] J. B. Nieder, M. Brecht and R. Bittl, *J. Am. Chem. Soc.* **131,** 69 (2009).

[9] P. Schmidt, T. Gensch, A. Remberg, W. Gärtner, S. E. Braslavsky and K. Schaffner, *Photochem. Photobiol.* **68,** 754 (1998).

[10] D. von Stetten, M. Günther, P. Scheerer, D. H. Murgida, M. A. Mroginski, N. Krauß, T. Lamparter, J. Zhang, D. M. Anstrom, R. D. Vierstra, K. T. Forest and P. Hildebrandt, *Angew. Chem. Int. Ed.* **47,** 4753 (2008).

[11] T. Lamparter, F. Mittmann, W. Gärtner, T. Börner, E. Hartmann and J. Hughes, *Proc. Natl. Acad. Sci. U.S.A.* **94,** 11792 (1997).

[12] G. A. Gambetta and J. C. Lagarias, *Proc. Natl. Acad. Sci. U.S.A.* **98,** 10566 (2001).

[13] L. -O. Essen, J. Mailliet and J. Hughes, *Proc. Natl. Acad. Sci. U.S.A.* **105,** 14709 (2008).

[14] D. W. McCamant, P. Kukura, S. Yoon and R. A. Mathies, *Rev. Sci. Instrum.* **75,** 4971 (2004).

[15] A. B. Myers and R. A. Mathies, in *Biological Applications of Raman Spectroscopy*, T. G. Spiro, Ed. (John Wiley & Sons, New York, 1987), Vol. 2, p. 1.

[16] S. Y. Lee and E. J. Heller, *J. Chem. Phys.* **71,** 4777 (1979).

[17] J. Tang and A. C. Albrecht, in *Raman Spectroscopy: Theory and Practice*; H. A. Szymanski, Ed. (Plenum Press, New York, 1970), Vol. 2, p. 33.

[18] T. Lamparter, B. Esteban and J. Hughes, *Eur. J. Biochem.* **268,** 4720 (2001).

[19] R. A. Matute, R. Contreras, G. Pérez-Hernández and L. González, *J. Phys. Chem.* B **112,** 16253 (2008)

[20] B. Borucki, H. Otto, G. Rottwinkel, J. Hughes, M. P. Heyn and T. Lamparter, *Biochemistry* **42,** 13684 (2003).

[21] V. M. Boitsov and V. I. Yuzhakov, *J. Appl. Spectrosc.* **45,** 1200 (1986).

[22] S. Mukamel *Principles of Nonlinear Optical Spectroscopy;* (Oxford University Press, New York, 1995)

[23] P. L. Geissler, *J. Am. Chem. Soc.* **127,** 14930 (2005).

Chapter 4

Conformational homogeneity and excited-state isomerization dynamics of the bilin chromophore in phytochrome Cph1 from resonance Raman intensities

4.1 Abstract

The ground-state structure and excited-state isomerization dynamics of the P_r and P_{fr} forms of phytochrome Cph1 are investigated using resonance Raman intensity analysis. Electronic absorption and stimulated resonance Raman spectra of P_r and P_{fr} are presented; vibronic analysis of the Raman intensities and absorption spectra reveals that both conformers exist as a single, homogeneous population of molecules in the ground state. The homogeneous and inhomogeneous contributions to the overall electronic broadening are determined, and it is found that the broadening is largely homogeneous in nature, pointing to fast excited-state decay. FC displacements reveal the initial atomic motions in the excited state, including the highly displaced, non-totally symmetric torsional and C_{15}–H HOOP modes that result from a loss of symmetry due to ground-state distortions about the C_{14}–C_{15} and C_{15}=C_{16} bonds. P_{fr} is especially well primed for ultrafast isomerization and torsional FC analysis predicts a <200 fs $P_{fr} \rightarrow P_r$ isomerization. This time is significantly faster than the observed 700 fs reaction time, indicating that the P_{fr} S_1 surface has a D-ring rotational barrier caused by steric interactions with the protein.

4.2 Introduction

Biological photoreceptors are responsible for the conversion of sunlight into chemical energy and information, and as such are critical for the survival and growth of the vast majority of life forms. In plants and bacteria, phytochromes regulate functional processes by interconverting between two thermally stable isomers: the physiologically inactive red-absorbing state (P_r) and the active far-red-absorbing state (P_{fr}) [1]. This transformation is achieved by a *Z*-to-*E* isomerization about the C_{15}=C_{16} methine bridge in

the open-chain tetrapyrrole (bilin) chromophore, which is covalently bound to the protein through a cysteine residue (Figure 4.1) [2]. This rapid and reversible reaction is followed by subsequent dark relaxation processes that eventually lead to changes in protein conformation that are coupled to the activation of target genes [3].

Ultrafast pump-probe electronic spectroscopy has been used to investigate the photochemistry of various phytochromes, revealing several intermediate states in the reaction pathway. For the $P_r \rightarrow P_{fr}$ photoconversion, two excited-state intermediates (I* and Lumi-R*) have been identified which lead to the formation of the first ground-state photoproduct Lumi-R [4-6]. Dasgupta et al. have shown that P_r undergoes rapid structural change on the excited state, forming the first fully isomerized excited-state intermediate Lumi-R* by 3 ps [4]. For the $P_{fr} \rightarrow P_r$ transformation, at least three kinetic components involved in the formation of the first photoproduct have been observed, but the intermediate and photoproduct states remain poorly characterized [7]. Previous studies have found that the *E*-to-*Z* isomerization takes place on the order of ~700 fs [7,8], although the first isomerized intermediate in the $P_{fr} \rightarrow P_r$ reaction has not yet been identified.

To further explore the early-time structural dynamics of P_r and P_{fr} following excitation, it is necessary to employ a high-resolution structural technique. Resonance Raman (RR) spectroscopy is ideal for the examination of primary photochemistry in pigment-containing proteins, as photoexcitation near the electronic absorption of the chromophore resonantly enhances Raman scattering from the chromophore modes with minimal interference from scattering by the surrounding non-resonant protein. While the vibrational frequencies in a RR spectrum provide detailed information about the ground-state molecular geometry, the RR line intensities report on the early-time (0-50 fs) molecular evolution on the excited-state surface [9]. The intensity of each vibrational line reflects the change in geometry between the electronic ground and excited states along that normal coordinate, and vibronic analysis reveals mode-specific information about the excited-state potential energy surface in the FC region.

RR spectroscopy also allows the examination of the ground-state structural composition of the bilin chromophore, which is currently a major point of discussion. The shoulder on the blue edge of the P_r and P_{fr} absorption spectra (Figure 4.2) has previously been interpreted as a unique electronic transition due to a second conformational species, thus suggesting conformational heterogeneity in both the P_r and P_{fr} ground states [10-13]. Other researchers subsequently supported a heterogeneous composition based on the measurement of multiple excited-state lifetimes by ultrafast pump-probe spectroscopy [7,14]. More recently, Song et al. used magic-angle spinning NMR spectroscopy to examine the P_r ground state, and concluded that it consists of two isoforms with different hydrogen bonding networks in the chromophore binding domain [15]. In contrast, using femtosecond stimulated Raman spectroscopy (FSRS), Dasgupta et al. monitored the structural dynamics of P_r following photoexcitation and saw no evidence of structural heterogeneity [4]. In addition, we have previously used RR intensity analysis to provide evidence that P_r is homogeneous in the ground state [16].

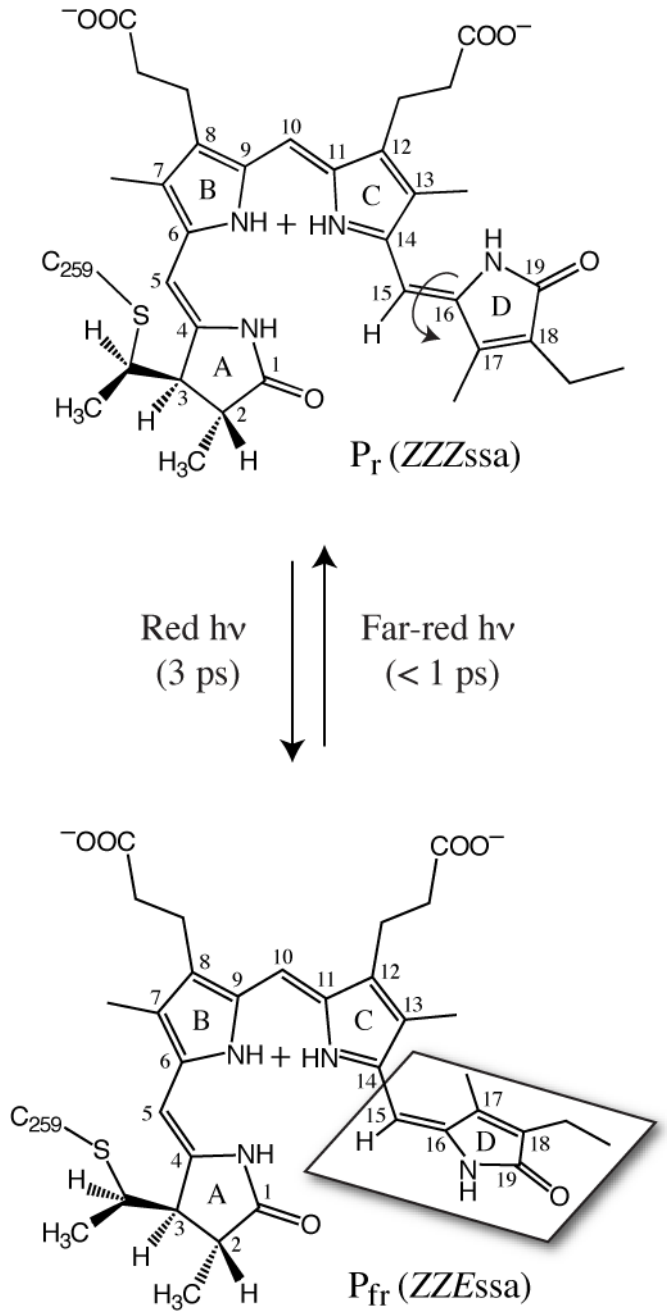

Figure 4.1. Structural changes of the bilin chromophore during the P_r-to-P_{fr} photocycle in phytochrome. The ground-state P_r chromophore structure is depicted as *ZZZ*ssa at the AB, BC and CD rings, respectively. Photoexcitation results in isomerization of the C_{15}=C_{16} methine bridge between the C and D rings, yielding the red-shifted *ZZE*ssa product P_{fr}. The D ring in P_{fr} is twisted out of the plane by ~20° due to the methyl-methyl steric interaction.

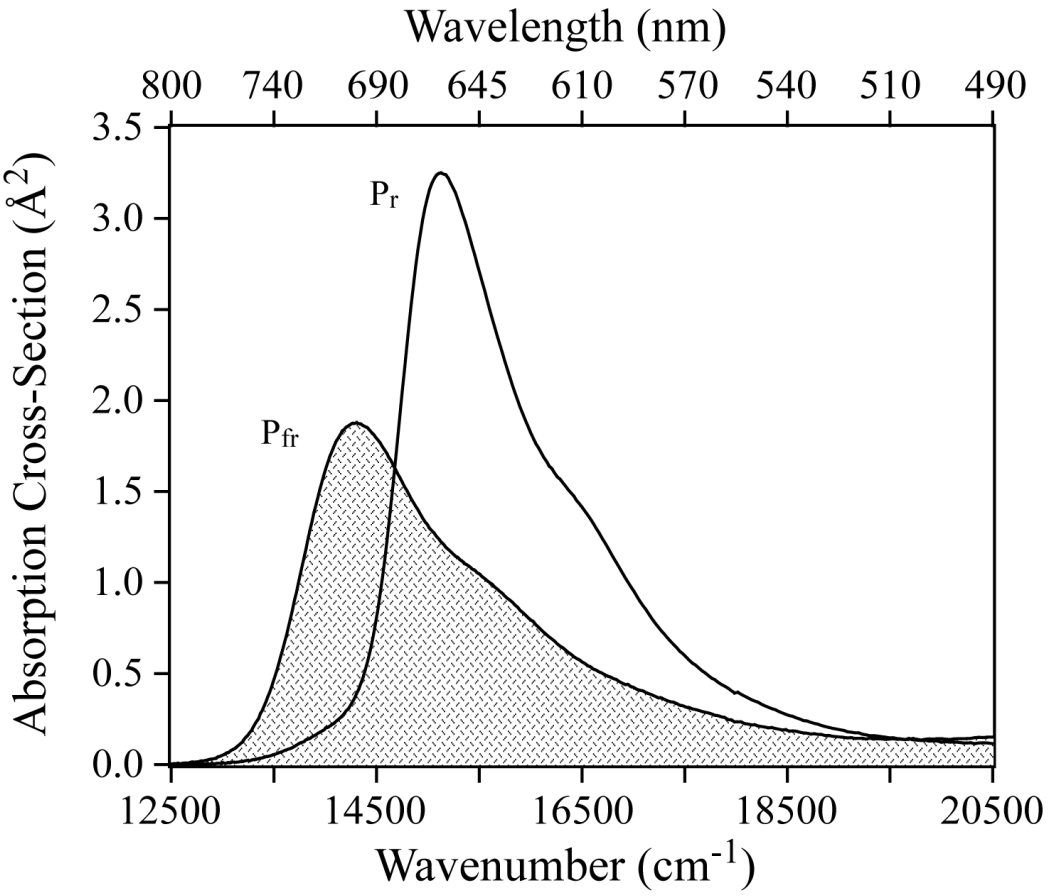

Figure 4.2. Absorption spectra of the P_r and P_{fr} forms of phytochrome Cph1 in TES-glycerol buffer at 295 K. The P_r form absorbs light maximally at 660 nm while the P_{fr} form absorbs maximally at 700 nm. The two forms are photoconvertible at room temperature.

Here we present a more complete RR intensity analysis study on P_r as well as an analysis of the ground-state structure and excited-state dynamics of P_{fr}. Vibronic analysis provides an in depth analysis of the P_r and P_{fr} ground-state composition, and the RR intensities reveal the initial atomic displacements on the excited-state surface for each of the observed normal modes. In addition to the expected displacements in the C=C rock and torsion, we see a strong HOOP displacement in P_{fr} that reveals the multidimensional nature of the initial photochemical dynamics.

4.3 Materials and Methods

Experimental Methods. Recombitant Cph1(N514) was expressed and purified as a phytocyanobilin-bound holoprotein as described previously [17]. The purified protein was then dialyzed overnight against 1 L buffer (25 mM TES–KOH, pH 8.0, 25 mM KCl, 10% glycerol). Prior to spectroscopic studies, samples were concentrated in Amicon spin prep columns (10-kDa cut-off) to 1.25×10^{-4} M. The RR spectra were obtained using the FSRS setup which has been described previously [18]. Briefly, a home-built mode-locked Ti:sapphire oscillator was amplified by a 1 kHz, 800 μJ regenerative amplifier (BMI Alpha 1000/US). This produced a train of 50-fs pulses centered at 795 nm which were used to generate the pump and probe pulses for the Raman measurements. A grating-based spectral filter generated the Raman pump pulse (790.4 nm, 4 ps, 3 μJ). A small portion of the amplifier output was used to produce the ~20-fs probe pulse by continuum generation in a 3-mm-thick sapphire plate, followed by pulse compression in a fused-silica prism compressor. The near-IR portion of the continuum was selected with an 830 nm long-pass filter and split into probe and reference beams by a 50:50 beam splitter, producing a 6 nJ probe pulse at the sample point. The noncollinear, horizontally polarized Raman pump and probe pulses were focused at the sample point, after which the probe was spatially selected, collimated and sent with the reference beam to the spectrograph (ISA HR320, 600 grooves/mm). The beams were then dispersed and imaged onto a Pixis:100F charge coupled device (CCD, Princeton Instruments). The CCD read-out rate was 1 kHz, allowing for single-shot detection. The frequency resolution was 10 cm^{-1} as determined by the 802 cm^{-1} cyclohexane band. The Raman spectra were determined as the ratio of the *Raman-pump-on* probe spectrum divided by the *Raman-pump-off* probe spectrum after normalization with the reference beam.

The samples were flowed through a homemade 1 × 2 × 40 mm Borofloat-glass flow channel and all measurements were taken at room temperature. The 500 μL sample was stored in a glass reservoir and driven through the flow cell by a peristaltic pump connected with PTFE tubing (0.5 mm inner diameter). The flow rate (~1 mL min^{-1}) was adjusted to replenish fresh sample for each laser pulse. For P_r Raman measurements, the photo-excited material was converted back to the P_r ground state by irradiation of the reservoir by a high-powered LED (720 nm, 5 mW, Roithner Lasertechnik) through an RG695 long-pass filter (Newport, Inc.). For P_{fr} measurements the reservoir was irradiated by a 650 nm, 2 mW LED. Sample integrity was confirmed by steady-state Raman and UV/Visible spectroscopy before and after the experiments and no irreversible spectral changes were observed.

For low-temperature (glass) absorption measurements, the sample was mixed with glycerol (65:35, v/v ratio) and sealed in an Oxford Instruments cryostat using a silanized 200 μm quartz cell (Starna). All molecules in the sealed sample were converted to the P_r form by saturating irradiation at room temperature with the 720 nm LED and an absorption measurement at room temperature revealed the OD at 660 nm to be 0.26 (per 200 μm). The sample was cooled to 100 K and an absorption measurement of P_r was taken. It was then brought to room temperature and photo-converted to a 70:30 mixture of P_{fr}/P_r by saturating irradiation with a 650 nm LED [19]. The sample was again cooled to 100 K and the absorption measurement was repeated. The pure P_{fr} absorption spectrum at each temperature was calculated as $A_{Pfr} = \left(A_{\mathrm{Pr/Pfr}} - 0.3 \times A_{\mathrm{Pr}}\right)/0.7$, where A_{Pr} and A_{Pfr} are the absorption intensities of the P_r and P_{fr} forms, respectively, and $A_{Pr/Pfr}$ is the absorption intensity of the mixed sample.

Computational Methods. Absolute Raman cross-sections of Cph1 were calculated as described previously [9] by comparing the integrated peak areas to that of the 1049 cm^{-1} NO_3^- symmetric stretch. Because nitrate can be damaging to the protein, the calibration was done indirectly by the following process. First, the differential cross-section of the 1049 cm^{-1} NO_3^- symmetric stretch was determined to be $(5.87 \pm 0.01) \times 10^{-31}$ cm^2 $molecule^{-1}$ $steradian^{-1}$ at 790.4 nm excitation by extrapolation from the known differential cross-section at 514.5 nm excitation ($(10.9 \pm 1.09) \times 10^{-30}$ cm^2 $molecule^{-1}$ $steradian^{-1}$) [20]. This was achieved using the Albrecht A term expression, which gives the following frequency dependence of the differential Raman cross-sections:

$$\frac{\partial \sigma_R}{\partial \Omega} = K \nu_0 \left(\nu_0 - \nu_{mn}\right)^3 \left[\frac{\nu_e^2 + \nu_0^2}{\left(\nu_e^2 - \nu_0^2\right)^2}\right]^2 \qquad (4.1)$$

where the constant K was 1.56×10^{-28} cm^2 $molecule^{-1}$ $steradian^{-1}$ and the frequency of the transition to the resonant electronic excited state (ν_e) was 52,300 cm^{-1} [20]. In this expression, ν_{mn} represents the frequency of the vibrational band of interest and ν_0 represents the excitation frequency.

The Raman spectrum of TES-buffer containing 250 mM NO_3^- and 1.233 M glycerol was then measured and the differential cross-section of the 1049 cm^{-1} glycerol C–OH stretch at 790.4 nm excitation was determined to be $(1.31 \pm 0.14) \times 10^{-30}$ cm^2 $molecule^{-1}$ $steradian^{-1}$ using the above-calculated nitrate differential cross-section and Equation 4.2:

$$\left(\frac{\partial \sigma_{glyc}}{\partial \Omega}\right) = \frac{\left(\nu_S\right)_{glyc}^3}{\left(\nu_S\right)_{nit}^3} \frac{A_{glyc}}{A_{nit}} \frac{c_{nit}}{c_{glyc}} \left(\frac{\partial \sigma_{nit}}{\partial \Omega}\right) \qquad (4.2)$$

where $(\nu_S)_{glyc}$ and $(\nu_S)_{nit}$ are the scattering frequencies, A_{glyc} and A_{nit} are the integrated peak areas, and c_{glyc} and c_{nit} are the concentrations of glycerol and NO_3^-, respectively. By the same method, the Raman spectrum of 1.25×10^{-4} M phytochrome Cph1 in TES–

buffer containing 1.096 M glycerol was measured at 790.4 nm and the glycerol C–OH stretch was used as an internal standard to determine the differential cross-sections of the Cph1 bands. The absolute Raman cross-sections of Cph1 were then determined using Equation 4.3:

$$\sigma_R = \frac{8\pi}{3}\left(\frac{1+2\rho}{1+\rho}\right)\left(\frac{\partial\sigma_R}{\partial\Omega}\right) \tag{4.3}$$

where the depolarization ratios, ρ, for all Cph1 bands were measured and found to be ~1/3.

Absorption and Raman cross-sections were calculated using the time-dependent wavepacket formalism of RR scattering [21]. The absorption cross-sections, σ_A, were determined by the Fourier transform of $\langle i|i(t)\rangle$, where $|i\rangle$ is the initial vibrational wavefunction on the ground electronic surface and $|i(t)\rangle$ is this initial wavefunction propagating on the excited electronic surface (Equation 4.4). The absolute Raman cross-sections, σ_R, were determined by the square of the half-Fourier transform of $\langle f|i(t)\rangle$, where $|f\rangle$ is the final vibrational wavefunction on the ground electronic surface (Equation 4.5):

$$\begin{aligned}\sigma_A(E_L) = {} & \frac{4\pi e^2 M^2 E_L}{6\hbar^2 cn\theta(2\pi)^{1/2}}\int_0^\infty dE \\ & \times\exp\left[\frac{-(E-E_0)^2}{2\theta^2}\right]\int_{-\infty}^{\infty} dt\langle i|i(t)\rangle e^{-\Gamma_G^2 t^2/\hbar^2} e^{i(E_L+\varepsilon_i)t/\hbar}\end{aligned} \tag{4.4}$$

$$\begin{aligned}\sigma_R(E_L,E_S) = {} & \frac{8\pi E_S^3 E_L e^4 M^4}{9\hbar^6 c^4\theta(2\pi)^{1/2}}\int_0^\infty dE \\ & \times\exp\left[\frac{-(E-E_0)^2}{2\theta^2}\right]\left|\int_0^\infty dt\langle f|i(t)\rangle e^{-\Gamma_G^2 t^2/\hbar^2} e^{i(E_L+\varepsilon_i)t/\hbar}\right|^2\end{aligned} \tag{4.5}$$

where E_L and E_S are the frequencies of the laser and scattered light, M is the electronic transition length, E_0 is the zero-zero transition energy, ε_i is the vibrational energy of eigenstate *i*, Γ_G is the Gaussian homogeneous broadening and θ is the standard deviation of the Gaussian distribution of zero-zero transition energies. The time-dependent overlaps, $\langle i|i(t)\rangle$ and $\langle f|i(t)\rangle$, depend on the dimensionless parameter Δ, which is the change in equilibrium geometry between the ground and excited states upon electronic excitation and is represented as the displacement between the ground and excited

electronic state harmonic minima. RR intensity calculations were performed using the program RRModel.f, written by Anne Myers Kelley of UC Merced, to model the experimental absorption spectra and Raman cross-sections. Relative delta values were initially estimated from the integrated intensities of the observed Raman bands assuming $I \propto \omega^2\Delta^2$ [22]. The overall scaling of Δ, homogeneous broadening Γ_G, inhomogeneous broadening θ, zero-zero energy E_0 and electronic transition length M were then adjusted to provide the best fits.

4.4 Results

The experimental and calculated absorption spectra of the P_r and P_{fr} forms of phytochrome Cph1 are shown in Figures 4.3 and 4.4, respectively. Spectra of 295 K solutions (Figures 4.3a and 4.4a) and 100 K glasses (Figures 4.3b and 4.4b) were acquired. The P_r absorption cross-section at 295 K was determined to be 3.25 Å^2/molecule at the 660 nm maximum based on the molecular extinction coefficient ε_{660} = 85,000 M^{-1} cm^{-1} [23]. Relative to this value, the peak cross-sections of the 100 K P_r form and the 295 and 100 K P_{fr} forms were determined to be 4.5, 1.88 and 2.70 Å^2/molecule, respectively. At 295 K, both isomers display a poorly resolved shoulder on the blue edge of the spectrum. Upon cooling to 100 K, the shoulder becomes more clearly resolved due to a decrease in spectral broadening. The small feature at 700 nm in the P_r spectra is due to residual P_{fr}. The minor baseline difference to the blue of 580 nm for P_r and 630 nm for P_{fr} is caused by a weak transition at 360 nm that was not taken into account in the calculations [24,25].

The Raman spectrum of 1.25×10^{-4} M phytochrome Cph1 in the P_r form excited at 790.4 nm is presented in Figure 4.5a. The most notable features are the coupled C=C and C–C torsions and in-plane twists at 664 cm^{-1}, C_5–H and C_{15}–H hydrogen-out-of-plane or HOOP wags at 793 and 810 cm^{-1}, respectively, vinyl N–H and C–H in-plane rocks at ~1315 cm^{-1}, the C=NH^+ stretch at 1568 cm^{-1} and the C=C stretch at 1630 cm^{-1}. The C=C stretch band has a poorly resolved shoulder at 1658 cm^{-1} which has been assigned to the C_4=C_5 (A–B ring) stretch, while the main peak at 1630 cm^{-1} represents a delocalized mode comprising the C_{15}=C_{16} methine bridge and the C_{17}=C_{18} double bond in the D-ring [26].

In the case of P_{fr}, due to the 70% P_r-to-P_{fr} photoconversion efficiency, the concentration of P_{fr} molecules in the sample was 8.75×10^{-5} M. The P_r contribution to the Raman spectrum was subtracted prior to analysis, and the pure P_{fr} spectrum is shown in Figure 4.5b. The most prominent bands in the P_{fr} spectrum are the coupled C=C and C–C torsions and in-plane twists at 658 cm^{-1}, the very intense C_{15}–H wag at 801 cm^{-1}, the N–H and C–H rocks and the C–C and C–N stretches in the 1300 cm^{-1} region, the in-phase in-plane N–H rock at 1547 cm^{-1} and the C=C stretch at 1607 cm^{-1}.

There are several notable differences between the P_r and P_{fr} Raman spectra. There is a marked change in the frequency and intensity of the C_{15}–H wagging mode upon isomerization – upon the conversion from P_r to P_{fr} the frequency of this mode blue-shifts from 793 to 801 cm^{-1} and is greatly enhanced. It is remarkable that a non-totally

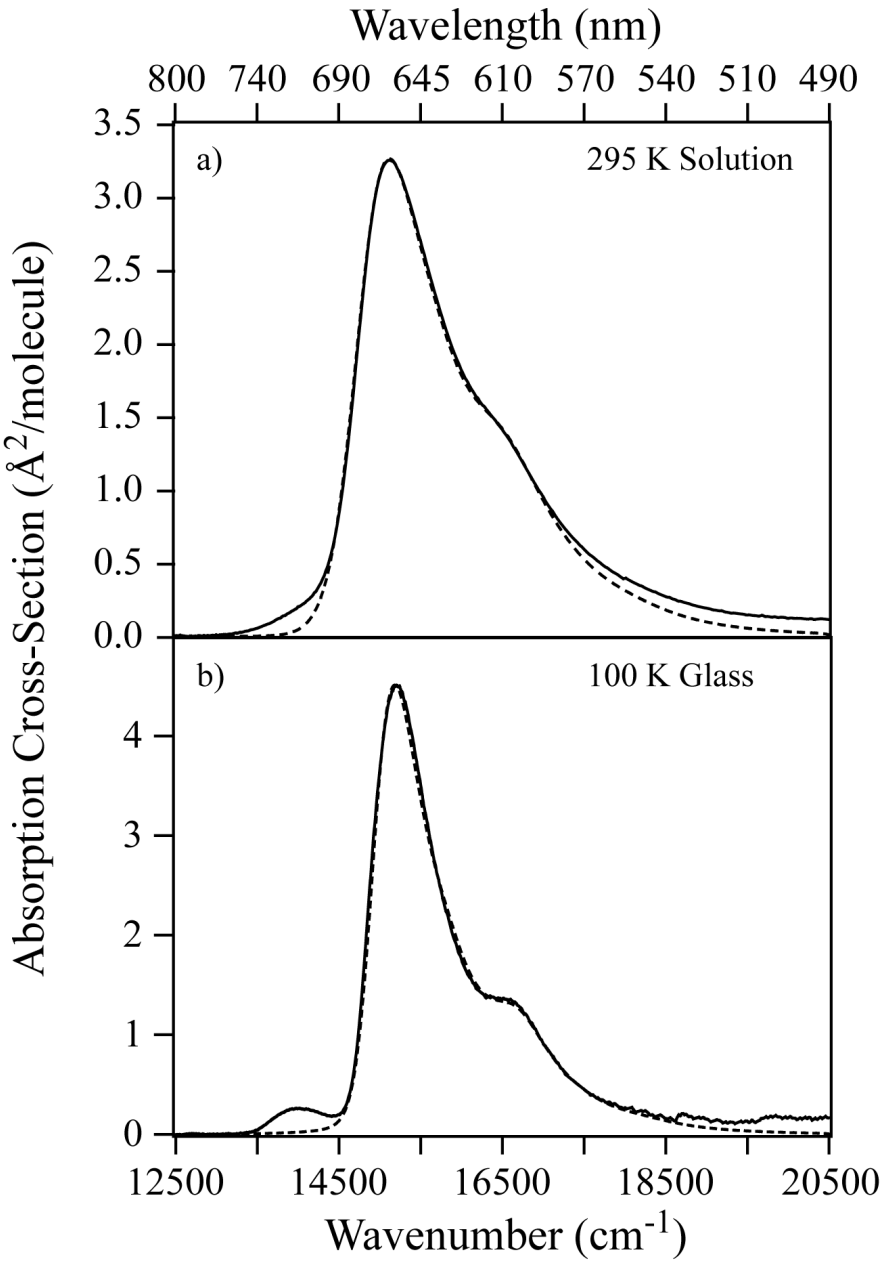

Figure 4.3. Absorption spectrum of the P_r form of phytochrome Cph1 at **a)** 295 K in TES-glycerol buffer (pH 8.0) and **b)** 100 K in TES-glycerol buffer mixed with glycerol at a v/v ratio of 35:65. The calculated curves are shown as dashed lines superimposed on the individual spectra and were determined using the parameters listed in Table 4.1.

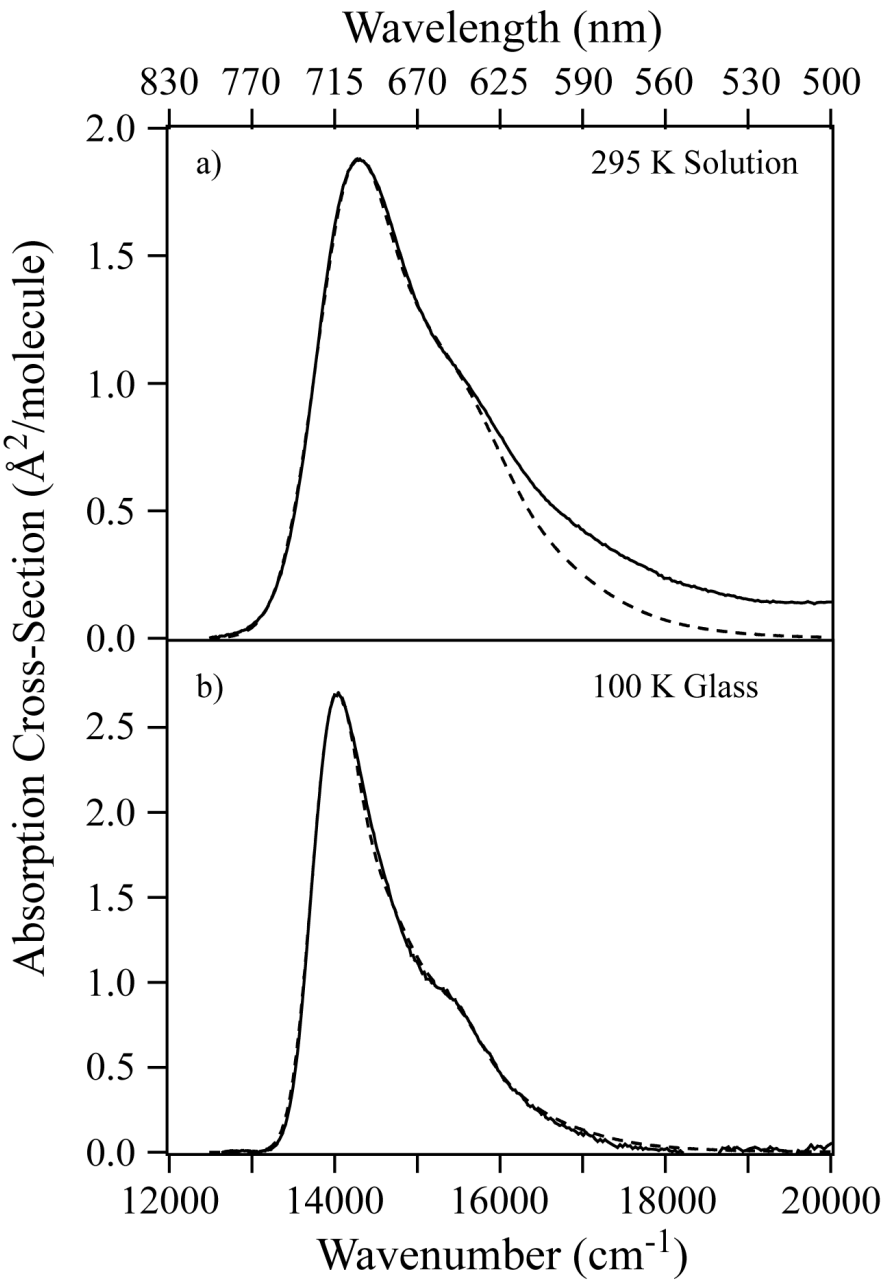

Figure 4.4. Absorption spectrum of the P_{fr} form of phytochrome Cph1 at **a)** 295 K in TES-glycerol buffer (pH 8.0) and **b)** 100 K in TES-glycerol buffer mixed with glycerol at a v/v ratio of 35:65. The calculated curves are shown as dashed lines superimposed on the individual spectra and were determined using the parameters listed in Table 4.2.

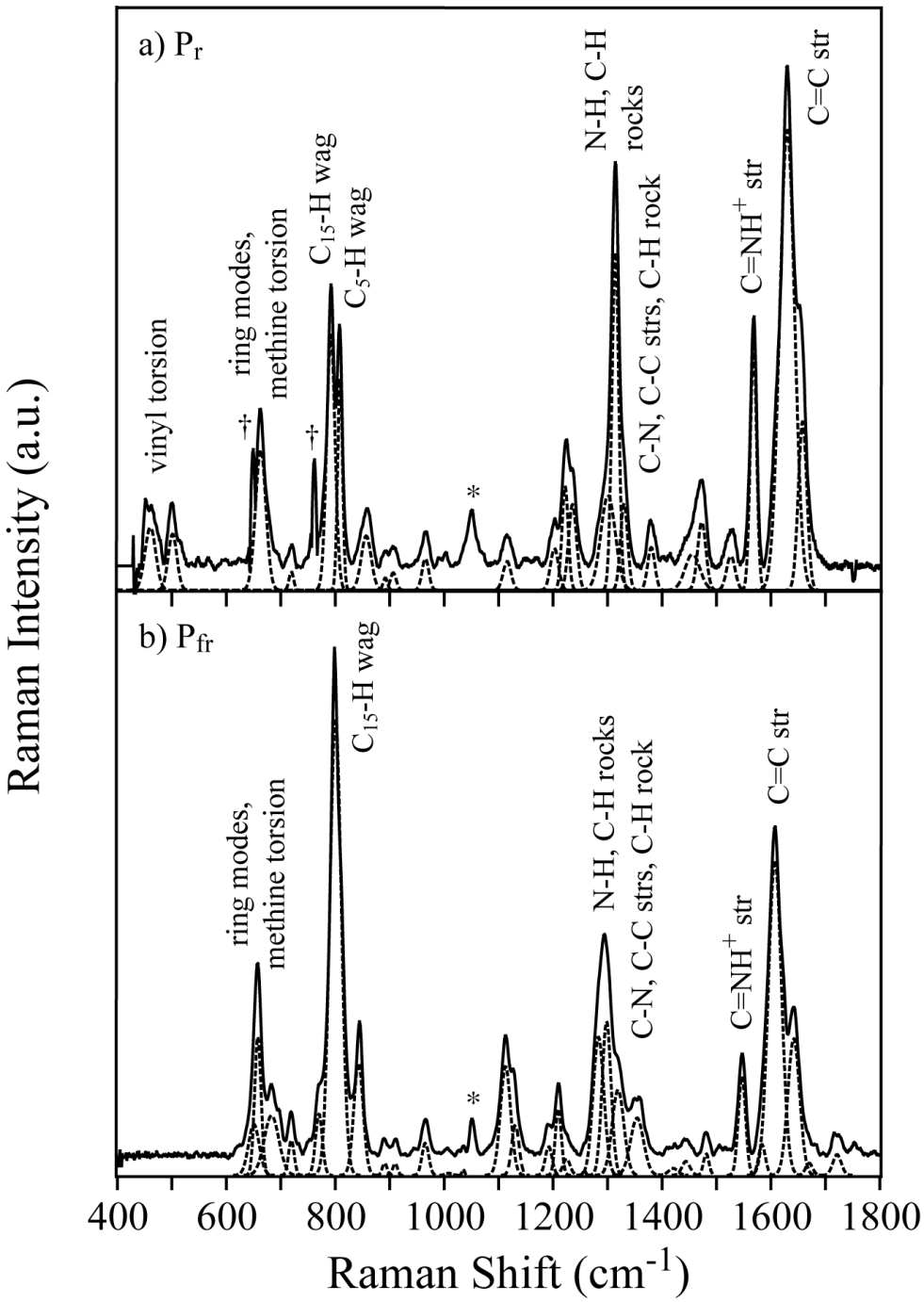

Figure 4.5. Stimulated Raman spectra (solid lines) of **a)** 1.25×10^{-4} M Cph1 P_r and **b)** 8.75×10^{-5} M Cph1 P_{fr} phytochrome obtained with a 3 μJ Raman pump pulse centered at 790.4 nm. Integrated areas of peak fits were used to determine the absolute Raman cross-sections presented in Tables 1 and 2 using the 1049 cm^{-1} symmetric stretch of NO_3^- as an external standard. The peaks at 1049 cm^{-1} indicated by an asterisk is due to the glycerol internal standard, and the features at 650 and 760 cm^{-1} indicated by a † are detector artifacts.

symmetric HOOP mode becomes the strongest resonance line in P_{fr}; this observation is generally indicative of a high degree of distortion in the C_{14}–C_{15}=C_{16} bond region [27]. In addition, the C=C stretch band is significantly red-shifted from 1630 to 1607 cm^{-1} in P_{fr}, pointing to a decrease in the C_{15}=C_{16} bond order.

Raman intensity calculations were performed to quantify the FC coupling of the vibrational modes with S_1 electronic excitation. The calculated displacements along the relevant vibrational modes for each isomer were optimized to reproduce their experimental Raman cross-sections (Tables 4.1 and 4.2) while simultaneously fitting their experimental absorption spectra. Figures 4.3 and 4.4 demonstrate the good agreement between the experimental absorption spectra (solid) and those calculated (dashed) using the parameters listed in Tables 4.1 and 4.2. The absorption spectra are broad and, particularly at room temperature, have poorly defined vibronic features, suggesting rapid excited-state dynamics and/or large inhomogeneous effects. Incorporating an inhomogeneous parameter of greater than 100 cm^{-1} in the 295 K calculations and greater than 50 cm^{-1} in the 100 K calculations produced unsatisfactory fits, leading us to conclude that the broad profile is due primarily to fast excited-state decay. For comparison, the homogeneous broadening parameters that provided the best fits to experimental data were 840 cm^{-1} at 295 K and 480 cm^{-1} at 100 K for P_r, and 1010 cm^{-1} at 295 K and 630 cm^{-1} at 100 K for P_{fr}. The greater amount of homogeneous broadening in P_{fr} points to faster excited-state decay in this conformer. The small amount of inhomogeneous broadening that is present in both P_r and P_{fr} is likely due to small fluctuations attributed to the diversity of similar (but not identical) interactions with a *single* chromophore binding environment.

The experimental Raman cross-sections and those determined from a 24-mode Raman intensity calculation for P_r are presented in Table 4.1. The experimental cross-sections of P_{fr} were modeled using a 31-mode vibronic analysis and these results are given in Table 4.2. Relative delta values were estimated assuming $I \propto \omega^2\Delta^2$ and the magnitude was adjusted to fit the overall width of the absorption spectrum. The homogeneous and inhomogeneous broadening parameters were adjusted to optimize the fit to the absorption band as described above. Efforts to model the data using a Lorentzian lineshape function whose width was large enough to produce the correct Raman cross-sections were unsuccessful because it predicted a large red-edge tail in the absorption spectrum that is inconsistent with experimental results. As a result, we used a Gaussian homogeneous lineshape function in the calculations. In addition, attempts to use larger relative values for the displacements resulted in absorption spectra that were too broad, and this breadth could not be reduced by any combination of homogeneous and inhomogeneous broadening parameters.

The most prominent modes in both the P_r and P_{fr} spectra are the HOOP, C–H rock and C=C stretch. In the case of P_r, the experimental cross-sections of the C_{15}–H HOOP and C_{15}=C_{16} stretch are 14.4×10^{-11} and 37.5×10^{-11} $Å^2$ $molecule^{-1}$, and in P_{fr} they are 118×10^{-11} and 75.8×10^{-11} $Å^2$ $molecule^{-1}$, respectively. While the cross-section of the P_{fr} C_{15}=C_{16} stretch is larger than that of P_r by a factor of ~2, the P_{fr} C_{15}–H HOOP is ~8.5 times larger than that of P_r. It is interesting to note that, with the exception of the P_{fr} C_{15}–H HOOP, the Δ values of each of these modes is ~ 0.4. For the P_{fr} C_{15}–H HOOP,

Table 1. Resonance Raman Cross-Sections of Cph1 (P_r)

frequency [cm^{-1}]	expt cross-section [$Å^2 \times 10^{-11}$][a]	calcd cross-section [$Å^2 \times 10^{-11}$]	delta [unitless][b]
461	4.96 ± 0.64	5.09	0.32 (0.29)
502	3.56 ± 0.57	3.66	0.25
664	10.2 ± 0.73	10.2	0.34 (0.31)
720	0.57 ± 0.38	0.64	0.08
793	14.4 ± 0.72	14.3	0.36 (0.32)
810	6.92 ± 0.49	6.91	0.25 (0.22)
858	3.60 ± 0.54	3.52	0.17
893	0.35 ± 0.43	0.34	0.05
907	0.66 ± 0.53	0.66	0.07
966	1.36 ± 0.42	1.36	0.10
1116	1.43 ± 0.44	1.32	0.09
1203	2.04 ± 0.64	1.93	0.10
1222	3.91 ± 1.51	3.86	0.14
1236	4.17 ± 1.40	4.04	0.15
1301	8.16 ± 2.92	8.19	0.20
1315	13.5 ± 2.61	13.6	0.26 (0.23)
1331	3.65 ± 0.97	3.49	0.13
1380	1.80 ± 0.38	1.70	0.09
1456	3.06 ± 2.35	2.96	0.12
1473	3.21 ± 2.31	3.27	0.12
1527	1.63 ± 0.39	1.53	0.08
1568	8.54 ± 0.33	8.55	0.19
1630	37.5 ± 0.78	37.4	0.39 (0.35)
1658	7.79 ± 0.41	7.79	0.18

Table 4.1. a) Raman cross-sections are relative to the 1049 cm^{-1} C–OH stretch of glycerol. The glycerol differential cross-section at λ_{ex} = 790.4 nm was 1.31 × 10^{-15} $Å^2$ $molecule^{-1}$ sr^{-1}. b) Delta values for the 295 K structure were determined with Γ = 840 cm^{-1}, θ = 60 cm^{-1}, E_0 = 14770 cm^{-1} and M = 2.31 Å. Delta values for the 100 K structure were determined using Γ = 480 cm^{-1}, θ = 50 cm^{-1}, E_0 = 14855 cm^{-1} and M = 2.32 Å and are shown in parentheses when they differ by > ±0.02 from the 295 K values.

Table 2. Resonance Raman Cross-Sections of Cph1 (P_{fr})

frequency [cm^{-1}]	expt cross-section [$Å^2 \times 10^{-11}$][a]	calcd cross-section [$Å^2 \times 10^{-11}$]	delta [unitless][b]
651	12.8 ± 13.7	12.7	0.24 (0.20)
658	21.0 ± 11.1	20.8	0.30 (0.26)
683	20.3 ± 1.99	20.2	0.29 (0.25)
719	4.53 ± 0.50	4.80	0.14
770	9.56 ± 0.48	9.46	0.19 (0.16)
801	118 ± 0.61	118	0.64 (0.54)
843	23.3 ± 0.53	23.3	0.28 (0.24)
891	1.25 ± 0.43	1.11	0.06
910	1.18 ± 0.42	1.28	0.06
965	4.70 ± 0.44	4.63	0.12
1008	0.26 ± 0.73	0.34	0.03
1035	0.31 ± 0.37	0.40	0.03
1113	23.2 ± 0.79	22.9	0.24 (0.21)
1131	7.60 ± 1.14	7.71	0.14
1192	3.98 ± 0.53	4.20	0.10
1210	8.11 ± 0.86	8.20	0.14
1225	2.41 ± 1.01	2.61	0.08
1283	29.7 ± 10.6	29.5	0.26 (0.22)
1298	27.4 ± 14.1	27.1	0.25 (0.21)
1319	19.7 ± 2.69	19.7	0.21 (0.18)
1354	14.6 ± 0.64	14.6	0.18 (0.15)
1420	1.21 ± 0.74	1.15	0.05
1444	2.10 ± 0.54	1.97	0.06
1481	2.23 ± 0.34	2.04	0.07
1547	13.3 ± 0.36	13.1	0.16
1584	3.85 ± 0.72	3.77	0.09
1607	75.8 ± 0.63	75.8	0.39 (0.33)
1642	29.1 ± 0.56	28.9	0.24 (0.20)
1670	1.51 ± 0.42	1.29	0.05
1721	3.06 ± 0.40	2.80	0.07
1754	1.05 ± 0.38	0.83	0.04

Table 4.2. a) Raman cross-sections determined relative to the 1049 cm^{-1} C–OH stretch of glycerol. The glycerol differential cross-section at λ_{ex} = 790.4 nm was 1.31×10^{-15} $Å^2$ $molecule^{-1}$ sr^{-1}. b) Delta values for the 295 K structure were determined with Γ = 1010 cm^{-1}, θ = 100 cm^{-1}, E_0 = 13735 cm^{-1} and M = 1.92 Å. Delta values for the 100 K structure were determined using Γ = 630 cm^{-1}, θ = 30 cm^{-1}, E_0 = 13525 cm^{-1} and M = 1.93 Å and are shown in parentheses when they differ by > ±0.02 from the 295 K values.

however, Δ was determined to be 0.64. A highly displaced HOOP wag is consistent with a nonplanar conformation of the C- and D-rings in the P_{fr} state [26]. Additional evidence of a distorted structure in this region is the decrease in double-bond character indicated by the large down-shift in the C_{15}=C_{16} stretch frequency from 1630 cm^{-1} in P_r to 1607 cm^{-1} in P_{fr}.

4.5 Discussion

The primary purpose of this study is to determine the structure and excited-state dynamics of the bilin chromophore during the photocycle of phytochrome Cph1. A clear picture of the ground-state structure is necessary for understanding the reaction pathway, while the early-time dynamics give insight into the mechanism by which the protein mediates photoisomerization. A particular point of interest is the difference in isomerization dynamics between the forward and back reactions: while the $P_r \rightarrow P_{fr}$ isomerization occurs in ~3 ps [4,6,28], the $P_{fr} \rightarrow P_r$ isomerization proceeds in <1 ps [5,7,8,29]. Here we use RR intensity analysis to address quantitatively the putative ground-state conformational heterogeneity [7,11-15] and to reveal the initial nuclear dynamics and mechanistic differences between the two reactions.

Simultaneous analysis of the absorption profiles and RR intensities allowed us to quantify the FC displacements (Δ values) of the Raman-active modes. In all cases, the calculated absorption spectra accurately model the experimental spectra, which are dominated by the 0–0 vibronic transition and have a shoulder on the blue edge near 600 nm in P_r and 645 nm in P_{fr} that is conclusively shown here to be a vibronic band due to the 0–1 transition. It is important to clarify that the blue shoulder is not due to a second chromophore species, but is instead a natural physical consequence of vibronic progressions in the absorption spectrum. The excellent modeling of the experimental data using a single set of parameters (given in Table 4.1 for P_r and Table 4.2 for P_{fr}) leads us to conclude that both P_r and P_{fr} exist as a single, homogeneous population of species in solution at the 10 cm^{-1} precision of our vibronic measurements. It is possible that the heterogeneity observed by other researchers may be the result of multiple photo-intermediate species present in the sample at the time of measurement.

The large Δ values in the C=C stretch, C_{15}–H HOOP wag, and C=C and C–C torsional modes indicate that there is a significant geometric change along these internal coordinates following photoexcitation. Because the isomerization occurs about the C_{15}=C_{16} bond, it is highly likely that the torsional reaction coordinate is dissociative, meaning that the system does not return to the FC region following excitation. By modeling the excited-state potential of the C_{15}=C_{16} torsion as a linear surface, the intensity of this mode can be used to make a crude prediction of the torsional isomerization time. Such an analysis was previously used to predict the 200 fs 11-*cis* → all-*trans* isomerization time of the 11-*cis* retinal chromophore in rhodopsin [30]. Based on DFT calculations, we assigned the C_{15}=C_{16} torsion to the mode at 664 cm^{-1} (Δ = 0.34) in P_r and 658 cm^{-1} (Δ = 0.30) in P_{fr}. If a wavepacket is propagated on the linear excited-state surface of a 664 cm^{-1} (Δ = 0.34) mode it will reach a dimensionless coordinate of

11, corresponding to a torsional angle of 90°, in only 65 fs [31]. Likewise, for a 658 cm^{-1} (Δ = 0.30) mode, the torsion will reach 90° in 70 fs. This analysis suggests that the isomerization could occur as fast as 130 fs in P_r and 140 fs in P_{fr} if torsional motions were the only consideration. However, this prediction is about an order of magnitude faster than experimental results, showing that a simple single mode analysis of isomerization is inadequate for phytochrome. In the $P_r \rightarrow P_{fr}$ reaction, the molecule moves quickly out of the FC region (~150 fs) but then reaches a local minimum on the S_1 surface due to the D-ring interaction with the protein that must be overcome to achieve isomerization [5]. The $P_{fr} \rightarrow P_r$ reaction is clearly faster, which is indicated by both the low fluorescence quantum yield ($\phi_f < 10^{-3} - 10^{-4}$) [32] and the short (~700 fs) excited-state lifetime [5], but its dynamics are still a factor of ~3 slower than what is predicted by torsional FC analysis. This analysis suggests that the P_{fr} S_1 potential energy surface also has a barrier due to frustrated D-ring rotation, resulting in a hindered crossing from the excited-state to the photoproduct. Although both P_r and P_{fr} likely encounter a steric barrier to isomerization, we predict that the >3× higher rate of $P_{fr} \rightarrow P_r$ photoconversion is due to the significantly enhanced P_{fr} C_{15}–H HOOP Δ and the ~20° pre-twist of the C_{14}–C_{15}=C_{16} moiety which reduces the distance the D-ring has to flip to form the photoproduct and increases its initial velocity out of the FC region.

The greatly enhanced Raman intensity and Δ in the P_{fr} 801 cm^{-1} C_{15}–H HOOP and 658 cm^{-1} torsional modes result from the loss of symmetry due to ground-state distortions about the C_{14}–C_{15} and C_{15}=C_{16} bonds caused by the C_{13}–CH_3 – C_{17}–CH_3 interaction. The large HOOP and torsional delta values, in turn, lead to fast excited-state dynamics along these coordinates following optical excitation. Using classical dynamics and assuming a linear excited-state surface, we calculated the geometry change along the 658 cm^{-1} torsional and 801 cm^{-1} C_{15}–H HOOP modes following excitation. As shown in Figure 4.6, during the first 20 fs of the reaction, the C_{14}–C_{15}=C_{16}–C_{17} torsional angle increases from 20° to 29° and the C_{15}–H moves from 12° to 42° out-of-plane. The phase of the torsion is chosen to swing the D-ring C_{17}–CH_3 group away from the steric clash with the C_{13}–CH_3 group on the C-ring. The phase of the C_{15}–H HOOP is chosen to be consistent with the increase in the C_{14}–C_{15} bond order upon $\pi \rightarrow \pi^*$ excitation. This motion also keeps the C_{15} hydrogen on the same side of the C_{15}=C_{16} bond during the isomerization and leads to the formation of the C_{15}-*Z,anti* configuration adopted in the P_r state. The C_{15}–H HOOP and torsional modes are not as dominant in the P_r form because P_r lacks the symmetry reducing methyl-methyl steric interaction.

The role of pre-twisting in rapid excited-state decay has been observed previously in the 11-*cis* retinal chromophore of rhodopsin [33]. In rhodopsin, the 11-*cis* retinal chromophore is distorted about the C_{10}–C_{11}, C_{11}=C_{12} and C_{12}–C_{13} bonds due to the C_{13}–CH_3 – C_{10}–H steric interaction, which lowers the structural symmetry and gives rise to highly displaced HOOP and torsional modes. Following optical excitation, the molecule undergoes rapid excited-state motion along the C_{11}H=C_{12}H HOOP and torsional coordinates and reaches the formally isomerized (>90°) photoproduct by 200 fs, although the overall structure is still highly distorted. The distortion introduced by the *cis-trans* isomerization is compensated by adjacent single- and double-bond twists so that the photoproduct shape is very similar to that of the reactant. This minimizes the disturbance

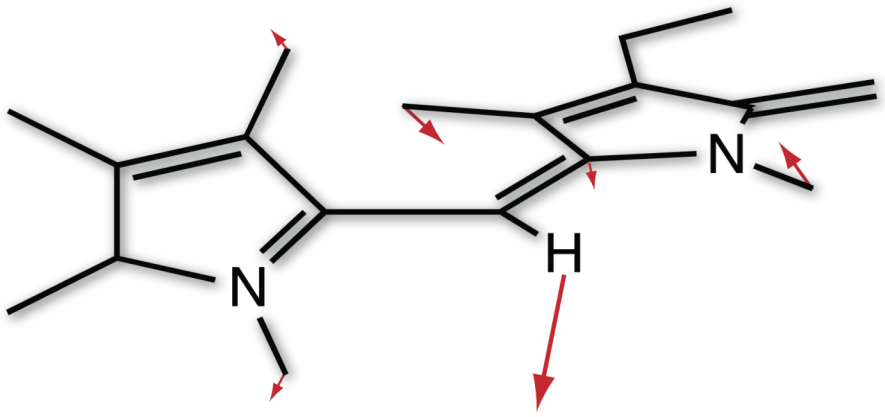

Figure 4.6. Representation of the initial geometric changes about the C- and D-rings of the excited P_{fr} form of phytochrome Cph1. The arrows indicate the geometry change along the torsional and C_{15}–H HOOP coordinates on a linear excited-state surface 20 fs after excitation. The phase of the torsion is chosen to swing the D-ring C_{17}–CH_3 group away from the steric clash with the C-ring. The phase of the C_{15}–H HOOP is chosen to be consistent with the increase in the C_{14}–C_{15} bond order upon $\pi \rightarrow \pi^*$ excitation; this motion also keeps the C_{15} hydrogen on the same side of the C_{15}=C_{16} bond during the isomerization.

to the chromophore binding pocket, thus allowing for the fast reaction rate and resultant high reaction quantum yield.

In contrast, the *Z*/*E* isomerization of the C_{15}=C_{16} methine bridge of the phycocyanobilin chromophore in phytochrome Cph1 is highly localized. Rings A – C are packed tightly in the binding pocket, and structural changes in the C_{14}–C_{15}=C_{16} region of the chromophore could not occur without associated dramatic changes in the surrounding protein [34] that are inconsistent with the short timescales discussed here. As such, early-time conformational changes are limited to the C_{14}–C_{15}=C_{16} methine bridge between the C and D rings; steric interaction between the D-ring and the protein prevents the molecule from completing a full isomerization by the <200 fs timescale predicted by a linear excited-state torsional potential. The slow reaction time relative to that predicted by FC dynamics is consistent with the low (15%) isomerization quantum yield [4]. As shown here, phytochrome has highly displaced HOOP and torsional modes that drive the molecule rapidly out of the FC region. This is analogous to rhodopsin, in which case the fast HOOP and torsional FC dynamics and barrier-free reaction pathway allow the 11-*cis* to all-*trans* isomerization of the retinal chromophore to proceed in 200 fs with 65% efficiency [35]. In contrast, the phytochrome bilin chromophore encounters a barrier on the excited-state surface due to frustrated D-ring rotation that results in a hindered isomerization which, despite getting off to an early fast start, is in the end relatively slow and inefficient.

4.6 Acknowledgments

We thank J. Clark Lagarias for providing the phytochrome Cph1 samples, Gabriela Schlau-Cohen for assistance with the low-temperature absorption measurements and Anne Myers Kelley for providing the RRModel program. This work was supported by the Mathies Royalty Fund.

4.7 References

[1] N. C. Rockwell, Y. S. Su and J. C. Lagarias, *Annu. Rev. Plant Biol.* **57,** 837 (2006).

[2] J. C. Lagarias and H. Rapoport, *J. Am. Chem. Soc.* **102,** 4821 (1980).

[3] P. H. Quail, *Nat. Rev. Mol. Cell Biol.* **3,** 85 (2002).

[4] J. Dasgupta, R. R. Frontiera, K. C. Taylor, J. C. Lagarias and R. A. Mathies, *Proc. Natl. Acad. Sci. U.S.A.* **106,** 1784 (2009).

[5] K. Heyne, J. Herbst, D. Stehlik, B. Esteban, T. Lamparter, J. Hughes and R. Diller, *Biophys. J.* **82,** 1004 (2002).

[6] J. J. van Thor, K. L. Ronayne and M. Towrie, *J. Am. Chem. Soc.* **129,** 126 (2007).

[7] M. Bischoff, G. Hermann, S. Rentsch and D. Strehlow, *Biochemistry* **40,** 181 (2001).

[8] M. Bischoff, G. Hermann, S. Rentsch and D. Strehlow, *J. Phys. Chem. A* **102,** 4399 (1998).

[9] A. B. Myers and R. A. Mathies, in *Biological Applications of Raman Spectroscopy,* T. G. Spiro, Ed. (John Wiley & Sons, New York, 1987), Vol. 2, p.1.

[10] D. L. Correll, J. L. Edwards and W. Shropshire, *Photochem. Photobiol.* **8,** 465 (1968).

[11] J. B. Nieder, M. Brecht and R. Bittl, *J. Am. Chem. Soc.* **131,** 69 (2009).

[12] P. Schmidt, T. Gertsch, A. Remberg, W. Gärtner, S. E. Braslavsky and K. Schaffner, *Photochem. Photobiol.* **68,** 754 (1998).

[13] D. von Stetten, M. Günther, P. Scheerer, D. H. Murgida, M. A. Mroginski, N. Krauβ, T. Lamparter, J. Zhang, D. M. Anstrom, R. D. Vierstra, K. T. Forest and P. Hildebrandt, *Angew. Chem. Int. Ed.* **47,** 4753 (2008).

[14] A. R. Holzwarth, E. Venuti, S. E. Braslavsky and K. Schaffner, *Biochim. Biophys. Acta* **1140,** 59 (1992).

[15] C. Song, G. Psakis, C. Lang, J. Mailliet, W. Gärtner, J. Hughes and J. Matysik, *Proc. Natl. Acad. Sci. U.S.A.* **108,** 3842 (2011).

[16] K. M. Spillane, J. Dasgupta, J. C. Lagarias and R. A. Mathies, *J. Am. Chem. Soc.* **131,** 13946 (2009).

[17] G. A. Gambetta and J. C. Lagarias, *Proc. Natl. Acad. Sci. U.S.A.* **98,** 10566 (2001).

[18] D. W. McCamant, P. Kukura, S. Yoon and R. A. Mathies, *Rev. Sci. Instrum.* **75,** 4971 (2004).

[19] T. Lamparter, F. Mittmann, W. Gärtner, T. Börner, E. Hartmann and J. Hughes, *Proc. Natl. Acad. Sci. U.S.A.* **94,** 11792 (1997).

[20] J. M. Dudik, C. R. Johnson and S. A. Asher, *J. Chem. Phys.* **82,** 1732 (1985).

[21] S. Y. Lee and E. J. Heller, *J. Chem. Phys.* **71,** 4777 (1979).

[22] J. Tang and A. C. Albrecht, in *Raman spectroscopy: theory and practice*, H. A. Szymanski, Ed. (Plenum, New York, 1970), Vol. 2, p. 33.

[23] T. Lamparter, B. Esteban and J. Hughes, *Eur. J. Biochem.* **268,** 4720 (2001).

[24] R. A. Matute, R. Contreras, G. Pérez-Hernández and L. González, *J. Phys. Chem. B* **112,** 16253 (2008).

[25] B. Borucki, H. Otto, G. Rottwinkel, J. Hughes, M. P. Heyn and T. Lamparter, *Biochemistry* **42,** 13684 (2003).

[26] F. Andel III, J. T. Murphy, J. A. Haas, M. T. McDowell, I. van der Hoef, J. Lugtenburg, J. C. Lagarias and R. A. Mathies, *Biochemistry* **39,** 2667 (2000).

[27] G. Eyring, B. Curry, R. Mathies, R. Fransen, I. Palings and J. Lugtenburg, *Biochemistry* **19,** 2410 (1980).

[28] S. Rentsch, G. Hermann, M. Bischoff, D. Strehlow and M. Rentsch, *Photochem. Photobiol.* **66,** 585 (1997).

[29] S. Rentsch, M. Bischoff, G. Hermann and D. Strehlow, *Appl. Phys. B* **66,** 259 (1998).

[30] G. R. Loppnow and R. A. Mathies, *Biophys. J.* **54,** 35 (1988).Myers, A. B., and Mathies, R. A. 1984. Excited-state torsional dynamics of *cis*-stilbene from resonance Raman intensities. J. Chem. Phys. 81:1552-1558.

[31] A. B. Myers and R. A. Mathies, *J. Chem. Phys.* **81,** 1552 (1984).

[32] V. A. Sineshchekov, *Biochim. Biophys. Acta* **1228,** 125 (1995).

[33] P. Kukura, D. W. McCamant, S. Yoon, D. B. Wandschneider and R. A. Mathies, *Science* **310,** 1006 (2005).

[34] L. –O. Essen, J. Mailliet and J. Hughes, *Proc. Natl. Acad. Sci. U.S.A.* **105,** 14709 (2008).

[35] J. E. Kim, M. J. Tauber and R. A .Mathies, *Biochemistry* **40,** 13774 (2001).

Chapter 5

Conical intersection dynamics of the primary photoisomerization event in vision

Reprinted with permission from the manuscript by Dario Polli, Piero Altoè, Oliver Weingart, Katelyn M. Spillane, Cristian Manzoni, Daniele Brida, Gaia Tomasello, Giorgio Orlandi, Philipp Kukura, Richard A. Mathies, Marco Garavelli and Giulio Cerullo
Nature **467,** 440–443 (2010).

5.1 Abstract

Ever since the conversion of the 11–*cis* retinal chromophore to its all–*trans* form in rhodopsin was identified as the primary photochemical event in vision [1], experimentalists and theoreticians have tried to unravel the molecular details of this process. The high quantum yield of 0.65 [2], the production of the primary ground–state rhodopsin photoproduct within a mere 200 fs [3–7], and the storage of considerable energy in the first stable bathorhodopsin intermediate [8] all suggest an unusually fast and efficient photoactivated one–way reaction [9]. Rhodopsin's unique reactivity is generally attributed to a conical intersection between the potential energy surfaces of the ground and excited electronic states [10,11] enabling the efficient and ultrafast conversion of photon energy into chemical energy [12-16]. But obtaining direct experimental evidence for the involvement of a conical intersection is challenging: the energy gap between the electronic states of the reacting molecule changes significantly over an ultrashort time–scale, which calls for observational methods that combine high temporal resolution with a broad spectral observation window. Here we show that ultrafast optical spectroscopy with sub–20–fs time resolution and spectral coverage from the visible to the near–infrared allows us to follow the dynamics leading to the conical intersection in rhodopsin isomerization. We track coherent wave–packet motion from the photoexcited Franck–Condon region to the photoproduct by monitoring the loss of reactant emission and the

subsequent appearance of photoproduct absorption, and find excellent agreement between the experimental observations and molecular dynamics calculations that involve a true electronic state crossing. Taken together, these findings constitute the most compelling evidence to date for the existence and importance of conical intersections in visual photochemistry.

5.2 Introduction

We initiated the photoisomerization reaction in the retinal chromophore of purified rhodopsin by 10–fs 500–nm pump pulses resonant with the ground–state absorption. The photoinduced dynamics were then probed by delayed ultra–broadband few–optical–cycle probe pulses, either in the visible wavelength region (500–720 nm) or in the near–infrared (NIR, 820–1,020 nm), generated by synchronized optical parametric amplifiers [17]. The temporal resolution was <20 fs over the entire monitored spectral range. Figure 5.1a presents a differential transmission ($\Delta T/T$) map as a function of probe wavelength and pump–probe time delay. Immediately following excitation from the ground state (S_0) to the first excited singlet state (S_1), we observed a positive $\Delta T/T$ signal (blue in the figure) with maximum intensity at ~650 nm, which is assigned to stimulated emission from the excited state due to the negligible ground–state absorption in this wavelength range. The stimulated emission signal rapidly shifts to the red while losing intensity and disappearing to wavelengths longer than 1,000 nm within ~75 fs. At this time, the $\Delta T/T$ signal changes sign and transforms into a weak photoinduced absorption signal (red in the figure), which initially appears at 1,000 nm and then gradually shifts to the blue and increases in intensity. For delays longer than 200 fs, the photo–induced absorption signal stabilizes as a long–lived band peaking at 560 nm, indicating the formation of the all–*trans* photoproduct [3]. We emphasize that the use of a sub–15–fs NIR probe is the key to observing the transition between the excited and ground electronic states. Time traces at selected probe wavelengths are shown in Fig. 5.1b, highlighting the red shift of the stimulated emission signal and the subsequent blue shift of the photoinduced absorption.

To extract a dynamic model of the photoinduced process from these data, we simulated the transient signals by using scaled complete active space–self consistent field (CASSCF) transition energies over hybrid quantum–mechanical (QM, CASSCF)/molecular–mechanical (MM) trajectories following the evolution of the opsin–embedded chromophore from the excited to the ground electronic state. Similar methods have been previously used to track photoinduced dynamics in rhodopsin [14,15,18] and other biomolecules [19-23]. This approach approximates full non–adiabatic complete active space with second–order perturbation theory (CASPT2) dynamics [24] that are currently possible only for smaller systems [25]. Our virtual spectroscopies and dynamics (Fig. 5.1c and d) agree almost quantitatively with the experimental results, owing to the inclusion of both the steric and electrostatic interactions within the retinal binding pocket (at the MM and QM level, respectively). The same holds for the 61% photoisomerization quantum yield and the average $S_1 \rightarrow S_0$ hopping time (~110 fs) extracted from the simulations, which further support the reliability of the theoretical approach.

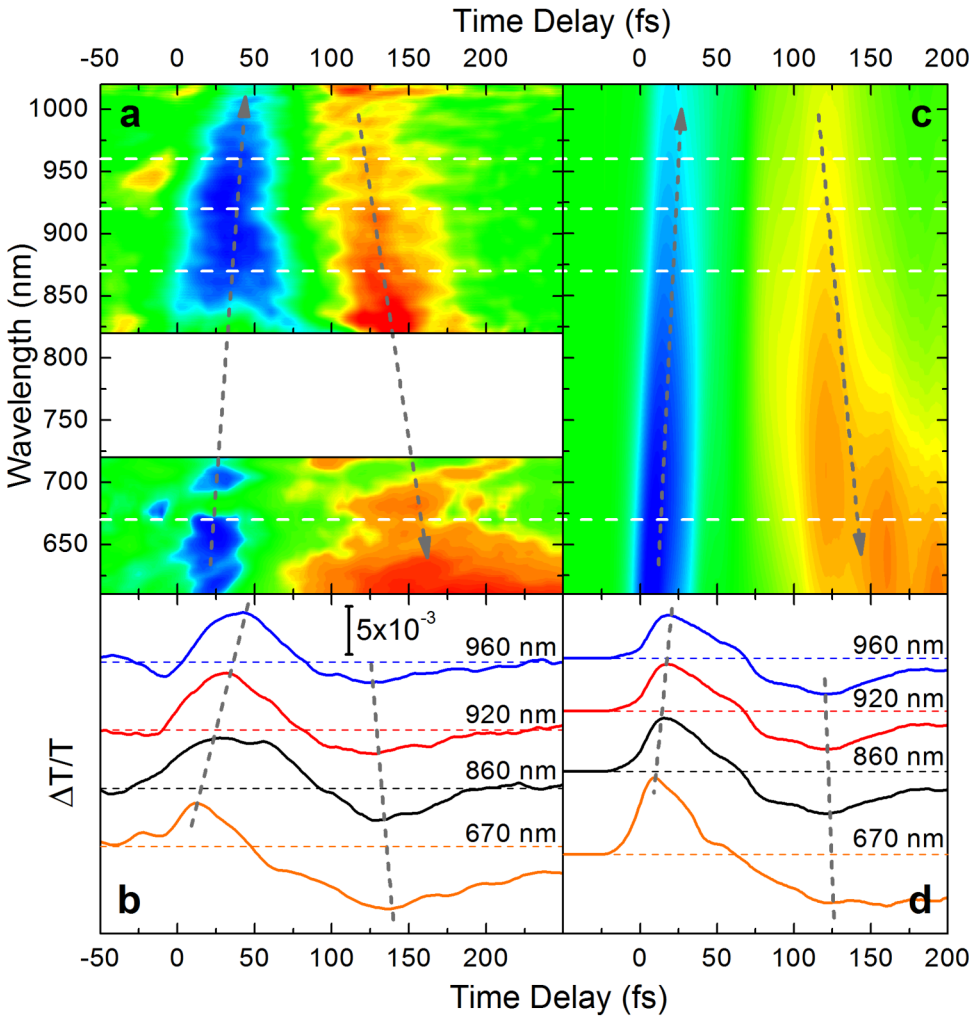

Figure 5.1. Wavepacket dynamics through the rhodopsin conical intersection. a, c, Experimental (**a**) and simulated (**c**) differential transmission (ΔT/T) map as a function of time delay and wavelength in the visible and NIR spectral regions. The white area in the experimental data around 750 nm corresponds to the 'blind region' of our setup. Grey lines are guides to the eye, highlighting the temporal shifts of the stimulated emission (blue) and photoinduced absorption (red/orange) signals. **b, d,** Experimental (**b**) and simulated (**d**) ΔT/T dynamics at selected probe wavelengths.

5.3 Results

The ultrafast complex spectral evolution observed both experimentally and theoretically can be understood qualitatively with the help of Fig. 5.2a. Here, the motion of the wave packet is depicted along the ground–state and excited–state potential energy surfaces of the rhodopsin chromophore as a function of the isomerization coordinate. The wave packet initially created in the Franck–Condon region of the excited state of the 11–*cis* reactant rapidly evolves along the reaction pathway towards the conical intersection, and the stimulated emission progressively shifts to the red as the energy gap between the excited and ground states narrows. Near the conical intersection region, which is reached in ~80 fs according to both experiment and theory, the stimulated emission signal vanishes as the two surfaces approach each other and the transition dipole moment decreases. Following the 'jump' to the hot ground state of the photoproduct, a symmetric photoinduced absorption signal is formed. This photoinduced absorption band rapidly shifts to the blue as the surfaces move away from each other energetically and the wave packet relaxes to the bottom of the photoproduct well, reflecting the redistribution of the excess energy deposited in the molecule and the final torsional movement to the all–*trans* configuration [26].

To complete the description of photoinduced dynamics in rhodopsin, we report the portion of the ΔT/T map probing the response of the system in the visible region, from 495 nm to 610 nm (Fig. 5.3a). In agreement with previous studies [3,27], we observe the delayed formation of the photoinduced absorption band of the photorhodopsin photo–product, which peaks at 560 nm and is complete within 200–250 fs. The signal does not display exponential build–up dynamics, but appears rather abruptly, starting at ~150 fs (see time trace at 550 nm in Fig. 5.3b), which is the time needed for the wave packet to cross the conical intersection and enter the probed wavelength window on the photoproduct side. The blue region of the spectrum is dominated by the photobleaching signal from the ground state of the parent rhodopsin molecule, peaking at ~510 nm. These two spectral signatures partially overlap, so that the photobleaching band shrinks in time as the photoinduced absorption signal forms and blue–shifts. The amplitude of the photobleaching band also decreases owing to the return of 35% of the excited state population back to the ground state of the 11–*cis* reactant. At early probe delays, a photoinduced absorption band peaking at ~500 nm is evident (see time trace in Fig. 5.3b), corresponding to a transition from the Franck–Condon excited state to a higher–lying S_n state [3], having a greater dipole moment than the ground state photobleaching band. This band disappears within ~50 fs, owing to the wave–packet motion out of the Franck–Condon region. Over longer timescales (see Supplementary Fig. B.8 and Supplementary Discussion), the photoproduct photoinduced absorption signal displays vibrational coherence with a ~550–fs period (~60–cm^{-1} frequency). The probe–wavelength dependence of the amplitude and phase of this vibration is consistent with a wave packet moving in the ground state of the photoproduct, in agreement with previous observations [27].

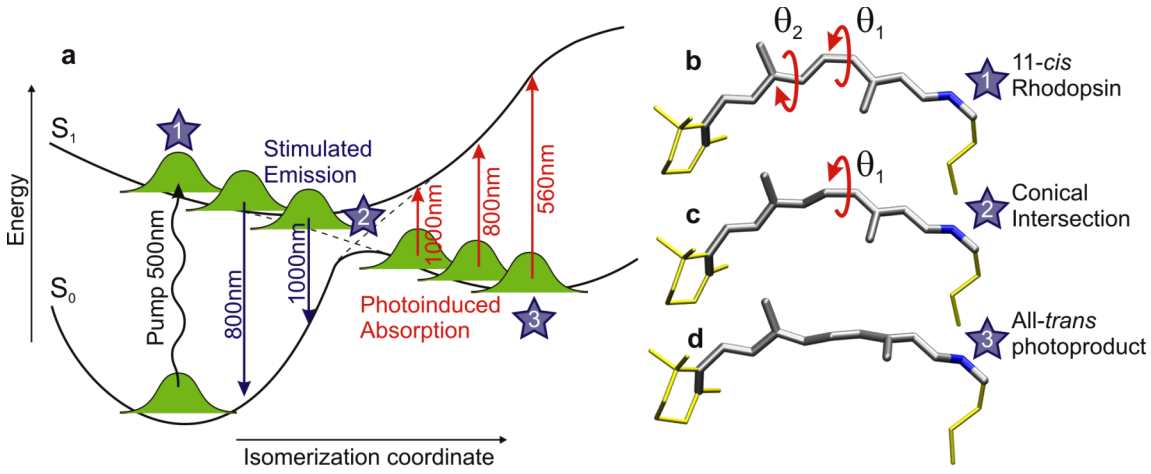

Figure 5.2. Isomerization potential energy surfaces of rhodopsin. a, Sketch of the ground- and excited-state potential energy surfaces of the chromophore in rhodopsin as a function of the isomerization coordinate. Wavy arrow indicates photoexcitation, straight arrows correspond to stimulated emission (blue) or photoinduced absorption (red/orange). The graph shows that stimulated emission from the excited state of the parent molecule and photoinduced absorption from the hot photoproduct can monitor the wave-packet dynamics through the conical intersection. **b–d,** Averaged structures of the chromophore at the initial 11-*cis* (**b**) (blue star '1', t = 0 fs, $\theta_1 = -12.8°$, $\theta_2 = 173.9°$), conical intersection (**c**) (blue star '2', t = 110 fs, $\theta_1 = -87.8°$, $\theta_2 = -144.6°$) and final all-*trans* (**d**) (blue star '3', t = 200 fs, $\theta_1 = -141.0°$, $\theta_2 = -142.0°$) configurations; grey/yellow colours indicate the chromophore QM/MM regions in the simulations.

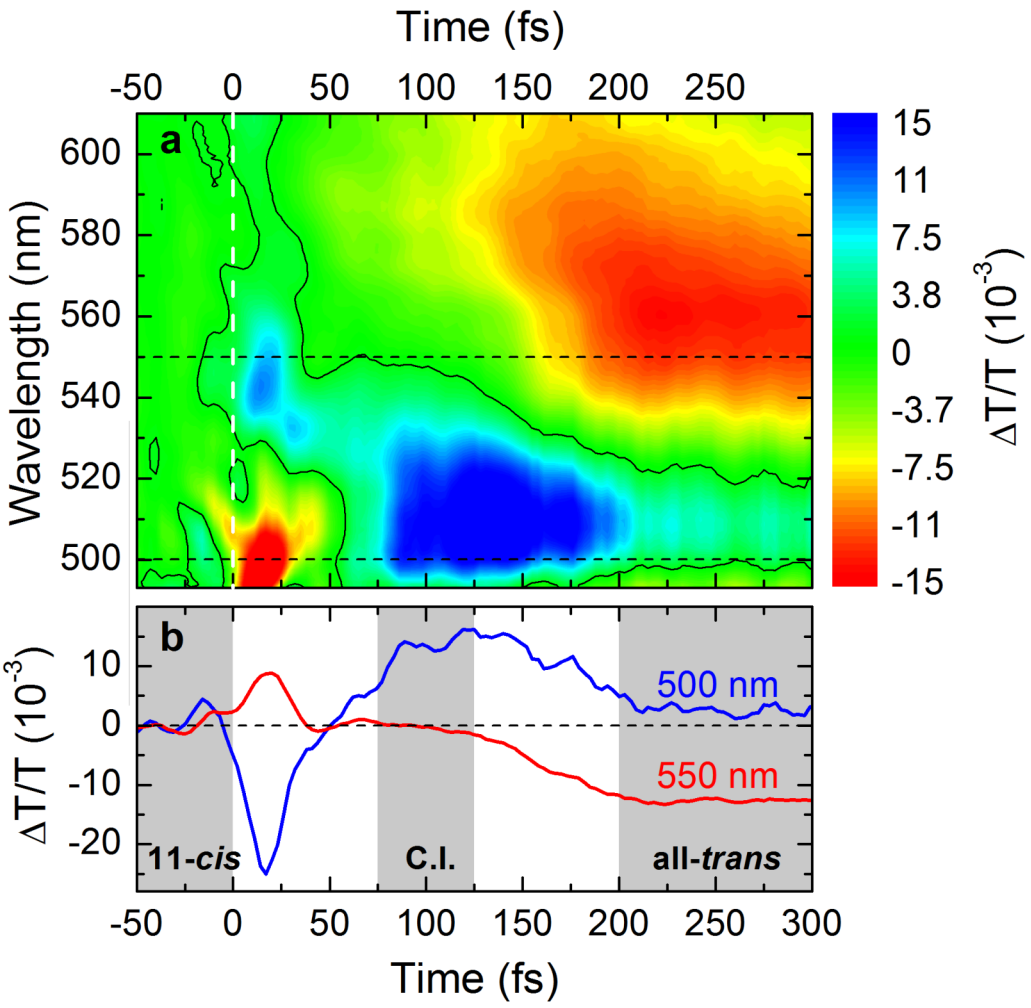

Figure 5.3. Rhodopsin isomerization probed in the visible spectral range. a, ΔT/T map in the visible spectral region. **b,** Time traces at 500 nm and 550 nm probe wavelengths; central grey area labelled CI indicates the approximate conical intersection occurrence between the initial 11–*cis* configuration (left grey area) and the final all-*trans* (right grey area; reached in ~200 fs).

5.4 Discussion

The extremely high experimental time resolution combined with the remarkable agreement with theory makes it possible to confidently predict the real–time structural changes occurring within the first 200 fs of retinal isomerization in rhodopsin. The Supplementary Movie shows the evolution of the reacting retinal structure during the first 200 fs, averaged over the isomerizing and non–isomerizing trajectories in the top and bottom movie panels, respectively. Here, we focus on the key structures, namely the 11–*cis* reactant, the structure of retinal at the conical intersection and the all–*trans* photoproduct (Fig. 5.2b–d). Comparison of the retinal structure in the ground state (Fig. 5.2b) with the structure at the conical intersection (Fig. 5.2c) reveals dramatic changes only in the vicinity of the isomerizing bond. We found that the average C_{11}=C_{12} dihedral angle at the conical intersection is $\theta_1 = -87.8°$ (Fig. 5.2c), ranging from –75° to –105° for individual trajectories, emphasizing the relevance of the C_{11}=C_{12} twist in triggering internal conversion. At the same time, the C_9=C_{10} torsional angle θ_2 also exhibits a large change (by ~45°) on the excited–state surface as the wave packet moves towards the conical intersection (Fig. 5.2c). This torsion also persists on the photo–product side (Fig. 5.2d), accounting for chromophore ends that are motionless during the isomerization process (yellow portions in Fig. 5.2b–d), in agreement with structures derived from femtosecond stimulated Raman scattering [26] and reminiscent of the 'bicycle pedal' proposal for retinal isomerization in rhodopsin [28,29]. Notably, all trajectories reach the S_1/S_0 crossing region and decay to S_0, from which they rapidly branch and immediately move towards their final ground state configuration: 61% yield the all–*trans* product ($\theta_1 < -140°$), while 39% result in a frustrated isomerization and return to the *cis* reactant ($\theta_1 < 215°$).

5.5 Conclusions

Taken together, these data indicate that the structural evolution from the reactant towards the conical intersection is restricted almost exclusively to the atoms in the centre of the molecule. This behaviour is promoted by the tight binding pocket provided by the protein for the chromophore, which restricts the possible motion at its ends [30]. Therefore, retinal can use all of the incident photon energy to drive minimal atomic displacements in the C_9=C_{10}–C_{11}=C_{12} region and reach the conical intersection region within 80 fs, resulting in a very fast reaction speed. Once the local isomerization has taken place, the overall highly strained structure can then rapidly relax either in the photoproduct well, resulting in the more *trans*–like structure that completes the primary isomerization reaction (major component), or back to the 11–*cis* starting reactant (minor component). The close agreement between our experimental data and theoretical simulations indicates that the resulting molecular movie of the photoisomerization process, generated with atomistic detail and femtosecond time resolution, indeed reveals the complete dynamics of this classical conical intersection reaction that initiates vision.

5.6 Methods Summary

A. Ultrafast spectroscopy

An amplified Ti:sapphire laser system delivering 150–fs pulses at 790 nm and 1 kHz feeds three independent, synchronized non–collinear optical parametric amplifiers (NOPAs) [17]. The first generates 10–fs pulses centred at 520 nm (with 55–nm bandwidth) that are used to pump rhodopsin. The second and third NOPAs generate the probe pulses in the visible (500–750 nm, 7 fs) and in the NIR (820–1,020 nm, 13 fs). The sample is contained in a ~300–μm–pathlength cuvette and is flowed rapidly to ensure complete replacement between consecutive pulses. A fast spectrometer enables single–shot recording of the probe spectrum. Control runs on the buffer solution confirmed that the observed dynamics are solely due to rhodopsin molecules. Temporal resolution was limited by group–delay mismatch between pump and probe pulses in the cuvette to ~13 fs and ~18 fs at 700 nm and 900 nm, respectively.

B. Numerical simulations

Protein set–up (1U19 PDB code) [30] is documented elsewhere [16]. QM(CASSCF(10,10)/6–31G*)/MM(Amber99ff) calculations account for the chromophore/protein electrostatic (steric) interactions at the highest QM (MM) level. Figure 5.2 highlights the chromophore QM/MM regions that, together with the two neighbouring water molecules, are mobile. All other atoms are fixed at their crystallographic positions, a choice that is supported by the sub–200–fs reaction timescale and recent computational evidence [15]. A thermal sample (300 K) of 38 initial conditions is used. A velocity Verlet algorithm (step size $\leq$ 0.5 fs) is applied to propagate trajectories, at constant energy, by equally weighting the first three roots in a state average CAS(10/10) procedure. $S_1 \rightarrow S_0$ decay occurs according to the scalar product of the S_1 and S_0 state coefficients ($\Delta E_{S0/S1} < 2.2$ kcal mol^{-1} at hopping). CASSCF data for $S_1 \rightarrow S_0$, $S_1 \rightarrow S_2$ and $S_0 \rightarrow S_1$ transitions from individual trajectories are convolved with a 20–fs FWHM (full–width at half–maximum) Gaussian function and scaled to match CASPT2–corrected energy gaps.

5.7 Acknowledgments

M.G., O.W., G.O., G.T. and P.A. thank E4–Computer Engineering S.p.A. for computational time and technical assistance. Part of this study was financially supported by the DFG (FOR490) and by the PRIN programme (2008JKBBK4). P.K. is supported by a Career Acceleration Fellowship awarded by the UK Engineering and Physical Sciences Research Council (EP/H003541/1).

5.8 Methods

A. Sample preparation

Rhodopsin molecules were extracted from the rod outer segments of bovine retinae and purified by sucrose flotation followed by sucrose density gradient centrifugation, as described elsewhere [31]. The OD_{280}/OD_{500} absorbance ratio was less than 1.8. Fresh NH_2OH was added to a final concentration of 2 mM.

B. Pump-probe spectroscopy

Supplementary Fig. B.1 shows the schematic experimental set–up. It starts with a regeneratively amplified mode–locked Ti:sapphire laser system (Clark–MXR model CPA–1) delivering pulses with 150–fs duration, 500–μJ energy, at 1–kHz repetition rate and 780–nm central wavelength. The system drives three independent non–collinear optical parametric amplifiers (NOPAs) [17] in the visible and in the NIR, which generate the pump and the probe pulses for the time–resolved experiments. The first NOPA (NOPA1) generates the pump pulses in the 500– to 550–nm wavelength region in order to selectively excite the rhodopsin molecule in resonance with its ground–state absorption. The second and third NOPAs are used alternatively to generate the probe pulses in the visible (NOPA2, from 500 nm to 750 nm) or in the NIR frequency range (NOPA3, from 820 nm to 1,020 nm). NOPA1 and NOPA2 are compressed to their transform–limited (TL) duration by multiple bounces on custom–designed chirped mirrors, while NOPA3 is compressed to the TL by a Brewster–cut fused–silica prism pair. The pulse durations, retrieved using the frequency–resolved optical gating (FROG) technique, are 10 fs for NOPA1, 7 fs for NOPA2 and 13 fs for NOPA3. Supplementary Fig. B.2 shows typical spectra from the three NOPAs.

The sample is contained in a cuvette with 250–μm–thick fused–silica windows and ~300–μm optical path. The sample thickness ultimately determines our experimental temporal resolution due to group–delay mismatch between the pump pulse (in the blue) and the probe pulse (in the red/NIR): when the pump and probe pulses are perfectly synchronized (time zero) at the front face of the sample, they will be delayed at the sample exit, thus smearing out the measured time traces. The calculated group delay mismatch is 12.7 fs at 700 nm and 17.4 fs at 900 nm (considering the dispersion relations of water).

After the sample, the probe beam is selected by an iris and focused onto the entrance slit of a spectrometer equipped with a 1,024–pixel linear photodiode array and electronics specially designed for fast read–out times and low noise [32]. The spectral resolution of the spectrograph (about 2 nm) is more than sufficient for our experiments. A fast analogue–to–digital conversion card with 16–bit resolution enables single–shot recording of the probe spectrum at the full 1–kHz repetition rate. By recording pump–on and pump–off probe spectra, we can calculate the $\Delta T/T$ spectrum at the specific probe delay τ as:

$$\Delta T/T(\lambda,\tau) = [T_{on}(\lambda,\tau) - T_{off}(\lambda)]/T_{off}(\lambda)$$

By repeating this procedure for a few hundred milliseconds and averaging the resulting signals, it is thus possible to achieve a high enough signal–to–noise ratio to detect $\Delta T/T$ spectra down to the 10^{-4} level over the whole probe wavelength range. By moving the translation stage we record $\Delta T/T$ spectra at different probe delays, thus obtaining a complete two–dimensional map: $\Delta T/T = \Delta T/T(\lambda,\tau)$.

The absorption spectrum of rhodopsin, peaking at ~500 nm, is plotted in Supplementary Fig. B.2 as a shaded curve. To prevent the accumulation of photoproduct in the irradiated volume, the sample was continuously re–circulated by means of a peristaltic pump in a closed–loop circuit with ~4 ml total volume to ensure complete replacement of the sample in the focal volume for each consecutive laser shot. The excitation fluence was chosen so as to be in a perturbative regime, with maximum $|\Delta T/T|$ of the order of 1–2%.

To ensure that the signal is only due to the rhodopsin molecule, we also performed pump–probe experiments, in exactly the same experimental conditions, on two different samples: (1) the buffer alone and (2) the fully bleached rhodopsin solution obtained by stopping the flow. In both cases, the transient signal disappeared except for the coherent artefact around time zero, which was subtracted from the data.

C. QM/MM calculations and protein setup

CASPT2//CASSCF/6–31G*/AMBER QM/MM [33] computations are performed using the COBRAMM interface [34] implemented by our group, using a hydrogen link–atom scheme [35] and linking the Molpro [36], MOLCAS–6.0 [37] and AMBER8 [38] packages. Details of the approach have been presented elsewhere [34]. Other applications involving this methodology may be found in refs 16, 39. Geometry optimizations, frequency calculations and molecular dynamics involve ab initio CASSCF/6–31G* computations [40] for the QM region. The AMBER8 software and the *ff99* force field [38] are used for the MM region and its charges. During all calculations the retinal chromophore, the region between Schiff base nitrogen and the Cβ–carbon of Lys 296, and the two neighbouring water molecules are mobile. The remaining atoms are fixed at their positions in the protein crystal (1U19 PDB code). Two different chromophore QM/MM–models have been used here, a full chromophore set–up for optimizations and static isomerization path mapping, and a reduced chromophore model for molecular dynamics simulations. In the full chromophore the QM–MM frontier is placed at the Cδ–Cε bond of the Lys296 side chain and a full CASSCF active space of 12 electrons and 12 π orbitals (CAS 12/12) is applied. The reduced model is simplified by excluding the non–π–conjugated β–ionone ring part (see Fig. 5.2b–d) and employing a reduced CASSCF 10/10 active space.

The protein set–up used in this work is the same used by some of the authors in a very recent static investigation of rhodopsin photoisomerization (see ref. 16 for the details). While the protonation state of glutamic acid 181 is still a matter of debate, it was left unprotonated in the current simulations. Owing to its location above the centre of the retinal chromophore, this residue's charge does not affect the photoisomerization path

and the energy of the photoactive charge transfer state S_1 (refs 16, 41). Therefore, this choice should not influence the computed dynamics.

D. Active space selection for dynamical simulations

The π orbital set used for the reduced chromophore is depicted in Supplementary Fig. B.3. To validate the reductions in orbital space and QM region, the static excited state reaction path along C_{11}=C_{12} torsion was computed by constrained geometry optimization and compared to the corresponding reaction path of the full chromophore from ref. 16. A two root state averaged wavefunction was employed in both calculations. Supplementary Fig. B.4 shows the isomerization S_1 energy profiles for the full chromophore (full lines) and the reduced model (dotted lines). Both the excited state energies and the S_1/S_0 energy differences in CAS(12/12) are almost perfectly reproduced by CAS(10/10). From these results we conclude that the simplifications applied are reasonable and allow a calculation of several trajectories at significantly reduced computational cost, still preserving the accuracy found in the unreduced QM–model/active space. This conclusion is further supported by dynamical computations (see below).

E. Molecular dynamics simulations

CAS(10,10)/6–31G*/AMBER QM/MM numerical frequencies have been calculated on the rhodopsin ground state minimum (optimized at the same level). These are used to generate initial conditions for the dynamics by thermally sampling the vibrational modes at 300 K (ref. 42; including zero–point energy corrections: high frequency C–H, N–H and O–H modes are excluded). Note that the temperature distribution is related only to the mobile part, while the protein stays fixed during thermal sampling and molecular dynamics runs. The fixed crystal structure of the protein is considered as a mean representation of the experimental positions of the atoms, although at low (100 K) temperature. This approximation is justified by the extremely short timescale of the rhodopsin primary photochemical event investigated here (~100 fs decay time and 200 fs photoproduct appearance time) that prevents protein thermalization (that is, equilibration). This is further supported by the results of ref. 15, showing that excited state dynamics in rhodopsin are not affected by protein mobility. While this is a well established procedure [14,16], it was also adopted for practical reasons. The number of electrostatic field derivatives that can be calculated in one step by the *ab initio* program is limited. Furthermore, a mobile protein environment may result in a wrong ordering of S_1 and S_2 energy states at the CASSCF level, leading to unrealistic simulations. Supplementary Fig. B.5 shows the distribution of several ensemble parameters for the 38 randomly generated initial conditions. Considering the limited number of sampled points, the partitioning of potential and kinetic energies and torsion angles appears reasonable and suggests that the sample is already statistically meaningful.

Trajectories were started after Franck–Condon excitation to the first excited singlet state using the COBRAMM interface, which couples Molpro–CASSCF and

Amber. The wavefunction was averaged over the first three singlet states throughout the entire calculation. For accurate calculation of state averaged CASSCF gradients, Molpro's CPMCSCF routines were employed [36]. Newton's equations of motion were integrated on the fly using the velocity Verlet algorithm [43] and a time step of 0.5 fs. In order to properly detect possible decay points, the time step was reduced to 0.25 fs when the S_1–S_0 energy difference was below 8 kcal mol^{-1}. When the scalar product of the S_1 and S_0 state coefficients indicated that a surface crossing had been passed, the trajectories were brought to the ground state [44]. The energy gap at the hops was always below 2.2 kcal mol^{-1}. This simplified algorithm forces hops to take place only at the S_1/S_0 intersection seam and, in principle, could lead to an underestimation of the population transfer probability. However, the S_1/S_0 conical intersection is very peaked in rhodopsin [16]. This topological feature is compatible with a decay that substantially occurs only when the intersection seam is reached, justifying the adopted hopping procedure.

The two–panel Supplementary Movie displays the 'averaged' molecular structures corresponding to the trajectories leading respectively to the all–*trans* retinal photoproduct and to the 11–*cis* reactant; owing to the random rotation of methyls, the positions of methyl hydrogens have been fixed relative to their neighbouring carbon. The dihedral angle of the rotating central bond is explicitly displayed, clearly showing that the motion is restricted to the central part of the chromophore.

F. Reference trajectories: further validation of the reduced CAS(10,10) active space

Two reference trajectories, starting without initial kinetic energy (0 K) with a time step of 1 fs, were propagated employing the reduced QM chromophore model with a CAS(10/10) active space and a full CAS(12/12) active space description. Supplementary Fig. B.6 shows the evolution of energies, C115C12 dihedrals and bond lengths. For the most part, the two trajectories are almost identical. Subtle differences appear only after the hop to the ground state, which is delayed by only 1 fs in CAS(12/12). These dynamical results validate the reduced CAS(10/10) active space employed in this work for a systematic dynamical investigation of the retinal photoreaction in rhodopsin, being almost as accurate as the full CAS(12,12) active space.

G. Calibration of ultraviolet-visible absorption and emission data

In order to partially account for the deficiencies in CASSCF calculated spectral data, linear scaling factors were estimated to match the more accurate values obtained at the CASPT2 level of theory [24]. As applied in the dynamics, a CAS(10,10)/6–31G* three root state averaged description of the wavefunction was used for the reduced system to optimize the complete static photoisomerization path from first excited to ground state. State averaged CASSCF gradients were computed using Molpro's CPMCSCF routines. The three root state averaged approach allowed us to estimate the contribution of both S_0–S_1 and S_1–S_2 transitions; the latter may have a non–negligible influence on time–resolved emission/absorption spectra.

Supplementary Fig. B.7a shows the first three singlet state energies along the

aforementioned reaction path calculated with CASSCF (full lines) and with Molcas CASPT2 (dotted lines). To generate these plots, the CASSCF(10/10) optimized reaction path of the reduced model (full lines) has been re–evaluated at the CASPT2 level employing a constant imaginary level shift [45] of 0.2 and according to a full chromophore approach: the QM region and active space have been enlarged on top of the reduced chromophore structures to embrace the whole chromophore and p orbital space, respectively. Remarkably, the vertical $S_0 \rightarrow S_1$ CASPT2(12,12) computed energy is 58.9 kcal mol^{-1}, in fair agreement with the recorded absorption (57.6 kcal mol^{-1}). As expected, S_1 is less steep at the CASPT2 level, and the S_2 energy is significantly reduced when considering dynamic electron correlation. Energy differences are depicted in Supplementary Fig. B.7b. Scaling factors for the stimulated emission signal were obtained by averaging the energy difference quotients from the S_1 backbone relaxed chromophore structure (Min–S_1) to 60° of C_{10}–C_{11}=C_{12}–C_{13} torsion. It is worth noting that, in order to increase the accuracy of the scaling factors employed in spectra simulations, both the Franck–Condon structure and the region in close vicinity to the conical intersection (that is, 70°–110° twisted points that all have a rather small S_1/S_0 energy gap) have not been taken into account in the fitting, as they do not enter the probe wavelength window (610–720 nm and 820–1,020 nm) of the experiments (see Fig. 5.1). Scaling factors for the photoinduced absorption signal were estimated by an analogous procedure, using the optimized ground state path from 120° towards the photoproduct. The values are reported in Supplementary Table B1.

In addition, the scaling factor for the stimulated emission process has also been determined from the reference 0 K CAS(10/10) trajectory described in the previous section, by employing an analogous procedure. Those values are listed in Supplementary Table B2 and show that the dynamical scaling factor (0.793) is very similar to the static one (0.791). This confirms that the scaling factors obtained here are applicable to retinal photoisomerization trajectories.

Supplementary Fig. B.7, comparing CASSCF versus CASPT2 energy profiles, also illustrates another important point: the CASSCF surface is not much steeper than the correlated one. Indeed, CASSCF overestimates excited state energies all along the photoisomerization path including the starting (Franck–Condon) and ending (conical intersection) points, leading to a moderate change in the gradient. More specifically, both profiles are barrierless and only the very initial part (Franck–Condon→Min–S_1) of the CASSCF relaxation path is slightly steeper. This part refers mainly to C–C bond order inversion, with no torsion involved. Afterwards, when C_{11}=C_{12} rotation becomes active, the two surfaces run almost parallel to each other. The same behaviour has already been recognized in other retinal protonated Schiff base models (see Figure 3 in ref. 10).

Owing to the overestimation of the surface steepness, a somewhat faster process is expected in our simulations and, indeed, our initial relaxation out of the Franck–Condon region is slightly faster than observed: see the simulated lines in Fig. 5.1c that are steeper than the experimental ones in Fig. 5.1a. However, the C_{11}=C_{12} torsional mode is driven by a correct gradient and force field, and the timing error is comparable to the 20–fs time resolution of the experiments. For this reason, differently from ref. 14, we preferred not to apply any scaling factor to the simulated timescale, which already agrees reasonably well with the experiments. The scaling factor was instead applied to the

transition energies to gain experimentally accurate values.

H. From the trajectories to the transient spectra

For each instant of time, the transient spectrum was calculated as a superposition of $S_1 \rightarrow S_0$ stimulated emission and $S_1 \rightarrow S_2$ photoinduced absorption before, and $S_0 \rightarrow S_1$ photoinduced absorption after, the hop to the ground state. Each of these three signals was represented by a Gaussian functions centred at the corresponding transition energy averaged over all the trajectories with half–width equal to the standard deviation of the collected data and height equal to the mean oscillator strength. To account for the finite pulse widths used in the experiments, we convolved the calculated transient signals with a 20–fs FWHM Gaussian function.

5.9 References

[1] T. Yoshizawa and G. Wald, *Nature* **197,** 1279 (1963).

[2] J. E. Kim, M. J. Tauber and R. A. Mathies, *Biochemistry* **40,** 13774 (2001).

[3] R. W. Schoenlein, L. A. Peteanu, R. A. Mathies and C. V. Shank, *Science* **254,** 412 (1991).

[4] G. Haran, E. A. Morlino, J. Matthes, R. H. Callender and R. M. Hochstrasser, *J. Phys. Chem. A* **103,** 2202 (1999).

[5] H. Chosrowjan, N. Mataga, Y. Shibata, S. Tachibanaki, H. Kandori, Y. Shichida, T. Okada and T. Kouyama, *J. Am. Chem. Soc.* **120,** 9706 (1998).

[6] H. Kandori, Y. Furutani, S. Nishimura, Y. Shichida, H. Chosrowjan, Y. Shibata and N. Mataga, *Chem. Phys. Lett.* **334,** 271 (2001).

[7] G. G Kochendoerfer and R. A. Mathies, *J. Phys. Chem.* **100,** 14526 (1996).

[8] G. A. Schick, T. M. Cooper, R. A. Holloway, L. P. Murray and R. R. Birge, *Biochemistry* **26,** 2556 (1987).

[9] R. A. Mathies and J. Lugtenburg, in *Handbook of Biological Physics: Molecular Mechanisms in Visual Transduction;* D. G. Stavenga, W. J. DeGrip and E. N. Pugh, Eds. (Elsevier Science, 2000), Vol. 3, p. 55.

[10] M. Garavelli, P. Celani, F. Bernardi, M. A. Robb and M. Olivucci, *J. Am. Chem. Soc.* **119,** 6891 (1997).

[11] R. González–Luque, M. Garavelli, F. Bernardi, M. Merchán, M. A. Robb and M. Olivucci, *Proc. Natl Acad. Sci. U.S.A.* **97,** 9379 (2000).

[12] M. Klessinger and J. Michl, *Excited states and photochemistry of organic molecules* (VCH Publishers, 1994).

[13] B. G. Levine and T. M. Martinez, *Annu. Rev. Phys. Chem.* **58,** 613 (2007).

[14] L. M. Frutos, T. Andruniow, F. Santoro, N. Ferre and M. Olivucci, *Proc. Natl. Acad. Sci. U.S.A.* **104,** 7764 (2007).

[15] S. Hayashi, E. Tajkhorshid and K. Schulten, *Biophys. J.* **96,** 403 (2009).

[16] G. Tomasello, G. Olaso-González, P. Altoè, M. Stenta, L. Serrano-Andrés, M. Merchán, G. Orlandi, A. Bottoni and M. Garavelli, *J. Am. Chem. Soc.* **131,** 5172 (2009).

[17] C. Manzoni, D. Polli and G. Cerullo, *Rev. Sci. Instrum.* **77,** 023103 (2006).

[18] O. Weingart, *J. Am. Chem. Soc.* **129,** 10618 (2007).

[19] S. Hayashi, E. Tajkhorshid and K. Schulten, *Biophys. J.* **85,** 1440 (2003).

[20] G. Groenhof, M. Bouxin-Cademartory, B. Hess, S. P. de Visser, H. J. C.

Berendsen, M. Olivucci, A. E. Mark and M. A. Robb, *J. Am. Chem. Soc.* **126,** 4228 (2004).

[21] G. Groenhof, L. V. Schäfer, M. Boggio-Pasqua, M. Goette, H. Grubmüller and M. A. Robb, *J. Am. Chem. Soc.* **129,** 6812 (2007).

[22] H. R. Hudock, B. G. Levine, A. L. Thompson, H. Satzger, D. Townsend, N. Gador, S. Ullrich, A. Stolow and T. J. Martinez, *J. Phys. Chem. A* **111,** 8500 (2007).

[23] H. R. Hudock and T. J. Martinez, *ChemPhysChem* **9,** 2486 (2008).

[24] K. Andersson, P. –A. Malmqvist and B. O. Roos, *J. Chem. Phys.* **96,** 1218 (1992).

[25] H. Tao, B. G. Levine and T. J. Martinez, *J. Phys. Chem. A* **113,** 13656 (2009).

[26] P. Kukura, D. W. McCamant, S. Yoon, D. B. Wandschneider and R. A. Mathies, *Science* **310,** 1006 (2005).

[27] Q. Wang, R. W. Schoenlein, L. A. Peteanu, R. A. Mathies and C. V. Shank, *Science* **266,** 422 (1994).

[28] A. Warshel, *Nature* **260,** 679 (1976).

[29] A. Warshel and N. Barboy, *J. Am. Chem. Soc.* **104,**1469 (1982).

[30] T. Okada, M. Sugihara, A. –N. Bondar, M. Elstner, P. Entel and V. Buss*, J. Mol. Biol.* **342,** 571 (2004).

[31] W. J. De Grip, F. J. M. Daemen and S. L. Bonting, *Methods Enzymol.* **67,** 301 (1980).

[32] D. Polli, L. Lüer and G. Cerullo, *Rev. Sci. Instrum.* **78,** 103108 (2007).

[33] H. Lin and D. G. Truhlar, *Theor. Chem. Acc.* **117,** 185 (2007).

[34] P. Altoè, M. Stenta, A. Bottoni and M. Garavelli, *Theor. Chem. Acc*. **118,** 219 (2007).

[35] U. C. Singh and P. A. Kollman, *J. Comput. Chem.* **7,** 718 (1986).

[36] H. –J. Werner et al. MOLPRO, version 2008.1, a package of *ab initio* programs (Cardiff University, UK, 2008).

[37] G. Karlström, R. Lindh, P. –A. Malmqvist, B. O. Roos, U. Ryde, V. Veryazov, P. –O. Widmark, M. Cossi, B. Schimmelpfennig, P. Neogrady and L. Seiojo, *Comput. Mater. Sci.* **28,** 222 (2003).

[38] D. A. Case, T. E. Cheatham, T. Darden, H. Gohlke, R. Luo, K. M. Merz, A. Onufriev, C. Simmerling, B. Wang and R. J. Woods, *J. Comput. Chem.* **26,** 1668 (2005).

[39] M. Stenta, M. Calvaresi, P. Altoè, D. Spinelli, M. Garavelli and A. Bottoni, *J. Phys. Chem. B* **112,** 1057 (2008).

[40] B. O. Roos, in *Advances in Chemical Physics: Ab Initio Methods in Quantum Chemistry;* K. P. Lawley, Ed. (Wiley & Sons, 1987) Part 2, Vol. 69, p. 399.

[41] A. Cembran, F. Bernardi, M. Olivucci and M. Garavelli, *J. Am. Chem. Soc.* **126,** 16018 (2004).

[42] C. S. Sloane and W. L. Hase, *J. Chem. Phys.* **66,** 1523 (1977).

[43] L. Verlet, *Phys. Rev.* **159,** 98 (1967).

[44] O. Weingart, I. Schapiro and V. Buss, *J. Phys. Chem. B* **111,** 3782 (2007).

[45] N. Försberg and P. –A. Malmqvist, *Chem. Phys. Lett.* **274,** 196 (1997).

Chapter 6
Conclusions and Prospects

6.1 Conclusions

Through the application of resonance Raman (RR) intensity analysis and ultrafast electronic pump-probe spectroscopy, this dissertation has provided a better understanding of the primary photochemical reactions in phytochrome Cph1 and rhodopsin. Although these proteins vary greatly in composition, architecture and biological function, their primary photochemistry is essentially the same. They utilize covalently bound, extended conjugated chromophores that absorb strongly in the visible region of the electromagnetic spectrum, and respond to light absorption through the isomerization of a carbon-carbon double bond. This initial isomerization event is of vital importance to the success of light-energy conversion in phytochrome Cph1 and rhodopsin, and is the focus of this dissertation.

In Chapters 3 and 4, I address the question of structural composition of the P_r and P_{fr} forms of phytochrome Cph1. Using RR intensity analysis, I accurately model the experimental absorption spectra with a unique set of parameters for each isomeric conformer, showing that both P_r and P_{fr} are structurally homogeneous in the ground state. This finding is of fundamental importance in understanding phytochrome photochemistry, and refutes the putative structural heterogeneity claimed by other researchers based on multi-component reaction kinetics and the asymmetry of the electronic absorption spectra [1-6]. I also examine the *Z*/*E* isomerization of the P_r and P_{fr} forms of the bilin chromophore in phytochrome Cph1, which takes place in ~1-3 ps with 15% efficiency [1,7-10]. This is a relatively slow and inefficient process – facts inconsistent with the low fluorescence quantum yield ($\phi_f < 10^{-3}$–10^{-4}) [11] that suggests ultrafast excited-state dynamics. I investigate this discrepancy and find that loss of symmetry in the distorted chromophore structure results in highly displaced torsional and hydrogen out-of-plane (HOOP) modes that mediate rapid motion out of the Franck-Condon (FC) region. Torsional FC analysis predicts a <200 fs *Z*/*E* isomerization for both

the forward and back reactions, but steric interaction between the chromophore and protein during the isomerization process creates a barrier on the S_1 potential energy surface, resulting in the return of 85% of excited molecules to the ground state before crossing from the excited-state to the photoproduct can occur [7] (see Figure 6.1). Even in the case of P_{fr}, which is primed for isomerization by a ~20° pre-twist along the torsional reaction coordinate, the reaction cannot proceed as predicted due to interference from the surrounding protein environment, which impacts the isomerization dynamics and reduces the net quantum yield.

In the case of rhodopsin, the barrier-free excited-state surface allows FC dynamics to carry the retinal molecule along the torsional and HOOP coordinates straight to the conical intersection, which mediates efficient transfer from the excited to the ground electronic state in 200 fs with a quantum yield of 0.65 [12,13]. The ultrafast FC dynamics paired with a barrierless excited-state surface result in a reaction quantum efficiency that is truly remarkable. In collaboration with researchers at Politecnico di Milano, Università di Bologna, Universität Duisburg-Essen, Max Planck Institute and The University of Oxford, we investigate the 11-*cis* → all-*trans* isomerization using ultrafast pump-probe spectroscopy with sub-20-fs time resolution and a spectral coverage from the visible to the near-infrared. By tracking the coherent wavepacket motion from the initial photoexcited state to the photoproduct, we observe a pattern consistent with the presence of a conical intersection. During the first ~80 fs, we observe the loss of reactant emission and a decrease in the energy gap as the ground- and excited-state potential energy surfaces approach each other. The reaction then passes through the conical intersection as the surfaces meet, and once the photoproduct forms we see the rise of photoproduct absorption and an increase in the probed energy gap. The results presented in Chapter 5 provide the most compelling experimental evidence to date of the involvement of a conical intersection in the unique reactivity of rhodopsin.

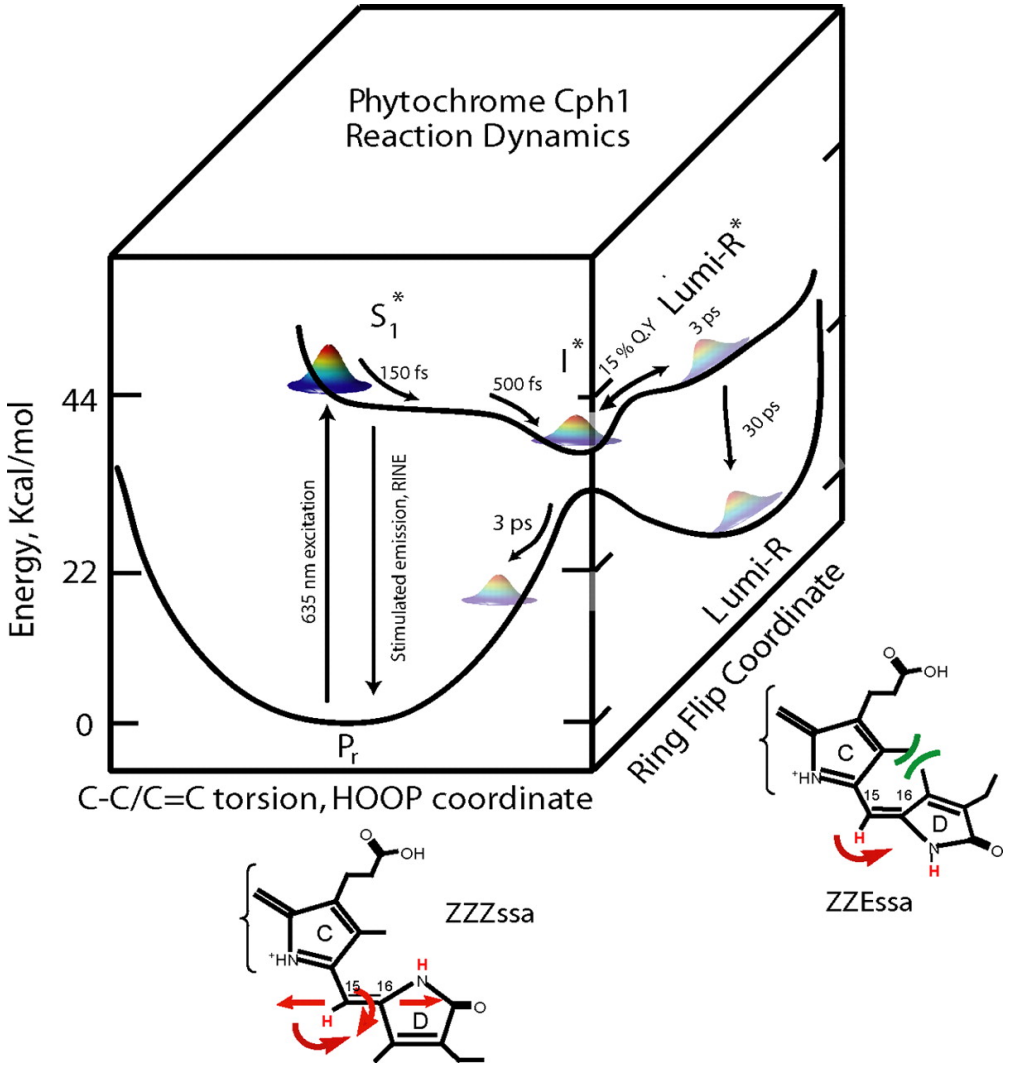

Figure 6.1. Schematic potential energy surfaces involved in the Cph1 P_r-to-P_{fr} photoreaction. The system is launched on the excited-state S_1, which has a steep initial slope in the FC region that rapidly drives the system to the excited-state intermediate I*. From I*, steric interaction between the chromophore and protein causes 85% of the population to return back to the reactant ground state while the remainder overcomes the barrier to form the Lumi-R* excited-state intermediate. This excited state decays in 30 ps to form the Lumi-R ground state. The chemical structures of P_r and Lumi-R schematically show the modes involved during the isomerization reaction (Figure from Dasgupta et al. [7]).

6.2 Prospects

The studies on phytochrome Cph1 presented in this dissertation reveal important information regarding its photocycle, yet several questions remain. Why and how are the photochemical mechanisms of the $P_r \rightarrow P_{fr}$ and $P_{fr} \rightarrow P_r$ reactions different? The forward reaction has been investigated extensively, revealing the I* and Lumi-R* intermediates leading to the formation of the first ground-state photoproduct Lumi-R [7,8,14]. Also, it has been shown that the isomerization occurs on the excited state in 3 ps [7]. In contrast, very little is known about the $P_{fr} \rightarrow P_r$ reaction. While several kinetic components have been observed, including the ~700 fs isomerization time, the intermediate and photoproduct states remain poorly characterized [1,10]. The back reaction is more difficult to study because, at photoequilibrium, phytochrome exists as a 70/30 P_{fr}/P_r mixture [9]. Therefore, a high-resolution structural technique is necessary to distinguish between P_r and P_{fr} spectral signatures. Femtosecond stimulated Raman spectroscopy (FSRS) is the obvious choice for investigating the back reaction as it allows the observation of structural dynamics with both high spectral and temporal resolution. FSRS would allow the investigation of the primary process of Cph1 $P_{fr} \rightarrow P_r$ photoconversion from 50-fs to 100-ps, revealing the vibrational structure of the intermediate states and the location of the isomerization, as well as the partitioning of the excited-state into successful and unsuccessful internal conversion pathways.

I have shown in this dissertation that the ground state populations of the P_r and P_{fr} forms of phytochrome Cph1 are homogeneous. It would be interesting to examine the structural conformation of other phytochromes, such as the PΦB-binding phyA. Mroginski et al. have recently presented the RR spectrum of the P_{fr} form of phyA(PΦB), which displays a prominent band at 1599 cm^{-1} originating from the $C_{15}=C_{16}$ stretch and a weaker band at 1618 cm^{-1} that is assigned to the $C_4=C_5$ stretch [15]. The 1618 cm^{-1} band exhibits a weak but clearly detectable shoulder at 1633 cm^{-1} for which the assignment is not clear. In addition, there is a prominent doublet at ~800-815 cm^{-1} in the HOOP region. Taken together, these data have been interpreted as evidence of two P_{fr} conformers that differ with respect to the structure of the A–B methine bridge. It is suggested that this structural heterogeneity may be functional for the thermal stability of P_{fr}, and is present only in those phytochromes in which the P_{fr} state undergoes a thermal decay to P_r (such as phyA(PΦB)). Because the P_{fr} form of phytochrome Cph1 does not undergo dark reversion to P_r, my work cannot be used to address this particular case. It would be very interesting to examine the structural composition of the P_{fr} form of phytochromes that undergo $P_{fr} \rightarrow P_r$ dark reversion to determine whether the photoinduced and thermally induced reaction pathways originate from structurally distinct P_{fr} conformers. RR intensity analysis of the P_{fr} form of phyA(PΦB) would address the question of whether conformational homogeneity is unique to phytochrome Cph1, or if it is ubiquitous to the phytochrome class of photoreceptors. The results could give great insight into the process of light-energy conversion and the triggering of biological function in phytochromes.

Another point of interest arising from this dissertation is the role of pretwisting in the ultrafast isomerization of extended conjugated chromophores. The chromophore binding domain of rhodopsin facilitates the ultrafast isomerization by constraining the 11-*cis* retinal protonated Schiff base (PSB) such that it is directed along the desired reaction

pathway. An important consequence of this constraint is the torsional distortion imposed on the chromophore, which primes the chromophore for isomerization. Taken out of the protein environment and put into solution, 11-*cis* retinal PSB has a much lower isomerization time (e.g., 10 ps in methanol) [16] and a much lower efficiency (e.g., quantum yield ~0.2) [17]. This is likely due to the loss of distortion, which is indicated by the significant decrease in the Raman HOOP intensity relative to that of rhodopsin (Figure 6.2). It is possible to confine the molecule in a distorted configuration by embedding the reactive double bond in an eight-member ring, forming the retinal analog PSB11.8 (Figure 6.3). Previous studies investigating the dynamics of rhodopsin incorporating PSB11.8 show that it forms two photoproducts (photorhodopsin-like and bathorhodopsin-like) and has a 60 fs excited-state (S_1) lifetime [19], making its photochemistry remarkably similar to that of native rhodopsin. It would be hugely interesting to study the photochemistry of PSB11.8 in solution to determine whether a distorted structure is sufficient to facilitate ultrafast isomerization, or if the protein's chromophore binding pocket is necessary to achieve this unique photochemistry. This can be achieved using RR intensity analysis and FSRS. Using RR intensity analysis the degree of distortion and initial excited-state photochemical dynamics can be determined, and FSRS can be used to probe the structural changes associated with PSB11.8 isomerization.

The RR intensity analysis work presented in this dissertation was accomplished using the RRModel.f program written by Anne Myers Kelley of UC Merced. The program is written in Fortran77 and requires an input file with hundreds of parameters that must be adjusted manually before each calculation. This process is extremely time consuming and requires the user to have an in depth understanding of the program and how adjustment of the parameters will affect the calculated outcome. Automation of this process would be hugely beneficial, not only because it would decrease enormously the time spent running the calculations (under an hour versus days or weeks) but also because it would make RR intensity analysis more routine and thus available to non-experts as a tool in their investigation of photochemical processes. An automated method has been developed previously [20], but I have not had success in using it to run RRModel calculations. The method utilizes the RRModel.f code combined with an optimization routine from MATLAB that iteratively adjusts the parameters of the molecular model to minimize the least-squared error between calculated and experimental spectra. Further development of the automated routine is needed so that it can be run routinely and without difficulties associated with debugging, compiling and running the program.

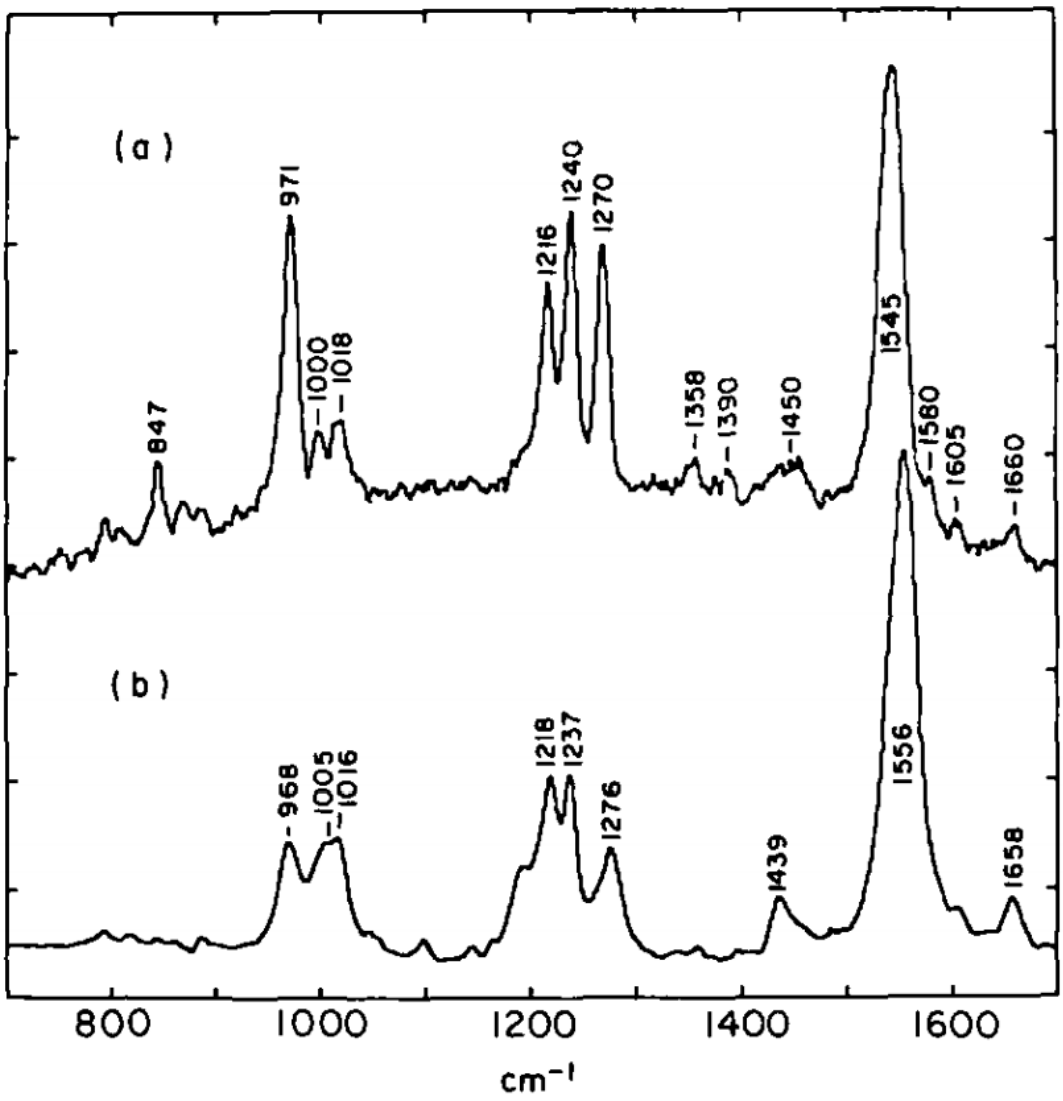

Figure 6.2. Resonance Raman spectra of a) rhodopsin in 60 mM sodium phosphate buffer and b) 11-*cis* retinal protonated Schiff base in ethanol obtained using 25 mW at 600 nm. The HOOP mode is at 971 cm^{-1} in rhodopsin and 968 cm^{-1} in 11-*cis* retinal. Spectra taken from Mathies et al. [18].

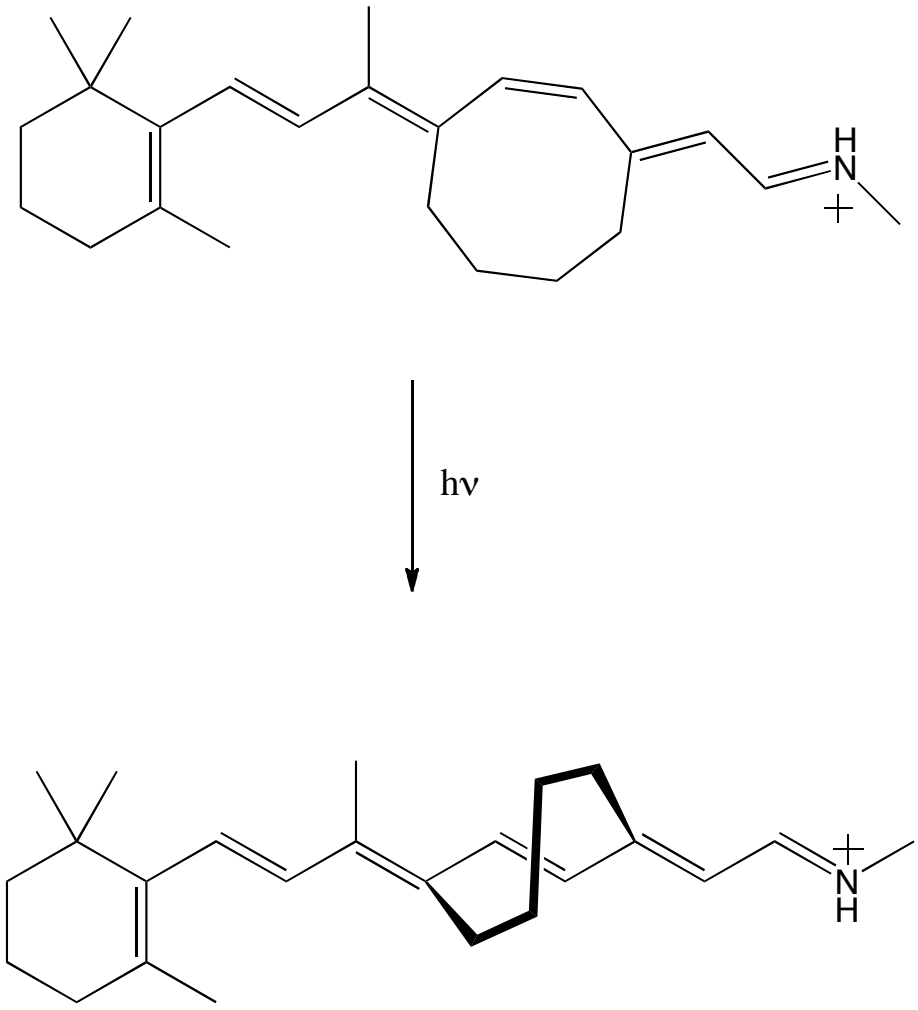

Figure 6.3. 11-*cis* → all-*trans* isomerization of the PSB11.8 retinal analog.

6.3 References

[1] M. Bischoff, G. Hermann, S. Rentsch and D. Strehlow, *Biochemistry* **40,** 181 (2001).

[2] D. L. Correll, J. L. Edwards and W. Shropshire, *Photochem. Photobiol.* **8,** 465 (1968).

[3] J. B. Nieder, M. Brecht and R. Bittl, *J. Am. Chem. Soc.* **131,** 69 (2009).

[4] P. Schmidt, T. Gertsch, A. Remberg, W. Gärtner, S. E. Braslavsky and K. Schaffner, *Photochem. Photobiol.* **68,** 754 (1998).

[5] D. von Stetten, M. Günther, P. Scheerer, D. H. Murgida, M. A. Mroginski, N. Krauβ, T. Lamparter, J. Zhang, D. M. Anstrom, R. D. Vierstra, K. T. Forest, and P. Hildebrandt, *Angew. Chem. Int. Ed.* **47,** 4753 (2008).

[6] A. R. Holzwarth, E. Venuti, S. E. Braslavsky and K. Schaffner, *Biochim. Biophys. Acta* **1140,** 59 (1992).

[7] J. Dasgupta, R. R. Frontiera, K. C. Taylor, J. C. Lagarias and R. A. Mathies, *Proc. Natl. Acad. Sci. U.S.A.* **106,** 1784 (2009).

[8] J. J. van Thor, K. L. Ronayne and M. Towrie, *J. Am. Chem. Soc.* **129,** 126 (2007).

[9] T. Lamparter, F. Mittmann, W. Gärtner, T. Börner, E. Hartmann and J. Hughes, *Proc. Natl. Acad. Sci. U.S.A.* **94,** 11792 (1997).

[10] M. Bischoff, G. Hermann, S. Rentsch and D. Strehlow, *J. Phys. Chem. A* **102,** 4399 (1998).

[11] V. A. Sineshchekov, *Biochim. Biophys. Acta* **1228,** 125 (1995).

[12] R. W. Schoenlein, L. A. Peteanu, R. A. Mathies and C. V. Shank, *Science* **254,** 412 (1991).

[13] J. E. Kim, M. J. Tauber and R. A. Mathies, *Biochemistry* **40,** 13774 (2001).

[14] K. Heyne, J. Herbst, D. Stehlik, B. Esteban, T. Lamparter, J. Hughes and R. Diller, *Biophys. J.* **82,** 1004 (2002).

[15] M. A. Mroginski, D. von Stetten, S. Kaminski, F. V. Escobar, N. Michael, G. Daminelli-Widany and P. Hildebrandt, *J. Mol. Struct.* **993,** 15 (2011).

[16] H. Kandori, Y. Katsuta, M. Ito and H. Sasabe, *J. Am. Chem. Soc.* **117,** 2669 (1995).

[17] R. Becker and K. Freedman, *J. Am. Chem. Soc.* **107,** 1477 (1985).

[18] R. Mathies, T. B. Freedman and L. Stryer, *J. Mol. Biol.* **109,** 367 (1977).

[19] L. De Vico, M. Garavelli, F. Bernardi and M. Olivucci, *J. Am. Chem. Soc.* **127,** 2433 (2005).

[20] E. Shorr and A. M. Kelley, *Phys. Chem. Chem. Phys.* **9,** 4785 (2007).

Appendix A

Supporting Information for "Homogeneity of Phytochrome Cph1 Vibronic Absorption Revealed by Resonance Raman Intensity Analysis"

Reprinted with permission from the manuscript by Katelyn M. Spillane, Jyotishman Dasgupta, J. Clark Lagarias and Richard A. Mathies
Journal of the American Chemical Society **131,** 13946-13948 (2009).

A.1 Experimental Section

The stimulated Raman spectra were obtained using the FSRS setup which has been described previously in detail [1]. Briefly, a home-built mode-locked Ti:sapphire oscillator was amplified by a 1 kHz, 800 μJ regenerative amplifier (BMI Alpha 1000/US). This produced a train of 50 fs pulses centered at 795 nm which was used to generate the two pulses necessary for the experiment. The 4 ps narrow bandwidth Raman pump pulse (790.4 nm, 3 μJ) was generated by a grating based pulse stretcher. The Raman probe pulse (~20 fs, 12 nJ) was produced by using a portion of the fundamental for continuum generation in a 3-mm-thick sapphire plate. The non-collinear beams were focused at the sample point. The Raman pump beam was attenuated with an 830 nm long-pass filter, and Raman spectra were measured using the 816–940 nm portions of the probe beam. The beams were dispersed by the spectrograph (ISA HR320) with a 600 grooves/mm grating and then imaged onto a Pixis:100F charge coupled device (CCD, Princeton Instruments). The CCD consists of a 1340 × 100 imaging array of 20 × 20 μm pixels. The CCD read-out rate is 1 kHz, allowing for single-shot detection. The frequency resolution was ~10 cm^{-1}, as determined from the 802 cm^{-1} cyclohexane peak.

Prior to spectroscopic studies, samples were dialyzed against 1 L buffer (25 mM TES–KOH, pH 8.0, 25 mM KCl, 10% glycerol) and then concentrated to 10.6 OD_{660}/cm. For absolute Raman cross-section calibration, a standard solution of $NaNO_3$ (250 mM) in TES–glycerol buffer was used. Samples were flowed through a homemade 1 × 2 × 40 mm Borofloat-glass flow channel at a rate of ~1 mL min^{-1} and measurements were taken at room temperature. The photo-excited material was converted back to the P_r ground state by irradiation of the 500 μL reservoir by a high-powered LED (720 nm, 5 mW, 30° viewing angle, Roithner Lasertechnik) through an RG695 long-pass filter. Sample integrity was confirmed by UV/Vis spectroscopy both before and after the experiments.

A2. Computational Details

Absolute Raman cross-sections of Cph1 were determined as described previously [2]. Briefly, the integrated peak areas were compared to that of an external standard band (the 1045 cm^{-1} symmetric stretch of NO_3^-, $\partial s_{std}/\partial\Omega = 10.9 \times 10^{-14}$ $Å^2$/molecule/steradian at 514.5 nm excitation) [3]. The differential cross-section at 514.5 nm was extrapolated to 1.78×10^{-15} $Å^2$ at 790.4 nm, assuming that the scattering cross-section is proportional to $\nu_S^3\nu_L$, where ν_S and ν_L are the frequencies of scattered and laser light, respectively. The differential cross-section of NO_3^- was then used to calculate the differential cross-section of the 1052 cm^{-1} C–OH stretch band of glycerol (in TES buffer) using Equation A.1:

$$\left(\frac{\partial\sigma}{\partial\Omega}\right)_{glyc} = \frac{(\nu_S)^3_{glyc}}{(\nu_S)^3_{std}} \frac{A_{glyc}}{A_{std}} \frac{c_{std}}{c_{glyc}} \left(\frac{\partial\sigma}{\partial\Omega}\right)_{std} \quad \text{(A.1)}$$

where $(\nu_S)_{glyc}$ and $(\nu_S)_{std}$ are the scattering frequencies, A_{glyc} and A_{std} are the integrated peak areas, and c_{glyc} and c_{std} are the concentrations of glycerol and NO_3^-, respectively.

By the same method, the differential cross-sections of Cph1 were calculated using the 1052 cm^{-1} glycerol mode as an internal standard. The absolute Raman cross-sections were then determined from Equation A.2:

$$\sigma_{Cph1} = \frac{8\pi}{3} \frac{(1+2\rho)}{(1+\rho)} \left(\frac{\partial\sigma}{\partial\Omega}\right)_{Cph1} \quad \text{(A.2)}$$

where the depolarization ratios, ρ, for all bands of Cph1 were measured and found to be ~1/3. Glycerol was used in place of nitrate as the internal standard because inclusion of 250 mM NO_3^- would denature the protein. As a result, Raman spectra of solutions of NO_3^- in TES–glycerol buffer, and Cph1 in TES–glycerol buffer, were measured separately.

Raman excitation profiles (REPs) were calculated using the time-dependent wavepacket formalism of resonance Raman scattering [4]. The absorption cross-sections,

σ_A, were determined by the Fourier transform of $\langle i|i(t)\rangle$, where $|i\rangle$ is the initial vibrational eigenstate on the ground electronic surface and $|i(t)\rangle$ is the vibrational wavefunction of the initial state propagating on the excited electronic surface (Equation A.3). The Raman cross-sections, σ_R, were determined by the square of the half-Fourier transform of $\langle f|i(t)\rangle$, where $|f\rangle$ is the final vibrational eigenstate on the ground electronic surface (Equation A.4):

$$\sigma_A = \frac{8\pi E_L e^2 M^2}{6\hbar^2 cn\left(\theta\sqrt{2\pi}\right)} \int_0^\infty dE \times \exp\left[\frac{-\left(E-E_0\right)^2}{2\theta^2}\right] \mathrm{Re}\int_0^\infty dt \langle i|i(t)\rangle e^{-\Gamma_G^2 t^2/\hbar^2} e^{i\left(E_L+\varepsilon_i\right)t/\hbar} \qquad \text{(A.3)}$$

$$\sigma_R = \frac{8\pi E_S^3 E_L e^4 M^4}{9\hbar^6 c^4\left(\theta\sqrt{2\pi}\right)} \int_0^\infty dE \times \exp\left[\frac{-\left(E-E_0\right)^2}{2\theta^2}\right] \left|\int_0^\infty dt \langle f|i(t)\rangle e^{-\Gamma_G^2 t^2/\hbar^2} e^{i\left(E_L+\varepsilon_i\right)t/\hbar}\right|^2 \qquad \text{(A.4)}$$

where E_L and E_S refer to the frequencies of the laser and scattered light, M is the electronic transition length, E_0 is the zero-zero energy, ε_i is the vibrational energy of eigenstate *i*, Γ_G is the Gaussian homogeneous broadening and θ is the inhomogeneous broadening.

The time-dependent overlaps, $\langle i|i(t)\rangle$ and $\langle f|i(t)\rangle$, depend on the dimensionless parameter Δ, which is the displacement between the ground and excited electronic state harmonic minima. Raman intensity calculations were performed using the program RRModel.f, which was provided by Anne Myers Kelley from UC Merced, to model the experimental absorption spectra and Raman cross-sections. Relative delta values were initially estimated from the intensities of the observed vibrational bands assuming $I \propto \omega^2\Delta^2$ [5]. The overall scaling of Δ, homogeneous broadening Γ_G, inhomogeneous broadening θ, zero-zero energy E_0, and electronic transition length M were then adjusted to provide the best fits.

Absorption Franck-Condon factors were calculated for the 0–0, 0–1, and 0–2 vibronic transitions of modes with $\Delta > 0.2$. The products of these one-dimensional overlaps are given in Equations A.5–A.7 [2]:

$$\langle 0|m\rangle\langle m|0\rangle = \left|\langle m|0\rangle\right|^2 = \left(s^m/m!\right)e^{-s} \qquad \text{(A.5)}$$

$$\langle 1|m\rangle\langle m|0\rangle = \left(\Delta/2^{1/2}\right)\left[\langle 0|m\rangle\langle m|0\rangle - \langle 0|m-1\rangle\langle m-1|0\rangle\right] \qquad \text{(A.6)}$$

$$\langle 2|m\rangle\langle m|0\rangle = 2^{-1/2}\left[s - 2m + \frac{m^2}{s}\langle 0|m\rangle\langle m|0\rangle - \langle 0|m-1\rangle\langle m-1|0\rangle\right] \qquad \text{(A.7)}$$

where m are the vibrational levels of the excited electronic state and $s = \Delta^2/2$. Representative FC overlaps for the 1630 cm^{-1} mode are shown in Figure A.2. The overlaps presented in Figure 3.1 of the main manuscript include a homogeneous broadening of 10 cm^{-1}.

Vibronic absorption spectra of P_r were measured over the temperature range of 281 to 313 K and revealed an isosbestic point at 600 nm (see Figure A.3A). These spectra were simulated using the vibrational frequencies and delta values given in Table A1, and are in excellent agreement with the experimental spectra (see Figure A.3B). For all spectra, the 0–0 transition energy was 14800 cm^{-1} and the inhomogeneous broadening was 90 cm^{-1}. The homogeneous broadening and electronic transition length parameters used in the calculations are given in Table A.1.

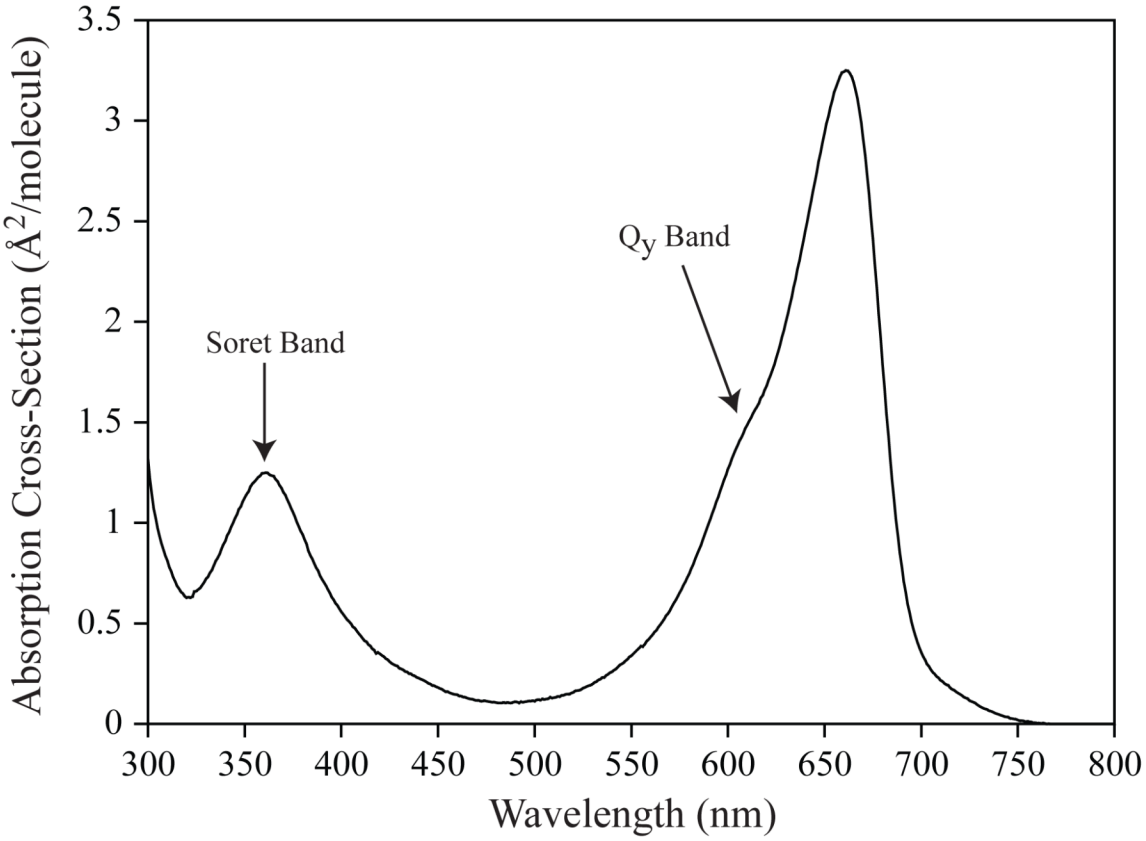

Figure A.1. Experimental absorption spectrum of the P_r form of phytochrome Cph1 at 295 K in glycerol-containing TES buffer. The band used in this analysis is the Q_y band centered at 660 nm.

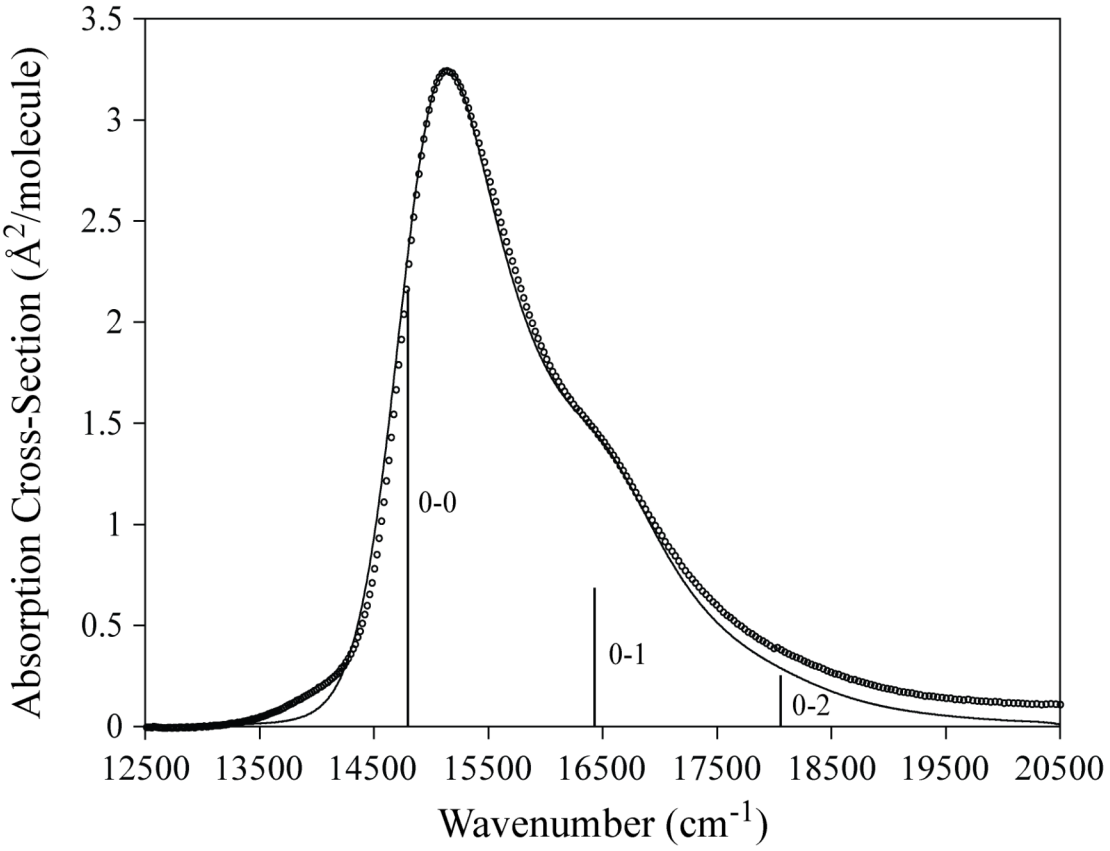

Figure A.2. Experimental and calculated absorption spectra of the P_r form of Cph1 at 295 K. The 0–0, 0–1, and 0–2 FC overlaps of the 1630 cm^{-1} C=C stretch mode are shown.

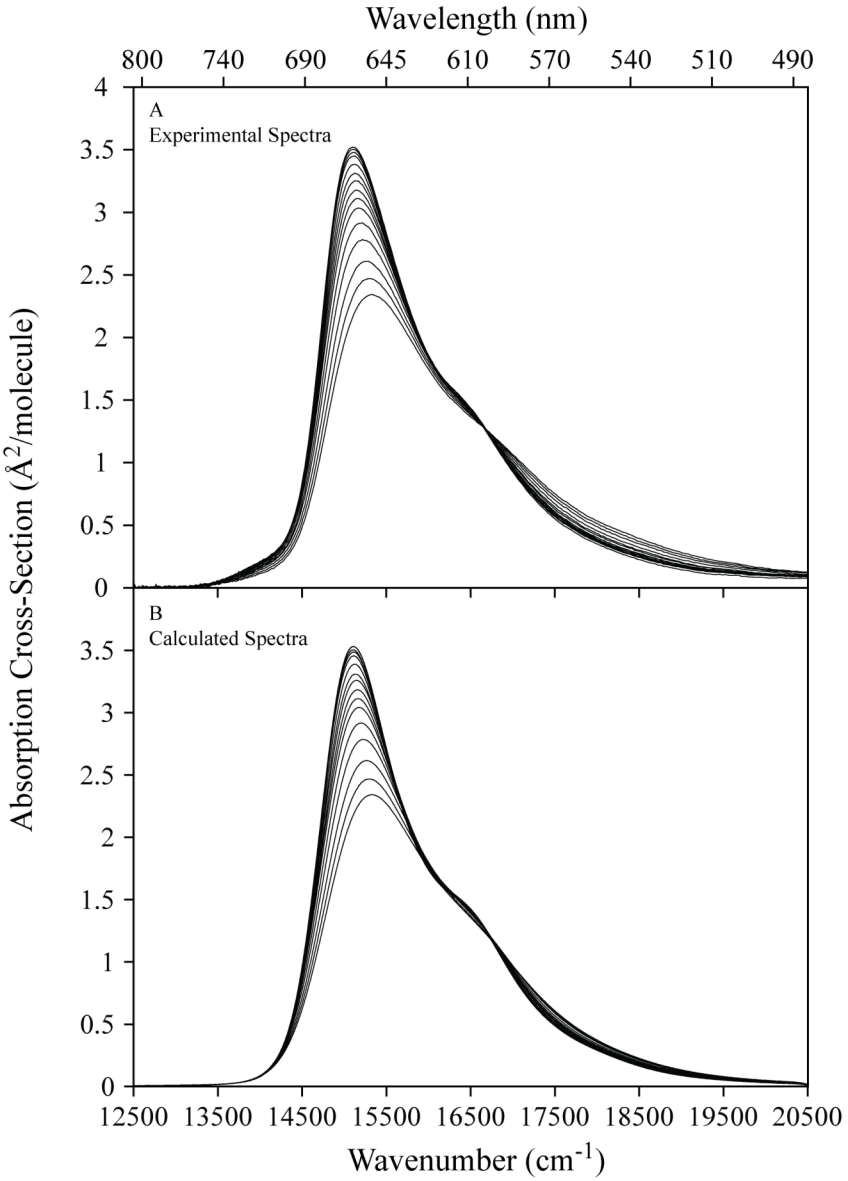

Figure A.3. Comparison of the experimental (A) and calculated (B) absorption spectra of P_r at various temperatures between 281 and 313 K (8°C and 40°C). Note that the absorption cross-section decreases with increasing temperature. The experimental spectra show an isosbestic point at 600 nm, while the calculated spectra show an isosbestic point at 596 nm.

Temp. (K)	Γ_G (cm^{-1})	M (Å)
281	820	2.34
282	820	2.33
283	825	2.35
286	830	2.34
288	835	2.33
291	850	2.33
294	865	2.32
296	880	2.32
298	895	2.31
300	905	2.29
302	920	2.28
304	945	2.26
306	975	2.24
309	1015	2.21
311	1045	2.18
313	1070	2.14

Table A.1. Homogeneous broadening (Γ_G) and electronic transition length (M) parameters over the range of temperatures used to calculate the spectra shown in Figure A3. For all plots, the 0–0 transition energy was 14800 cm^{-1} and the inhomogeneous broadening was 90 cm^{-1}.

A3. References

[1] D. W. McCamant, P. Kukura, S. Yoon and R. A. Mathies, *Rev. Sci. Instrum.* **75,** 4971 (2004).

[2] A. B. Myers and R. A. Mathies, in *Biol. App. of Raman Spectroscopy*; T. G. Spiro, Ed. (John Wiley & Sons, New York, 1987), Vol. 2, p. 1.

[3] J. M. Dudik, C. R. Johnson and S. A. Asher, *J. Chem. Phys.* **82,** 1732 (1985).

[4] S. Y. Lee and E. J. Heller, *J. Chem. Phys.* **71,** 4777 (1979).

[5] J. Tang and A. C. Albrecht, in *Raman Spectroscopy: Theory and Practice*; H. A. Szymanski, Ed. (Plenum Press, New York, 1970), Vol. 2, p. 33.

Appendix B

Supporting Information for "Conical intersection dynamics of the primary photoisomerization event in vision"

Reprinted with permission from the manuscript by Dario Polli, Piero Altoè, Oliver Weingart, Katelyn M. Spillane, Cristian Manzoni, Daniele Brida, Gaia Tomasello, Giorgio Orlandi, Philipp Kukura, Richard A. Mathies, Marco Garavelli and Giulio Cerullo
Nature **467,** 440–443 (2010).

B.1 Analysis of the coherent oscillations

The experimental $\Delta T/T(\lambda,\tau)$ maps for rhodopsin were also recorded for longer time delays with respect to the 200-fs window reported in the main text. We observe the PA signal from the ground state of the all-*trans* photoproduct, peaking around 550 nm. The signal is modulated by a low frequency oscillation. Supplementary Fig. B.8(a) shows the $\Delta T/T(\lambda,\tau)$ map of the oscillatory component of the signal (after subtraction of the slowly varying background). The oscillation, with ~550 fs period, shows a phase jump and an amplitude minimum around 540 nm (see Supplementary Fig. B.8(b)), in proximity of the PA peak of the photoproduct. The probe-wavelength dependence of the amplitude and phase of the oscillation indicates that the wavepacket oscillates in the ground state of the photoproduct, as previously observed by Wang et al. [1] The fact that vibrational coherence, initiated by the pump pulse in the FC region of the reactant, is preserved through the CI and to the photoproduct, is consistent with the extreme speed of excited state wavepacket evolution.

B.2 Trajectory analysis

In this paragraph we analyze in detail the evolution of all 38 trajectories we computed. Supplementary Table B3 reports the hopping time for each individual trajectory, together with the corresponding C_8–C_9=C_{10}–C_{11} and the C_{10}–C_{11}=C_{12}–C_{13} torsion angles at hop. The last column reports the photoproduct state (11-*cis*/all-*trans*) that is reached in the individual runs. Most trajectories reach the S_1/S_0 crossing region within only 80 fs and decay to the ground state at about 110 fs delay on average. At the moment of surface hop, the average torsional angle for the C_{11}=C_{12} bond is $\theta_1 \sim -88°$.

Supplementary Fig. B.9 shows the complete temporal evolution of the two torsional angles. In particular, the green solid curve represents the averaged evolution of the 23 trajectories (61% of the total) which build the all-*trans* isomer and reach a final C_{11}=C_{12} torsional angle of $\theta_1 \sim -140°$, while the red dashed line corresponds to the 15 trajectories (39%) which return to 11-*cis* ($\theta_1 \sim -15°$). A significant change (~ 45°) from its starting value is also observed for the average C_9=C_{10} torsional angle (θ_2) at the hopping point and at the photoproduct side, in agreement with Warshel's proposal of a bicycle pedal photoisomerisation mechanism [2]. Similar findings have been obtained in the recent studies of Weingart [3], Hayashi et al. [4] and Frutos et al. [5]. Weingart's dynamics *in vacuo*, employing a reduced model (lacking the β-ionone ring) for the protein-twisted chromophore, are consistent with the stereoselectivity and ultrafast (< 100 fs) character of the isomerization process. However, they cannot illustrate spectroscopies (the protein is lacking and the chromophore model is smaller), quantum yield (that is overestimated) and cannot account for the protein constrained bicycle-pedal mechanism (the chromophore ends are free to move there). This mechanism, together with the sub-100 fs decay, is accounted for in Hayashi's and Frutos's QM/MM studies, where protein constraints are included. However, the latter employs only one costly CASSCF(12,12) 0 K trajectory that never leaves the S_1 surface and is unable to describe transient spectroscopies (from the reactant to the photoproduct) and the quantum yield. On the other hand, the former uses a mechanical embedding scheme that misses the electrostatic interaction of retinal with the protein pocket and prevents experimentally accurate spectroscopies and quantum yields as well (13 out of 14 trajectories lead to the *trans* photoproduct). Our work includes the latter interaction at the highest (i.e., QM) level, which is mandatory to reproduce quantitatively both effects.

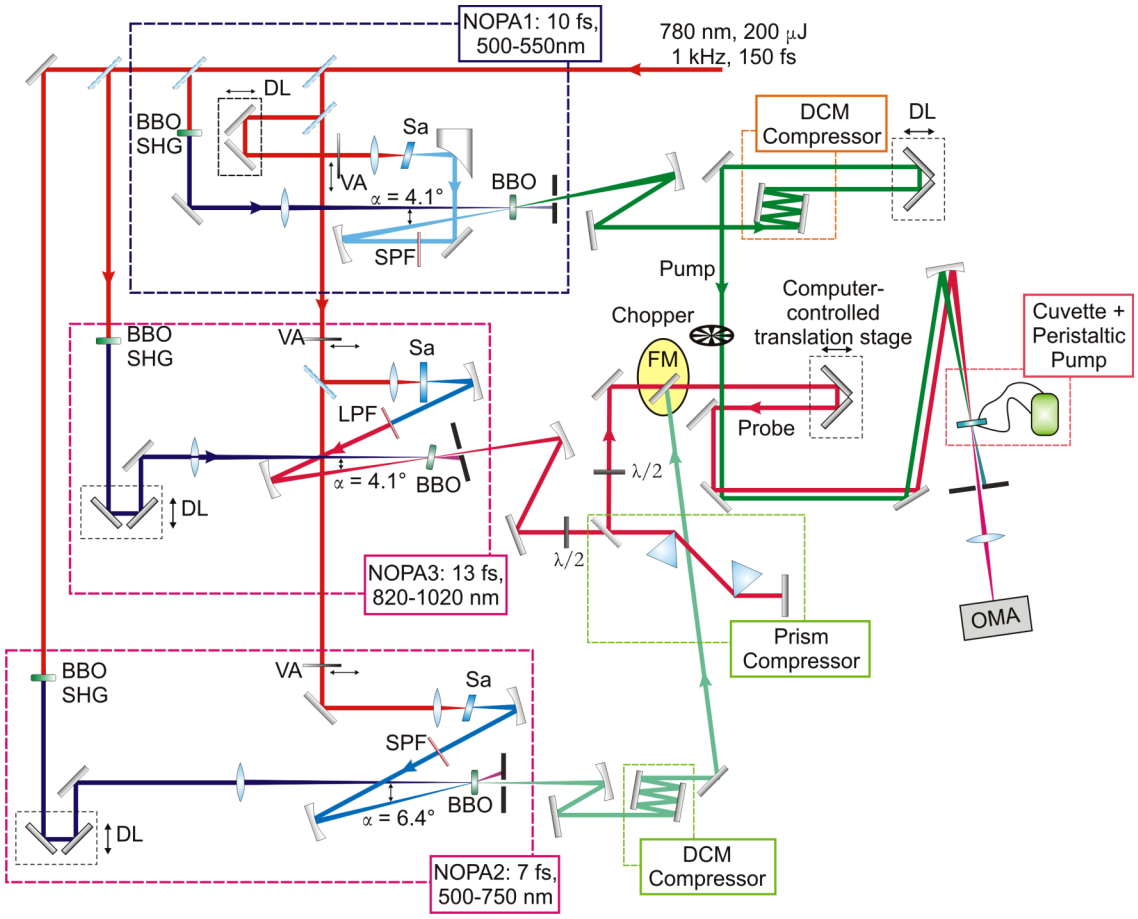

Figure B.1: Experimental set up. NOPA: non-collinear optical parametric amplifier; DL: delay line; Sa: sapphire plate; VA: variable attenuator; DCM: double-chirped mirrors; SHG: second-harmonic generation; SPF: short-pass filter; LPF: long-pass filter; OMA: optical multichannel analyzer; FM: flip mirror.

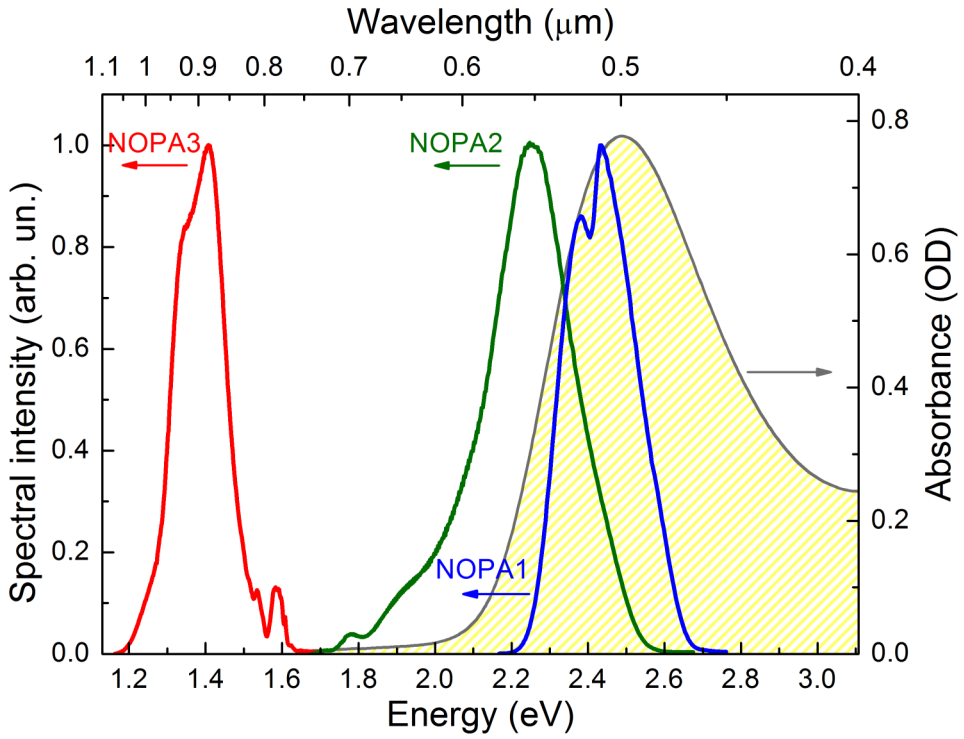

Figure B.2. Pump and probe pulse spectra (solid lines) together with rhodopsin absorption spectrum in a 1-mm cuvette (dashed area).

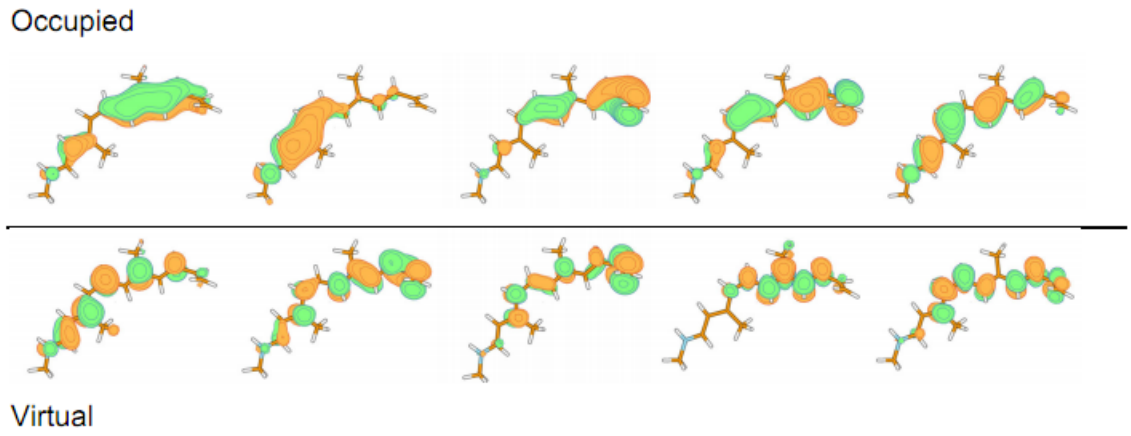

Figure B.3. π-active 10/10 space used in the calculation of QM/MM molecular trajectories of retinal in rhodopsin.

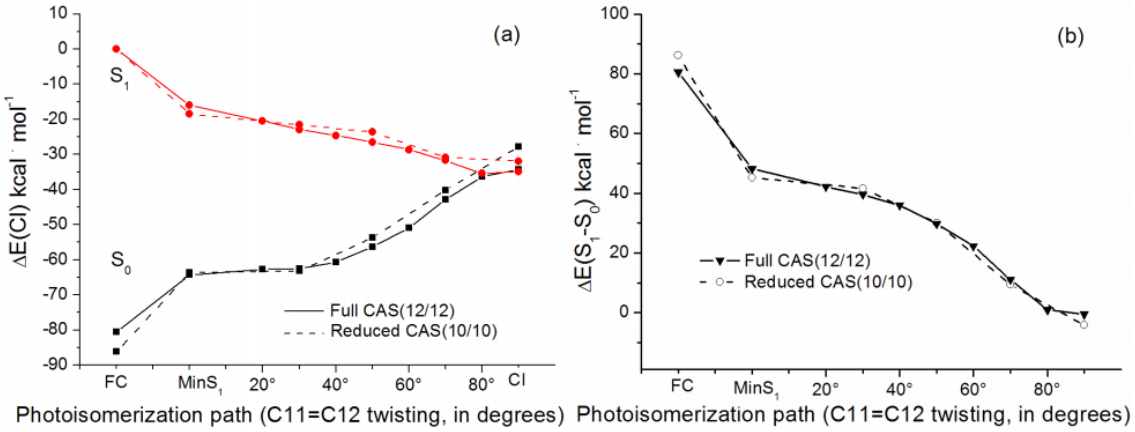

Figure B.4. (a) S_1 and S_0 energies along the excited state reaction path of the full CASSCF(12/12) retinal (full lines) and the reduced CASSCF(10/10) retinal (dotted lines) in rhodopsin. (b) S_1/S_0 energy gap in the same calculations.

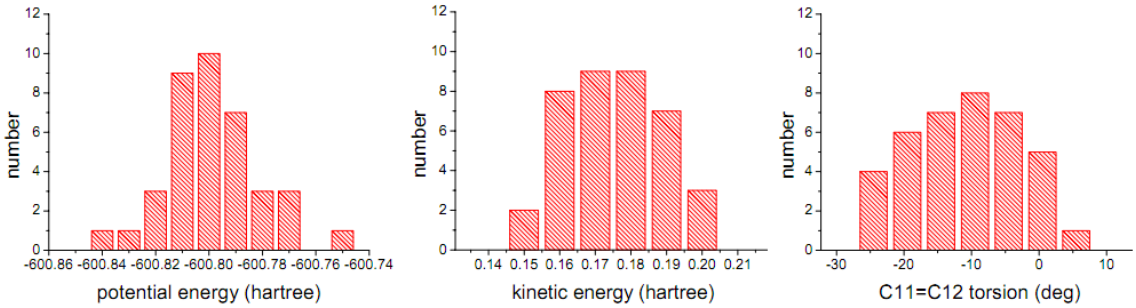

Figure B.5. Potential energies, kinetic energies and C_{11}=C_{12} torsion angles at the start of the simulation.

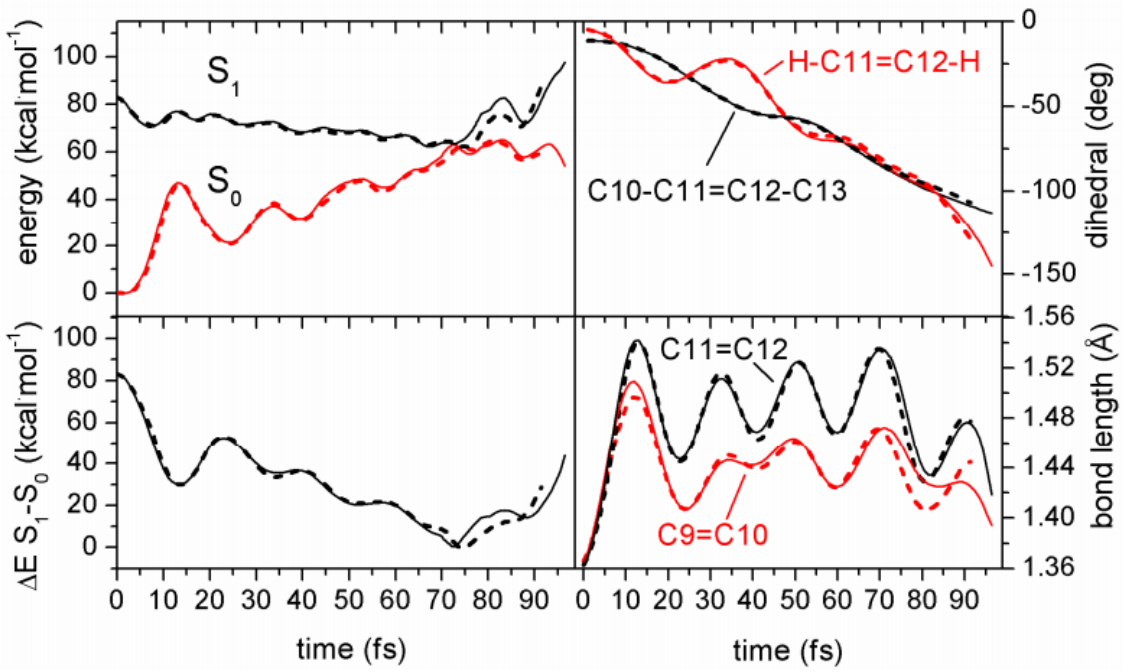

Figure B.6. Evolution of S_1 and S_0 energies, C_{11}=C_{12} torsions, S_1/S_0 energy difference and selected double bond lengths in CAS(10/10) (full lines) and CAS(12/12) reference trajectories (dashed lines).

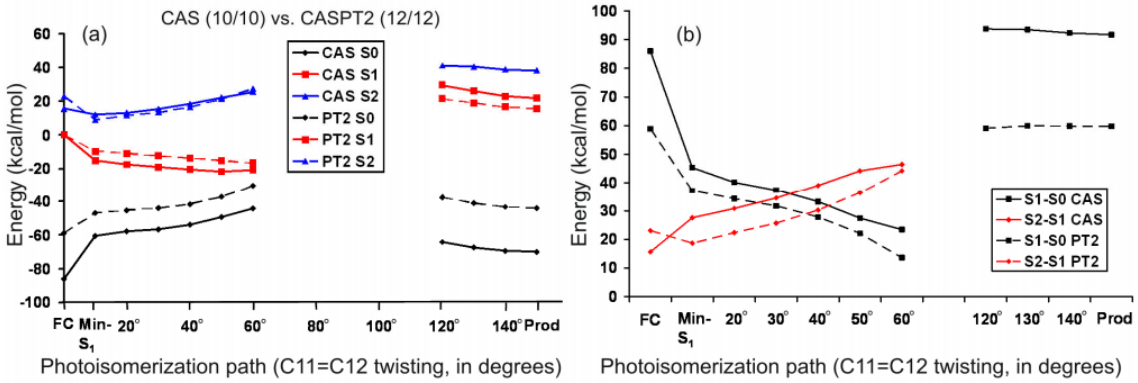

Figure B.7. (a) CASSCF(10/10) (full lines) and CASPT2(12/12) (dotted lines) profiles along the C_{11}=C_{12} photoisomerization path. The FC S_1 energy is used as reference for relative energy values. (b) S_0–S_1 and S_1–S_2 energy differences along the C_{11}=C_{12} photoisomerization path.

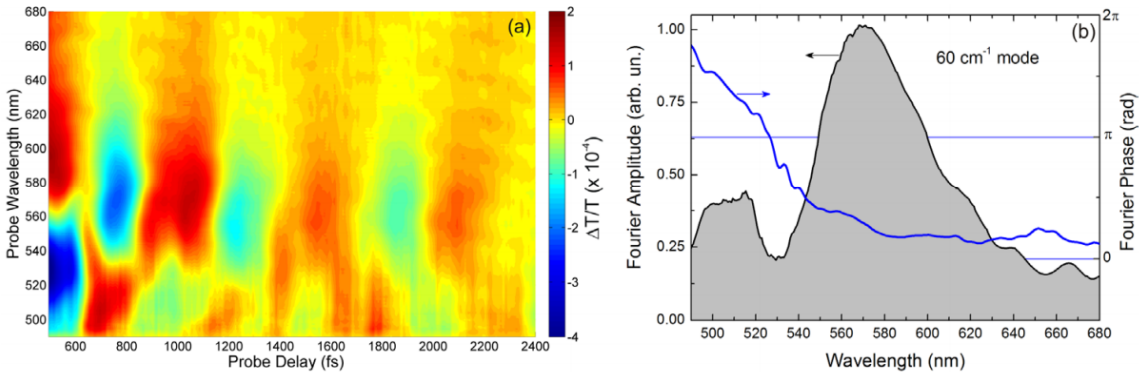

Figure B.8. (a): Map of the oscillatory component of the ΔT/T signal, as a function of probe delay and wavelength; (b) Plot of the Fourier amplitude (filled area) and phase (solid blue line) of the 60 cm^{-1} mode as a function of probing wavelength.

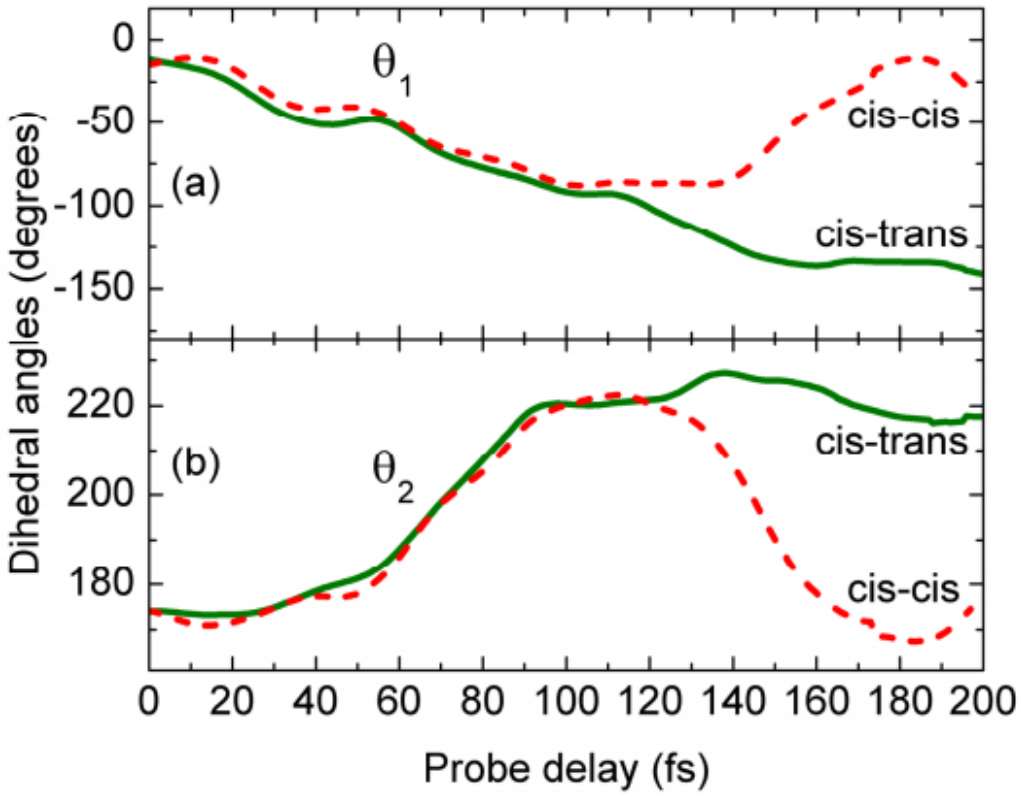

Figure B.9. Evolution of the (a) C_{10}–C_{11}=C_{12}–C_{13} dihedral angle (θ_1) and of the (b) C_8–C_9=C_{10}–C_{11} dihedral angle (θ_2) for both the trajectories leading to the photoproduct (green solid line) and those returning to the parent molecule (red dashed line).

Table B.1: CASSCF to CASPT2 scaling factors for S_0–S_1 and S_1–S_2 transitions from minimum energy path calculations

Static	**FC**	**MinS_1**	**20°**	**30°**	**40°**	**50°**	**60°**	**Aver. (Std. Dev)**
S_1-S_0 Em.	0.685*	0.819	0.853	0.848	0.838	0.805	0.582	***0.791*** (0.104)
S_1-S_2 Tr. Abs.	1.474*	0.677	0.725	0.745	0.773	0.824	0.951	0.782 (0.096)
	Prod	**140°**	**130°**	**120°**				
S_0-S_1 Phot. Abs.	0.651	0.649	0.641	0.631				0.643 (0.009)

*not included in the average and ST. DEV.

Table B.2: CASSCF to CASPT2 scaling factors for S_0–S_1 transitions from reference trajectory.

Dynamic	FC	20fs	40fs	60fs	Aver (Std. Dev)
S_1-S_0 Em.	0.710*	0.908	0.809	0.660	***0.793*** (0.125)

*not included in the average and ST. DEV.

Table B.3: Parameters of individual trajectories at hop and final photoproduct.

Nr	Hopping time [fs]	C10-C11=C12-C13 (θ_1) torsion angle at hop [deg]	C8-C9=C10-C11 (θ_2) torsion angle at hop [deg]	Final product
01	189.25	-83.3	214.5	*Cis*
02	122.25	-91.4	212.6	*Trans*
03	111.75	-78.4	213.6	*Cis*
04	70.50	-82.8	213	*Trans*
05	122.25	-85.7	222.9	*Trans*
06	100.75	-100.0	226.7	*Trans*
07	188.00	-89.8	213.8	*Cis*
08	138.00	-100.8	207.6	*Trans*
09	127.00	-85.3	224.4	*Cis*
10	66.00	-98.6	239.8	*Cis*
11	51.75	-97.2	207.4	*Trans*
12	83.25	-84.9	225.9	*Trans*
13	109.00	-96.9	233.7	*Cis*
14	103.00	-94.7	229.6	*Trans*
15	170.75	-93.9	192.1	*Cis*
16	78.75	-88.2	210.6	*Trans*
17	76.75	-80.5	223.2	*Cis*
18	104.25	-82.3	216.6	*Cis*
19	110.75	-84.6	219.8	*Trans*
20	121.50	-79.7	224.4	*Trans*
21	83.25	-84.9	225.9	*Trans*
22	140.75	-93.6	211	*Cis*
23	146.00	-86.9	215.2	*Cis*
24	134.75	-87.3	188.4	*Trans*
25	107.75	-82.9	224.9	*Trans*
26	95.00	-85.4	217.7	*Cis*
27	121.75	-86.3	216.2	*Trans*
28	102.25	-96.0	222.1	*Trans*
29	80.75	-74.6	199.2	*Trans*
30	97.75	-91.2	206.5	*Trans*
31	87.00	-87.7	208	*Trans*
32	102.00	-89.3	213.4	*Cis*
33	109.00	-82.3	225.4	*Trans*
34	118.25	-70.8	221.7	*Cis*
35	124.25	-92.5	192.9	*Trans*
36	86.50	-73.2	203.9	*Trans*
37	62.50	-93.2	215.4	*Trans*
38	149.75	-99.2	207.1	*Cis*

B.3 References

[1] Q. Wang, R. W. Schoenlein, L. A. Peteanu, R. A. Mathies and C. V. Shank, *Science* **266,** 422 (1994).

[2] A. Warshel, *Nature* **260,** 679 (1976).

[3] O. Weingart, *J. Am. Chem. Soc.* **129,** 10618 (2007).

[4] S. Hayashi, E. Taikhorshid and K. Schulten, *Biophys. J.* **96,** 403 (2009).

[5] L. M. Frutos, T. Andruniow, F. Santoro, N. Ferre and M. Olivucci, *Proc. Natl. Acad. Sci. U.S.A.* **104,** 7764 (2007).

Appendix C
Raman Intensity Calculations

C.1 RRModel Tutorial

A. Introduction

Resonance Raman spectroscopy is a powerful tool in the study of molecules that undergo fast excited-state photochemistry. While the Raman peak frequencies and linewidths originate from a molecule's ground-state vibrational structure, the peak intensities contain information about the excited electronic states. This is because in resonance Raman spectroscopy, the intermediate or "virtual" states in the scattering event are the excited electronic states. Thus, the Raman peak intensities serve as a very sensitive probe of the structure and dynamics of the resonant electronic state.

Resonance Raman intensity analysis can be used to model the individual vibronic displacements that make up the Franck-Condon absorption and Raman excitation profiles, as well as provide information regarding the geometric evolution of a molecule immediately after excitation. The RRModel program calculates the absorption spectrum and resonance Raman intensities of a molecule using Heller's time-dependent formalism [1]. The absorption profile is given by

$$\sigma_A(E_L) = \frac{4\pi e^2 M^2 E_L}{6\hbar^2 cn\theta(2\pi)^{1/2}} \int_0^\infty dE \times \exp\left[\frac{-(E-E_0)^2}{2\theta^2}\right] \int_{-\infty}^{\infty} dt \langle i | i(t)\rangle e^{-\Gamma_G^2 t^2/\hbar^2} e^{i(E_L+\varepsilon_i)t/\hbar} \tag{C.1}$$

where M is the transition length, E_L is the incident photon energy, E_0 is the zero-zero transition energy, Γ_G is the Gaussian homogeneous linewidth, θ is the Gaussian inhomogeneous broadening, $|i\rangle$ is the initial ground-state vibrational wavefunction, and

$|i(t)\rangle = e^{-iHt/\hbar}|i\rangle$ is this initial wavefunction propagated for time t on the excited-state potential surface. The corresponding expression for the Raman cross-sections is

$$\sigma_R(E_L, E_S) = \frac{8\pi E_S^3 E_L e^4 M^4}{9\hbar^6 c^4 \theta (2\pi)^{1/2}} \int_0^\infty dE \times \exp\left[\frac{-(E-E_0)^2}{2\theta^2}\right] \left| \int_0^\infty dt \langle f | i(t) \rangle e^{-\Gamma_G^2 t^2/\hbar^2} e^{i(E_L+\varepsilon_i)t/\hbar} \right|^2 \quad \text{(C.2)}$$

where E_S is the energy of the scattered photon, and $|f\rangle$ is the final excited vibrational level on the ground-state potential surface [2]. Note that the homogeneous broadening can also be modeled as a Lorentzian lineshape if the $e^{-\Gamma_G^2 t^2/\hbar^2}$ term is replaced with $e^{-\Gamma|t|/\hbar}$. In the time-dependent picture of the Raman cross-section, the relationship between the resonance Raman intensities and excited-state dynamics is evident. Those modes with intense Raman lines correspond to the vibrational coordinates along which the electronically excited molecule distorts rapidly.

The source code for the program (RRModel.f) is written in Fortran 77, and was provided by Anne Myers Kelley of UC Merced. The program requires an input file titled rrmodel.txt, and the necessary parameters and format are defined below. Assuming short-time dynamics, the integrated Raman peak intensity of each mode is proportional to $\omega^2\Delta^2$, where ω is the vibrational frequency and Δ is the unitless normal mode displacement. To start, the relative Δ's should be estimated and the magnitude of the delta values should be adjusted to fit the overall width of the absorption spectrum; delta values that are too large will result in a calculated absorption profile that is too broad, while small delta values underestimate the breadth. Next, E_0 and M are adjusted to fit the peak frequency and amplitude, respectively, of the experimental absorption spectrum. Altering these parameters does not affect the shape of the calculated profile – adjusting E_0 simply shifts the spectrum to higher or lower frequency, and altering M changes the overall amplitude. The inhomogeneous broadening parameter (θ) determines the degree of vibronic structure present in the calculated absorption profile, with lower θ resulting in sharper vibronic transition features. The homogeneous broadening parameter (Γ), whose upper limit is constrained by the absolute Raman cross-sections, is then adjusted to match the red edge of the absorption spectrum. Iterative adjustment of these parameters is performed until a good fit is obtained for both the absorption spectrum and the Raman cross-sections.

B. Creating an Input File

To run RRModel, an input file titled rrmodel.txt must first be created. Listed first are the parameters that are needed for the calculation.

nmode = total number of vibrational modes (50 max)
nline = number of Raman lines to calculate (35 max)
ntime = number of time steps in the Fourier transform (5000 max)
bcut = smallest relative Boltzmann factor to consider in the thermal sum
iprof = 1 to print out full profiles; 0 for discrete points only
cutoff = cutoff parameter in the sum over n in the Brownian oscillator calculation; usually in the range of 10^{-6} to 10^{-8} (check convergence by reducing the cutoff and re-running)
$\mathbf{E_0}$ = zero-zero electronic transition energy (cm^{-1})
gamma = electronic homogeneous linewidth (FWHM in cm^{-1}). Using the correct Brownian oscillator calculation this does not give the exact FWHM; just consider it a parameter
rkappa = unitless lineshape parameter in the stochastic model (>>1 is Lorentzian, <<1 is Gaussian)
glife = homogeneous linewidth (HWHM in cm^{-1}) from the exponential lifetime decay
sig = electronic inhomogeneous width, q (Gaussian standard deviation in cm^{-1})
u = electronic transition length at equilibrium geometry, M (Å)
alow, ahigh = the lowest and highest energies (in cm^{-1}) of the calculated absorption profile
delt = time step in Fourier transform (fs); typically 0.5 to 1.0
refrac = solvent refractive index, n
efreq = array of excitation energies (cm^{-1}) used to calculate the Raman spectrum;
wg = array of ground-state vibrational frequencies (cm^{-1}) for the first (nmode–1) modes
we = array of excited-state frequencies for these modes
delta = array of dimensionless displacements for these modes
du = array of (du/dq)/u0 for these modes (i.e., the ratio of vibronically induced to allowed transition moments)
wlow = the vibrational frequency of the last, thermally populated mode
delow = dimensionless displacement of this mode
dudq = (du/dq)/u0 in this thermally populated mode
temp = temperature in Kelvin
nquanta(i,j) = the number of quanta excited in mode j in Raman line i
ibroad = 0 for Gaussian, 1 for Lorentzian inhomogeneous lineshape

The format for the rrmodel.txt file is as follows. This file can be created in any text editor.

nmode, nline, ntime, nfreq, bcut, iprof
sig, cutoff, temp, ibroad, gchar
E_0, gamma, rkappa, u, glife
alow, ahigh, delt, refrac
efreq array
wg, we, delta, du
nquanta

As an example, the input file for Mark Trulson's CHD data [3] is as follows:

12, 12, 2500, 1, 1, 1
0, 1.e-8, 295, 0, 0
34100, 1700, 0.1, 0.67, 1
32000, 45000, 0.5, 1.45
38865
507, 507, 0.51, 0.00
557, 557, 0.36, 0.00
750, 750, 0.23, 0.00
948, 948, 0.37, 0.00
1014, 1014, 0.24, 0.00
1057, 1057, 0.23, 0.00
1150, 1150, 0.34, 0.00
1237, 1237, 0.39, 0.00
1321, 1321, 0.85, 0.00
1404, 1404, 0.22, 0.00
1435, 1435, 0.09, 0.00
1578, 1578, 1.91, 0.00

wg, we, delta, du
(for each of the 12 modes)

1,0,0,0,0,0,0,0,0,0,0,0
0,1,0,0,0,0,0,0,0,0,0,0
0,0,1,0,0,0,0,0,0,0,0,0
0,0,0,1,0,0,0,0,0,0,0,0
0,0,0,0,1,0,0,0,0,0,0,0
0,0,0,0,0,1,0,0,0,0,0,0
0,0,0,0,0,0,1,0,0,0,0,0
0,0,0,0,0,0,0,1,0,0,0,0
0,0,0,0,0,0,0,0,1,0,0,0
0,0,0,0,0,0,0,0,0,1,0,0
0,0,0,0,0,0,0,0,0,0,1,0
0,0,0,0,0,0,0,0,0,0,0,1

nquanta
(for each of the 12 modes)

From the above file, we can see that there were 12 vibrational modes (nmode) and 12 Raman lines (nline) calculated at 295 K. The zero-zero electronic transition energy (E_0) is 34,100 cm^{-1}, which is the value that provided the best match for the experimental and calculated absorption peak frequencies. The electronic homogeneous linewidth (Γ) is 1700 cm^{-1}, and 0 cm^{-1} of inhomogeneous broadening (θ) was included. The parameter rkappa is 0.1, indicating a Gaussian lineshape, and the electronic transition length (M) is 0.67 Å. The absorption spectrum was calculated over a range of 32,000 – 45,000 cm^{-1}, and the efreq array parameter is 38,865 cm^{-1} (equivalent to the excitation wavelength, λ_{ex} = 257.3 nm).

Following these initial parameters is a list of (wg, we, delta, du) for each calculated Raman line. In this calculation, it was approximated that the ground and excited state potentials are harmonic and differ only in their equilibrium positions (thus, wg = we for each mode). This approximation can be relaxed, if necessary, to allow for excited state frequency changes.

C. Running RRModel in OS X:

Step 1: Create a working directory.

Create a folder on the desktop titled RRModel (this folder can be placed in a different location, but for the sake of clarity I am putting it on the desktop for this tutorial). Place the source code RRModel.f and the input file rrmodel.txt into this folder. Also, include text files for the experimental absorption spectrum (column 1: frequency in cm^{-1}; column 2: absorption cross-section in $Å^2$) and Raman spectrum (column 1: Raman shift in cm^{-1}; column 2: absolute Raman cross-section in $Å^2$). Within the context of this tutorial, I will refer to these files as 'ExpAbsorption' and 'ExpRaman', respectively.

Step 2: Compile the program.

Before the program can be executed, it needs to be compiled. A compiler is a computer program that transforms a source code (i.e., RRModel.f) that is written in some computer language (i.e., Fortran 77) into machine code format, which is basically a set of instructions that the computer can read and execute (binary code). The compiler I use for this program is g77, which is a GNU Fortran compiler. g77 is no longer maintained by the GNU Project, and has been replaced by gfortran as the compiler for newer versions of Fortran, yet I still recommend using g77 to compile the current RRModel.f code (because I know it works!). For Mac OS X users, this compiler can be downloaded from SourceForge, which is a resource for open source software development and distribution. The g77 binary can be downloaded at hpc.sourceforge.net. To compile the RRModel program, open a terminal (/Applications/Utilities/Terminal) and at the prompt type **cd Desktop/RRModel** [ENTER], then **g77 RRModel.f** [ENTER].

```
dhcp-128-32-246-81:~ katelynspillane$ cd Desktop/RRModel
dhcp-128-32-246-81:RRModel katelynspillane$ g77 RRModel.f
dhcp-128-32-246-81:RRModel katelynspillane$
```

This will create an executable file named a.out in the directory containing the RRModel.f file (in our case, in the RRModel folder on the desktop). Execution of a.out will produce a summary file (raman.out), the calculated absorption spectrum (absorp.dat), and Raman excitation profiles (profxx) in the RRModel folder.

Step 3: Install Gnuplot.

I use Gnuplot as my graphing utility. While any graphing program can be used (i.e., Excel), I find that Gnuplot is the most convenient to use in this case because it is command-line driven. In order to use Gnuplot, first install AquaTerm (a Mac OS X graphics terminal) from http://sourceforge.net/projects/aquaterm/. Next, install Gnuplot from http://gnuplot.sourceforge.net and compile using the instructions listed in the ReadMe file.

Step 4: Do the calculation.

1) Open a terminal (/Applications/Utilities/Terminal) and at the prompt, type **cd Desktop/RRModel**. cd is a Unix command that means 'change directory'; thus, in this step we are changing the active directory to the RRModel folder on the desktop (/Users/Desktop/RRModel).

2) At the prompt, type **./a.out**. This executes the a.out program. Once complete, an absorption spectrum (absorp.dat), the Raman excitation profiles for each mode (profxx), and a summary file (raman.out) are created in the RRModel folder. The 'raman.out' file includes the differential cross-section of each mode (in units of 1.E–11 $Å^2$).

```
dhcp-128-32-246-81:~ katelynspillane$ cd Desktop/RRModel
dhcp-128-32-246-81:RRModel katelynspillane$ ./a.out
dhcp-128-32-246-81:RRModel katelynspillane$
```

3) Convert the differential Raman cross-sections to absolute Raman cross-sections. This can be done using the equation

$$\sigma_R = \frac{8\pi}{3}\frac{(1+2\rho)}{(1+\rho)}\left(\frac{\partial\sigma}{\partial\Omega}\right)$$

where ρ is the depolarization ratio. Save the calculated Raman absolute cross-sections (column 1: Raman shift in cm^{-1}; column 2: cross-sections in $Å^2$) as a text file titled 'CalcRaman' in the RRModel folder on the desktop.

4) Open a second terminal. Once again, change the active directory to /Users/Desktop/RRModel (**cd Desktop/RRModel**).

5) At the prompt, type **gnuplot**. At the next prompt, type **set term aqua**.

6) Type **plot 'absorp.dat' with lines, 'ExpAbsorption' with lines**. This plots the experimental and calculated absorption spectra in the same window. Multiple spectra can be plotted simultaneously by entering the file names, indicated separately by quotation marks and separated by a comma, after the plot command. Note that these files must be in the same active directory in order to be plotted together.

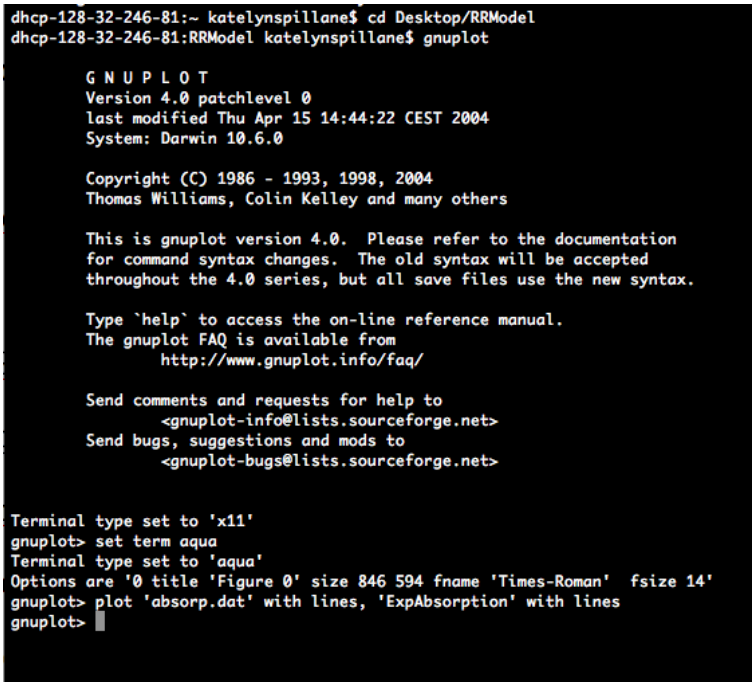

7) Open a third terminal. Once again, change the active directory to /Users/Desktop/RRModel. At the prompt, type **gnuplot**. At the next prompt, type **set term aqua**.

8) Type **plot 'CalcRaman', 'ExpRaman'**. This plots the experimental and calculated Raman absolute cross-sections in the same window.

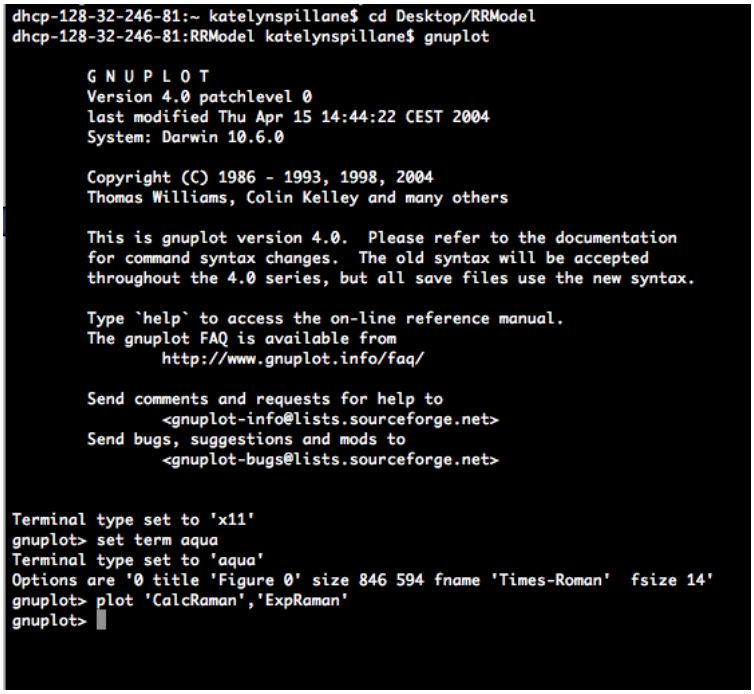

9) Adjust the parameters of rrmodel.txt iteratively and repeat steps 2–8 until satisfactory fits are found for both the absorption spectrum and the Raman cross-sections.

D. Running RRModel in Windows:

Before the program can be run, it needs to be compiled. A compiler is a computer program that transforms a source code (i.e., RRModel.f) that is written in some computer language (i.e., Fortran 77) into a machine code format, which is basically a set of instructions that the computer can read and execute (binary code). The compiler I use for this program is g77, which is a GNU Fortran compiler. g77 is no longer maintained by the GNU Project, and has been replaced by gfortran for newer versions of Fortran, yet I still recommend using g77 to compile the current RRModel.f code. For Windows users, g77 can be downloaded as part of Cygwin (www.cygwin.com; click 'Install Cygwin now' in the upper right corner of the screen). The g77 compiler is not included in Cygwin by default. When installing Cygwin (www.cygwin.com), click the View button in the Select Packages screen and change the view to full. Scroll down to "gcc-g77:Fortran compiler" and click on the little double arrow next to "skip" until you see 3.4.4-3. It should select automatically any uninstalled dependent packages. Click next to install.

Because Cygwin is a Unix emulator, the installation directory (by default, c:/cygwin) is the *root* of the Unix-like file system, which contains bni, etc, home, tmp, and usr directories as would be found on a GNU/Linux or other Unix system. In order to run the program, the source code (RRModel.f) needs to be in the same directory as

Cygwin. I find it easiest to create a new folder titled RRModel, within this directory, which contains the source code and input file rrmodel.txt. Once RRModel.f is compiled, the executable file will be placed in this folder, as will all output files that are produced. The RRModel folder should also include text files for the experimental absorption spectrum (column 1: frequency in cm^{-1}; column 2: absorption cross-section in $Å^2$) and Raman spectrum (column 1: Raman shift in cm^{-1}; column 2: absolute Raman cross-section in $Å^2$). Within the context of this tutorial, I will refer to these files as 'ExpAbsorption' and 'ExpRaman', respectively.

I use Gnuplot as my graphing utility. While any graphing program can be used (i.e., Excel), I find that Gnuplot is the most convenient to use in this case because it is command-line driven. Install Gnuplot from http://gnuplot.sourceforge.net and compile using the instructions listed in the ReadMe file.

The step-by-step instructions to run RRModel with a Windows system are as follows:

1) Open Cygwin.

2) Type **RRModel**. This makes the RRModel folder your active directory.

3) The first time the program is run, it needs to be compiled. Type **g77 RRModel.f**. This compiles the RRModel program and creates an executable file named a.exe in the RRModel folder.

4) Prepare an input file titled rrmodel.txt using the parameters and format defined above.

5) Because a.exe takes its input parameters from rrmodel.txt, these files must both be in the same directory (the RRModel folder within the Cygwin directory).

6) Type **./a**. This executes the program. Once complete, an absorption spectrum (absorp.dat), the Raman excitation profiles for each mode (profxx), and a summary file (raman.out) are created in the RRModel folder. The 'raman.out' file includes the differential cross-section of each mode (in units of 1.E–11 $Å^2$).

7) Convert the differential Raman cross-sections to absolute Raman cross-sections. This can be done using the equation

$$\sigma_R = \frac{8\pi}{3}\frac{(1+2\rho)}{(1+\rho)}\left(\frac{\partial\sigma}{\partial\Omega}\right)$$

where ρ is the depolarization ratio. Save the calculated Raman absolute cross-sections as a text file titled 'CalcRaman'.

8) Open a second terminal. Once again, change the active directory to /Cygwin/RRModel (**cd Cygwin/RRModel**).

9) At the prompt, type **gnuplot**.

10) Type **plot 'absorp.dat' with lines, 'ExpAbsorption' with lines**. This plots the experimental and calculated absorption spectra in the same window. Multiple spectra can be plotted simultaneously by entering the file names, indicated separately by quotation marks and separated by a comma, after the plot command. Note that these files must be in the same active directory in order to be plotted together.

11) Open a third terminal. Once again, change the active directory to /Cygwin/RRModel. At the prompt, type **gnuplot**

12) Type **plot 'CalcRaman', 'ExpRaman'**. This plots the experimental and calculated Raman absolute cross-sections in the same window.

13) Adjust the parameters of rrmodel.txt iteratively and repeat steps 4–12 until satisfactory fits are found for both the absorption spectrum and the Raman cross-sections.

C.2 RRModel Source Code (written in Fortran 77)

```
program rrmodel
c
c     Program to calculate Raman and absorption intensities using time-dependent
c          method, including excited-state frequency changes or coordinate dependence
c          of the transition moment, and three thermally populated modes (which may
c          also have both a frequency change and coord dependence). Uses Mukamel's
c          Brownian oscillator model for the solvent induced broadening (identical to
c          stochastic model for real part of broadening function, but with imaginary part
c          which gives solvent Stokes shift). The formula correct when not in the high
c          temperature limit is used. All deltas and dudqs are in ground-state
c          dimensionless coordinates.
c
c     Inputs (read from file "rrmodel.txt"):
c     nmode = total # vibrational modes (50 max)
c     nline = # Raman lines to calculate (35 max)
c     ntime = # time steps in Fourier transform (5000 max)
c     bcut = smallest relative Boltzmann factor to consider in thermal sum
c     iprof = 1 to print out full profiles; 0 for discrete points only
c     cutoff = cutoff parameter in the sum over n in Brownian oscillator calc,
c          usually 10^-6 to 10^-8 range (check convergence by reducing cutoff and re-
c          running)
c     e0 = electronic zero-zero energy
c     gamma = electronic homogeneous linewidth (FWHM in cm^-1).  Using correct
c          Brownian oscillator calculation, this doesn't give exact FWHM; just
c                    consider it a parameter
c          rkappa = lineshape parameter in stochastic model (>>1 is Lorentzian, <<1 is
c          Gaussian)

c          glife = homogeneous HWHM (cm^-1) from exponential lifetime decay
c     sig = electronic inhomogeneous width (Gaussian standard dev. in cm^-1)
c     u = electronic transition length at equilibrium geometry (Å)
c     alow,ahigh = lowest and highest energies (cm^-1) to calc. absorption
c     delt = time step in Fourier transform (fs), typically 0.5 to 1.0
c     refrac = solvent refractive index
c     efreq = array of excitation energies (cm^-1) to calculate Raman spectrum
c     wg = array of ground state vib. freqs (cm^-1) for first (nmode-1) modes
c     we = array of excited-state frequencies for these modes
c     delta = array of dimensionless displacements for these modes
c     du = array of (du/dq)/u0 for these modes (i.e. ratio of vibronically induced to
c                    allowed transition moment)
c     wlow = vib. frequency of last, thermally populated mode
c     delow = dimensionless displacement of this mode
c     dudq = (du/dq)/u0 in thermally populated mode
c     temp = temperature in Kelvin
```

```
c     nquanta(i,j) = # of quanta excited in mode j in Raman line i

c          ibroad = 0 for Gaussian, 1 for Lorentzian inhomogeneous lineshape
c

c          Outputs:

c          Input parameters and Raman intensities (differential cross-sections) at

c                    specific excitation frequencies in raman.out

c          Absorption spectrum in absorp.out

c          Raman excitation profile (diff. cross section in units of 1.E–11 Å**2) for xx line

c                    in profxx

c
      implicit complex (c)
      dimension wg(35),we(35),delta(35),du(35),
     1  covlp(35,5,2500),ceiwt(2500),covlp2(3,3,3,2500)
      dimension covlpq(35,3,2500)
      dimension coswt(2500),csinwt(2500),cqt(2500),cpt(2500),
     1  cat(2500),cgt(2500),toverh(2500)
      dimension spectrum(1000,50),xfreq(1000),nquanta(50,35),
     1  xs(1000),efreq(20),ffunc(1000),gfunc(1000),pfunc(501),rshift(50)
      dimension ifreq(20),cdamp(2500),espect(20,50)
      double precision vs(2500),vsi,arg,cutoff,einc,vn,dex,ainc,gchar

           character*4 base

           character*2 numb(50)
      data pi/3.14159/ci/(0.,1.)/spectrum/50000*0./hbar/5308.8/
      data xs/1000*0./boltz/0.695/sq2/0.707107/sq32/1.224745/
      data espect/1000*0./base/'prof'/

           data numb/'01','02','03','04','05','06','07','08','09',

     1'10','11','12',

     2'13','14','15','16','17','18','19','20','21','22','23','24',

     3'25','26','27','28','29','30','31','32','33','34','35',

     4'36','37','38','39','40','41','42','43','44','45','46',
```

```
     5'47','48','49','50'/
c
c     input parameters
c
      open(unit=30,name='rrmodel.txt',type='old')
      read (30,*) nmode,nline,ntime,nfreq,bcut,iprof
      read (30,*) sig,cutoff,temp,ibroad,gchar

           if(bcut.ge.1.) bcut=1.
      if(nmode.gt.35) nmode=35
      if(nline.gt.50) nline=50
      if(ntime.gt.2500) ntime=2500
      if(nfreq.gt.20) nfreq=20

           if(gchar.ge.1.) gchar=1
      read (30,*) e0,gamma,rkappa,u,glife
      read (30,*) alow,ahigh,delt,refrac
      read (30,*) (efreq(i),i=1,nfreq)
      read (30,*) (wg(i),we(i),delta(i),du(i),i=1,nmode)
      do 40 i=1,nline
 40        read (30,*) (nquanta(i,j),j=1,nmode)
      close(unit=30)
c
c     print parameters
c
      open(unit=31,name='raman.out')

           write (31,*) ' # time steps, Boltzmann cutoff, T'

      write (31,*) ntime,bcut,temp

           if(ibroad.eq.0) write (31,*) ' Gaussian inhomog. lineshape used'

           if(ibroad.ne.0) write (31,*) ' Lorentzian inhomog. lineshape used'

           write (31,*) ' Inhom. width, Brownian cutoff'

      write (31,333) sig,cutoff

           write (31,*) ' e0, gamma, kappa, trans. length, exp decay width'

           write (31,333) e0,gamma,rkappa,u,glife

           write (31,*) ' Time step, refractive index'

      write (31,333) delt,refrac
```

```
          write (31,*) ' wg, we, delta, du/dq'

      write (31,333) (wg(i),we(i),delta(i),du(i),i=1,nmode)

          write (31,*) ' # of quanta in each mode in each line'

          do i=1,nline

                    write (31,*) (nquanta(i,j),j=1,nmode)

                    end do

c

c

      pre = 2.08e-20*1.e-6*delt**2*0.3/pi
      if(iprof.eq.0.and.sig.ne.0.) iprof=2

          do i=nmode-2,nmode
        du(i) = -du(i)
        delta(i) = delta(i)*sqrt(we(i)/wg(i))

                    end do
      delth = delt/hbar
      beta = 1./(boltz*temp)
      do 50 i=1,ntime
 50       toverh(i) = (i-1)*delth
c
c         Calculate vibrational stuff for both excited states
c         Brownian oscillator first
c
        do 55 i=1,ntime
 55         vs(i) = 0.
        rk2 = rkappa**2
        a = (2.355+1.76*rkappa)/(1.+0.85*rkappa+0.88*rk2)
        rlamb = rkappa*gamma/a
        reorg = beta*(rlamb/rkappa)**2/2.
        v = 2.*pi/beta
        n = 0
 510     n = n + 1
        vn = v*n*1.d0
        ainc=vn*delth
        arg=-1.d0
        einc=dexp(-ainc)
```

```
      dex=1.d0
      denom = vn*(vn**2-rlamb**2)
      ii = 0
      do 530 i=2,ntime
        arg = arg+ainc
        dex = dex*einc
        vsi = (dex+arg)/denom
        if(n.eq.1) go to 520
        if(dabs(vsi/vs(i)).gt.cutoff) ii=1
520       vs(i) = vs(i) + vsi
530       continue
      if(ii.ne.0.or.n.eq.1) go to 510
      vpre = 4.*reorg*rlamb/beta
      rpre = (reorg/rlamb)/tan(rlamb*beta/2.)
      do 60 i=1,ntime
         rlambt = rlamb*toverh(i)
         damp = 1. - exp(-rlambt) - rlambt
         rdamp = -rpre*damp + vpre*vs(i) + glife*toverh(i)
60        cdamp(i) = conjg(cexp(-rdamp+ci*reorg*damp/rlamb))
c
c       Now undamped oscillators
c


          do i=1,3

          im = nmode - 3 + i
      call dukomp(wg(im),we(im),delta(im),delth,ntime,5,3,
     1       du(im),covlp,ceiwt,covlp2,i)

                          end do
      do 100 i=1,nmode-3
        if(wg(i).eq.we(i)) call simpov(i,delth,ntime,

     1              wg,delta,covlp,ceiwt,covlpq)
        if(wg(i).ne.we(i)) call kompov(i,delth,ntime,

     1             wg,we,delta,covlp,ceiwt,coswt,csinwt,cqt,

     2             cpt,cat,cgt,toverh)
        do 850 j=1,ntime
        ct1 = du(i)*sq2*(covlp(i,2,j)+covlpq(i,1,j))
        ct2 = du(i)*(covlp(i,3,j)+sq2*covlp(i,1,j)+sq2*
     1              covlpq(i,2,j))
        ct3 = du(i)*(sq32*covlp(i,4,j)+covlp(i,2,j)+sq2*
     1              covlpq(i,3,j))
        covlp(i,1,j) = covlp(i,1,j) + ct1
```

```
          covlp(i,2,j) = covlp(i,2,j) + ct2
 850        covlp(i,3,j) = covlp(i,3,j) + ct3
 100        continue
c
c     Set up the time integrals
c
        do i=1,ntime
          cat(i)=u**2*cexp(-ci*(e0+reorg)*toverh(i))*cdamp(i)
        end do
c
c         Set up inhomogeneous broadening
c
      part = 0.
      xfreq(1) = alow
      xinc = (ahigh-alow)/999.
      do 166 k=2,1000
 166      xfreq(k) = xfreq(k-1) + xinc
      pfunc(1) = 0.
      do 605 i=2,501
 605     pfunc(i) = pfunc(i-1) + xinc
      if(sig.eq.0.) go to 620

          if(ibroad.eq.0) then
                  deno = 2.*sig**2
                  do 610 i=1,501
 610                      pfunc(i) = exp(-pfunc(i)**2/deno)

          end if

          if(ibroad.eq.1) then

                  deno = sig**2

                  do 611 i=1,501

 611                      pfunc(i) = deno/(pfunc(i)**2 + deno)

          end if

          if(ibroad.gt.1) then

             deno = 2.*sig**2

                  gpre = 1./(sig*sqrt(2.*pi))

                  ppre = sig/pi
```

```
                do 612 i=1,501

612                     pfunc(i) = gchar*gpre*exp(-pfunc(i)**2/deno) +

   1                ppre*(1-gchar)/(pfunc(i)**2 + (deno/2))

          end if


c
c     Loop over all Raman lines to calculate. ceiwt is product of overlaps.
c
620   do 290 i1=1,3

          do 290 i2=1,3

          do 290 i3=1,3
       ei = (i1-1)*wg(nmode-2)+(i2-1)*wg(nmode-1)+(i3-1)*wg(nmode)
       weight = exp(-ei*beta)

           if(weight.lt.bcut) go to 289
       part = part + weight
       do 288 j=1,nline
         do 130 k=1,ntime
130           ceiwt(k) = (1.,0.)
         rshift(j) = 0.
         do 140 k=1,nmode-3
           kk = nquanta(j,k)+1
           do 150 l=1,ntime
150           ceiwt(l)=ceiwt(l)*covlp(k,kk,l)
140        rshift(j) = rshift(j) + (kk-1)*wg(k)
         kk1 = nquanta(j,nmode-2)+1

                  kk2 = nquanta(j,nmode-1)+1

                  kk3 = nquanta(j,nmode)+1
         rshift(j) = rshift(j) + (kk1-1)*wg(nmode-2)

         1                + (kk2-1)*wg(nmode-1) + (kk3-1)*wg(nmode)
         do 155 k=1,ntime
155         ceiwt(k) = ceiwt(k)*cat(k)*covlp2(1,i1,kk1,k)

    1              *covlp2(2,i2,kk2,k)*covlp2(3,i3,kk3,k)
c
c     Loop over 1000 excitation frequencies
```

```
c
            if(iprof.eq.0) go to 200
          do 180 k=1,1000
            csum=0.5*ceiwt(1)
            cinc = cexp(ci*(ei+xfreq(k))*delth)
            cold = (1.,0.)
c
c     Do time integral by simple sum (rectangle rule)
c
            do 170 l=2,ntime
              cold = cold*cinc
 170            csum= csum + cold*ceiwt(l)

                          sigma = csum*conjg(csum)
c
c     Calculate total crossections (k-th - excitation freq.,
c           j-th Res. Raman mode)
c
 180          spectrum(k,j)=sigma*weight + spectrum(k,j)
              go to 288
 200          do 280 k=1,nfreq
                csum = 0.5*ceiwt(1)
                cinc = cexp(ci*(ei+efreq(k))*delth)
                cold = (1.,0.)
                do 270 l=2,ntime
                                cold = cold*cinc
 270                            csum = csum + cold*ceiwt(l)
                sigma = csum*conjg(csum)
 280            espect(k,j) = sigma*weight + espect(k,j)

 288                continue

 289                continue
 290        continue
c
c     Convolve with Gaussian inhomogeneous distribution
c

           pre = pre/part
           if(iprof.eq.0) go to 310
      do 700 i=1,nline
         do 710 j=1,1000
 710     ffunc(j) = spectrum(j,i)
         call convl(ffunc,pfunc,gfunc,1000,501,sig)
         do 720 j=1,1000
 720     spectrum(j,i)=pre*gfunc(j)*xfreq(j)*(xfreq(j)
```

```
     1              -rshift(i))**3
 700      continue
      do i=1,nfreq
         do j=1,999
       aa = (xfreq(j+1)-efreq(i))*(xfreq(j)-efreq(i))
       if(aa.lt.0.) then
          efreq(i) = xfreq(j)
          ifreq(i) = j
          end if
        end do
         end do
           go to 319
 310     do 315 i=1,nline
             do 315 j=1,nfreq
 315               espect(j,i)=pre*efreq(j)*(efreq(j)-rshift(i))**3
     1                       *espect(j,i)
c
c     Print out spectra
c
 319  write (31,*) ' Raman shift and sum of intensities'

          do i=1,nline
      sumint=0.
      do j=1,nfreq
      if(iprof.ne.0) sumint=sumint+spectrum(ifreq(j),i)
           if(iprof.eq.0) sumint=sumint+espect(j,i)
      end do
      write(31,*) rshift(i),sumint
      end do
      do 340 i=1,nfreq
         write(31,320) efreq(i)
 320  format(' exc.freq ',f10.3)

                   if(iprof.eq.0) go to 321

                   write (31,*) ' Relative intensities'
         write(31,333) (100.*spectrum(ifreq(i),j)/
     1         spectrum(ifreq(i),1),j=1,nline)

                   write (31,*) ' Absolute differential cross sections'
         write(31,330) (spectrum(ifreq(i),j)*1.e11,j=1,nline)

                   go to 340
 321               write (31,*) ' Relative intensities'

                   write(31,333) (100.*espect(i,j)/espect(i,1), j=1,nline)
```

```
                write (31,*) ' Absolute differential cross sections'
                write(31,330) (espect(i,j)*1.e11,j=1,nline)
 330  format(6e11.3)
 331  format(f8.1,3x,e11.3)
 333  format(6f11.3)
 340     continue
c
c     Print out profiles
c

          close (unit=31)
      if(iprof.ne.1) go to 352
      do 350 i=1,nline

                open (unit=31+i,name=base//numb(i))
        write (31+i,342) rshift(i)
 342     format(f10.3,' cm-1')
        write (31+i,341) (xfreq(j),spectrum(j,i)*1.e11,j=1,1000)
 341     format(1x,f11.3,5x,f11.4)
 350     close (unit=31+i)
c
c     Calculate absorption spectrum
c

 352  pre2 = 5.745e-3*1.e-3*delt/(refrac*part)
      do 452 i1=1,3

          do 452 i2=1,3

          do 452 i3=1,3
        ei = (i1-1)*wg(nmode-2)+(i2-1)*wg(nmode-1)+(i3-1)*wg(nmode)
        weight = exp(-ei*beta)

                if(weight.lt.bcut) go to 451

                weight = weight*pre2
        do 410 k=1,ntime
 410        ceiwt(k) = cat(k)*covlp2(1,i1,1,k)*covlp2(2,i2,1,k)

    1           *covlp2(3,i3,1,k)
        do 420 k=1,nmode-3
          do 420 l=1,ntime
 420          ceiwt(l) = ceiwt(l)*covlp(k,1,l)
        do 450 k=1,1000
          csum = 0.5*ceiwt(1)
```

```
          cinc = cexp(ci*(ei+xfreq(k))*delth)
          cold = (1.,0.)
            do 440 l=2,ntime
              cold = cold*cinc
 440            csum = csum+cold*ceiwt(l)
            sigma = abs(real(csum))
            sigma = sigma*weight
 450        xs(k) = sigma + xs(k)

 451              continue

 452              continue
      call convl(xs,pfunc,gfunc,1000,501,sig)
      do 730 j=1,1000
 730      xs(j) = gfunc(j)*xfreq(j)
      open(unit=31,name='absorp.dat')
c      write (31,470) 1.,0.
      do 731 i=1,1000
 731  write (31,470) xfreq(i),xs(i)
 470  format(2f21.14)
      close(unit=31)
      stop
      end
c
c
      subroutine convl(f,p,g,nf,np,sig)
c
c     calculates the convolution of f with p and returns result in g
c
      dimension f(nf),p(np),g(nf)
c
      if(sig.eq.0.) go to 500
      pmult = p(1)
      sum = pmult
      do 100 i=1,nf
 100      g(i) = f(i)*pmult
      do 300 j=1,np-1
         pmult = p(j+1)
         if(pmult.lt.1.e-5) go to 350
         do 200 k=1,nf
        kmj = k - j
        if(kmj.gt.0) g(k)=g(k)+pmult*f(kmj)
        kpj = k + j
 200     if(kpj.le.nf) g(k)=g(k)+pmult*f(kpj)
 300      sum = sum + 2.*pmult
 350  do 400 i=1,nf
```

```
 400      g(i) = g(i)/sum
      return
 500  do 510 i=1,nf
 510      g(i) = f(i)
      return
      end
c
c
c
      subroutine simpov(n,delth,ntime,wg,delta,covlp,ceiwt,covlpq)
c
c     Calculates time-dependent overlap for mode with equal ground and
c     excited state frequency
c
      implicit complex (c)
      dimension wg(35),delta(35),covlp(35,5,2500),ceiwt(2500)
      dimension covlpq(35,3,2500)
      data ci/(0.,1.)/sq2/0.7071/sq6/2.44949/
c
      s = delta(n)**2/2.
      sqrts = -sqrt(s)
      cinc = cexp(-ci*wg(n)*delth)
      ceiwt(1) = (1.,0.)
      do 10 i=2,ntime
 10       ceiwt(i) = ceiwt(i-1)*cinc
c
c     Calculate <0|0(t)> through <4|0(t)>
c
      do 30 i=1,ntime
         ce = ceiwt(i)
         ce1 = 1. - ce
         ct = cexp(-s*ce1)
         covlp(n,1,i)=cexp(-s*(1.-ceiwt(i)))
         covlp(n,2,i)=sqrts*(ceiwt(i)-1.)*covlp(n,1,i)
         covlp(n,3,i)=sq2*s*(ceiwt(i)-1.)**2*covlp(n,1,i)
         covlp(n,4,i)=-s*sqrts*(1.-ceiwt(i))**3
     1         *covlp(n,1,i)/sq6
         covlpq(n,1,i)=covlp(n,2,i)
         covlpq(n,2,i)=(ce+s*ce1**2)*ct
         covlpq(n,3,i)=-(s+ce1**3+2.*ce*ce1)*ct*sqrts*sq2
 30       covlp(n,5,i)=s**2*(1.-ceiwt(i))**4/(2.*sq6)
      return
      end
c
c
c
```

```
      subroutine kompov(n,delth,ntime,wg,we,delta,covlp,

     1          ceiwt,coswt,csinwt,cqt,cpt,cat,cgt,toverh)
c
c     Calculates time-dependent overlap for non-Duschinsky rotated mode
c     with different ground and excited state frequencies.  Negative ex.
c     state frequency is interpreted as imaginary freq.
c
      implicit complex(c)
      dimension wg(35),we(35),delta(35),covlp(35,5,2500),

     1     ceiwt(2500)
      dimension coswt(2500),csinwt(2500),cqt(2500),cpt(2500),
     1  cat(2500),cgt(2500),toverh(2500)
      data ci/(0.,1.)/pi/3.14159/sq2/1.414/sq3/1.73205/sq6/2.44949/
c
      s = -delta(n)
      wwg = wg(n)
      ww = we(n)
      if(ww.ge.0.) go to 100
c
c     Calculate coswt and sinwt for imaginary w
c
         einc = exp(-ww*delth)
         einc2 = exp(ww*delth)
         cqt(1) = (1.,0.)
         ceiwt(1) = (1.,0.)
         do 20 i=2,ntime
        cqt(i) = cqt(i-1)*einc
 20     ceiwt(i) = ceiwt(i-1)*einc2
         do 30 i=1,ntime
        coswt(i) = 0.5*(cqt(i)+ceiwt(i))
 30     csinwt(i) = ci*0.5*(cqt(i)-ceiwt(i))
         cwwe = -ci*ww
         go to 200
c
c     Calculate coswt and sinwt for real w
c
 100  einc = cos(ww*delth)
      einc2 = sin(ww*delth)
      coswt(1) = (1.,0.)
      csinwt(1) = (0.,0.)
      do 120 i=2,ntime
         coswt(i) = einc*coswt(i-1)-einc2*csinwt(i-1)
 120      csinwt(i) = einc2*coswt(i-1)+einc*csinwt(i-1)
      cwwe = (1.,0.)*ww
```

```
c
c     Calculate q(t) [cqt], p(t) [cpt], a(t) [cat], part of g(t) [cgt]
c
 200  do 230 i=1,ntime
         cqt(i) = s*(1.-coswt(i))
         cpt(i) = s*cwwe*csinwt(i)/wwg
         cat(i) = -0.5*(ci*coswt(i)-cwwe*csinwt(i)/wwg)*ci
         cat(i) = cat(i)/(ci*csinwt(i)*wwg/cwwe + coswt(i))
         cgt(i) = ci*cat(i)*cqt(i)**2 - 0.5*cpt(i)*(cqt(i)+s)
         if(ww.gt.0.) cgt(i)=cgt(i)+0.5*toverh(i)*cwwe
c
c     Put det(z) into coswt array
c
 230      coswt(i) = coswt(i)+ci*csinwt(i)*wwg/cwwe
      nphase = 0
      rxold = 1.
      do 250 i=1,ntime
c
c     Evaluate ln(det z) and add to g(t)
c
         realx = real(coswt(i))
         realy = aimag(coswt(i))
         thet = atan(realy/realx)
         if(realx/rxold.lt.0.) nphase=nphase+1
         rxold=realx
         cinc = ci*0.25*(alog(realx**2+realy**2))
         cinc = cinc - 0.5*thet - 0.5*pi*nphase
         cgt(i)= cgt(i) + cinc
c
c     Calculate p prime and a
c
         cpt(i) = cpt(i) - 2.*ci*cat(i)*cqt(i)
         cat(i) = cat(i) + 0.5
c
c     Calculate overlaps <0|0(t)> through <4|0(t)>
c
         cinc = cexp(ci*cgt(i)-cpt(i)**2*0.25/cat(i))
         covlp(n,1,i) = cinc/csqrt(cat(i))
         covlp(n,2,i) = -ci*cpt(i)*covlp(n,1,i)/(cat(i)*sq2)
         cinc = (cpt(i)/cat(i))**2
         cinc = cinc + 2.*(1.-1./cat(i))
         covlp(n,3,i) = -0.5*cinc*covlp(n,1,i)/sq2
         cinc = cpt(i)/cat(i)
         cinc = cinc*(cinc**2/6. + 1. - 1./cat(i))
         covlp(n,4,i) = ci*sq3*cinc*covlp(n,1,i)/2.
         cinc = (cpt(i)/cat(i))**2
```

```
        cinc = cinc**2 + 12.*cinc*(1.-1./cat(i))
        cinc = cinc + 12.*(1.-1./cat(i))**2
        covlp(n,5,i) = covlp(n,1,i)*cinc/(8.*sq6)
 250     continue
      return
      end
c
c
c
c

          subroutine dukomp(wg,we,delta,delth,ntime,nmax,nocc,

          1         dudq,covlp,ceiwt,covlp2,iw)
c
      implicit complex (c)
      double precision cherm(12,2500)
      dimension covlp(35,5,2500),ceiwt(2500),covlp2(3,3,3,2500)
      dimension ceiwt2(2500),cf(2500),cg(2500),cpsi(2500),ca(2500),
     1     c0(2500),cesum(2500)
      dimension ssinwt(2500)
      data ci/(0.,1.)/
c
c
      rat = sqrt(we/wg)
      wp = we + wg
      wm = we - wg
      rat2 = 2.*we/wg
      crat4 = ci*((we/wg)**2 - 1.)
      psipre = 0.25*wp**2/(we*wg)
      psirat = (wm/wp)**2
c
      cinc1 = cexp(-ci*we*delth)
      cinc3 = cinc1**2
      ceiwt(1) = (1.,0.)
      ceiwt2(1) = (1.,0.)
      delta2 = delta**2
      do i=2,ntime
         ceiwt(i) = ceiwt(i-1)*cinc1
         ceiwt2(i) = ceiwt2(i-1)*cinc3
         end do
      do i=1,ntime
         ssinwt(i) = aimag(ceiwt(i))
         end do
c
      do i=1,ntime
```

```
        cf(i) = -(wg*(1.-ceiwt(i)))/(wp-wm*ceiwt(i))
        cg(i) = (rat2+crat4*ssinwt(i))/(rat2-crat4*ssinwt(i))
        cal = (wm-wp*ceiwt(i))/(2.*wp-2.*wm*ceiwt(i))
        cph = psipre*(1.-psirat*ceiwt2(i))
        cph = 1./cph
        cpsi(i) = csqrt(cph)
        ca(i) = csqrt(cal)
        c0(i) = cpsi(i)*cexp(delta2*cf(i))
        cesum(i) = rat*cf(i)*delta/ca(i)
        end do
c
      call hermit(cesum,cherm,nmax+nocc+1,ntime)
      do 300 i=1,4
         ii = i-1
         do 290 j=1,6
       do l=1,ntime
          covlp(j,i,l) = (0.,0.)
          end do
       jj = j - 1
       ij = ii + jj
       pre = 1./sqrt(fact(ii)*fact(jj)*2.**ij)
       kstar = ij/2
       do 280 k=1,kstar+1
          kk = k-1
          prek = fact(2*kk)/fact(kk)
          prek = pre*prek*eta(jj,ii,kk)
          do 275 l=1,ntime
             cadd = prek*c0(l)
             cadd = cadd*ca(l)**ij
             cadd = cadd*cg(l)**kk
             cadd = cadd*cherm(ij-2*kk+1,l)
             covlp(j,i,l)=covlp(j,i,l)+cadd
 275           continue
 280        continue
 290     continue
 300      continue
      d1 = dudq/sqrt(2.)
      d2 = d1**2
      do 350 i=1,3
         si = sqrt(float(i-1))
         sip = sqrt(float(i))
         do 350 jj=1,3
       j = jj + i - 1
       sf = sqrt(float(j-1))
       sfp = sqrt(float(j))
       do 350 k=1,ntime
```

```
          cadd = (0.,0.)
          cad2 = (0.,0.)
          if(j.gt.1) cadd=sf*covlp(j-1,i,k)
          if(i.gt.1) cadd=cadd+si*covlp(j,i-1,k)
          cadd=cadd+sfp*covlp(j+1,i,k)+sip*covlp(j,i+1,k)
          if(i.gt.1.and.j.gt.1) cad2=sf*si*covlp(j-1,i-1,k)
          if(j.gt.1) cad2=cad2+sf*sip*covlp(j-1,i+1,k)
          if(i.gt.1) cad2=cad2+si*sfp*covlp(j+1,i-1,k)
          cad2=cad2+sfp*sip*covlp(j+1,i+1,k)
 350        covlp2(iw,i,jj,k)=covlp(j,i,k)+d1*cadd+d2*cad2

c

          return
      end
c
c
c
      function fact(n)
c
      rn = float(n)
      fact = 1.
      if(n.le.1) return
      do i=2,n
         fact = fact*i
         end do
      return
      end
c
c
c
      function eta(jj,ii,kk)
c
      eta = 0.
      do i=1,2*kk+1
         iq = i-1
         eta = eta + comb(jj,2*kk-iq)*comb(ii,iq)*(-1)**iq
         end do
      return
      end
c
c
c
      function comb(m,l)
c
      if(l.gt.m) comb = 0.
```

```
      if(l.le.m) comb = fact(m)/(fact(l)*fact(m-l))
      return
      end
c
c
c
      subroutine hermit(carg,cherm,n,ntime)
c
      implicit complex (c)
      dimension carg(2500)
      double precision cherm(12,2500)
c
      do i=1,ntime
         ca = carg(i)
         cherm(1,i) = (1.d0,0.d0)
         cherm(2,i) = 2.d0*ca
         do j=2,n-1
       cherm(j+1,i) = 2.*ca*cherm(j,i) - 2.*(j-1)*cherm(j-1,i)
       end do
         end do
      return
      end
c
```

C.3 References

[1] S. Y. Lee and E. J. Heller, *J. Chem. Phys.* **71,** 4777 (1979).

[2] A. B. Myers and R. A. Mathies, in *Biol. App. of Raman Spectroscopy*; T. G. Spiro, Ed. (John Wiley & Sons, New York, 1987), Vol. 2, p. 1-58.

[3] M.O. Trulson, G. D. Dollinger and R. A. Mathies, *J. Chem. Phys.* **90,** 4274 (1989).

Appendix D
Pigment Preparation

Rod Outer Segment (ROS) Isolation Buffers:

1. <u>1 L MOPS Buffer, pH 7.4</u>
   4.20 g MOPS
   0.17 g $CaCl_2 \cdot (H_2O)_2$
   0.10 g EDTA
   0.77 g DTT (5 mM) — DTT is a reducing agent that breaks disulfide bonds and should be replenished every ~3 weeks (although it is best to make fresh buffer for each prep).

   Combine to make ~950 mL of solution in Milli-Q water. Check the pH with a calibrated pH meter – the 950 mL solution should have a pH of ~3.4. Add KOH solution to bring the pH up to 7.4 (to make the KOH solution, add ~25 KOH pellets to 150 mL Milli-Q water). Use dilute (1M) HCl to adjust the pH if necessary. Fill with Milli-Q water to 1 L.

2. <u>35% sucrose in MOPS (HiSu)</u>
   140 g sucrose
   260 g MOPS buffer

3. <u>22% sucrose in MOPS (LoSu)</u>
   55 g sucrose
   195 g MOPS buffer

ROS Purification Buffers:

1. <u>1 L column start buffer</u>
   0.7 g imidazole
   30 mL Ammonyx-LO
   Bring to pH 7 with 1M HCl.

2. <u>30 mM phosphate buffer (buffer A)</u>
   1.07 g Na_2HPO_4
   0.9 g NaH_2PO_4 (*not* hydrate $NaH_2PO_4 \cdot H_2O$)
   16.5 mL Ammonyx-LO
   Bring to 500 mL with Milli-Q water.
   (check pH before use: 6.86)

3. <u>150 mM phosphate buffer (buffer B)</u>
   5.35 g Na_2HPO_4
   4.5 g NaH_2PO_4 (*not* hydrate $NaH_2PO_4 \cdot H_2O$)
   16.5 mL Ammonyx-LO
   Bring to 500 mL with Milli-Q water.
   (check pH before use: 6.86)

Rhodopsin Regeneration Buffer:

<u>500 mL 100 mM phosphate buffer (buffer C)</u>
3.55 g Na_2HPO_4
3.00 g NaH_2PO_4 (*not* hydrate $NaH_2PO_4 \cdot H_2O$)
500 mL Milli-Q water
0.39 g DTT (5 mM)
(check pH before use: 7)

ROS Isolation

1. Begin ROS preparation

a) Thaw 2 cups of retinas (50 retinas per cup) by placing the cups into room temperature water (~1 hour).

b) Distribute the 2 cups of thawed retinas into 12 centrifuge tubes and add equal volume of high sucrose. The total volume should be ~15 mL per tube (~1/4 full).

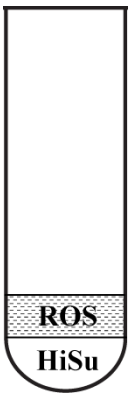

c) Cap the tubes and vortex for 90 seconds each. (Isolate the vortex mixer from any analytical balances, i.e., place on a stool, since vibrations during vortexing can damage the balance.)

This is a *very* important step as it directly affects the final rhodopsin yield. The solution must be vortexed well – it should mix to the top of the tubes. *Keep tubes on ice when not being vortexed.*

d) After the 12 tubes have been vortexed, pour the contents of 4 tubes evenly into the 8 remaining tubes. Rinse the 4 tubes with high sucrose and add this to the 8 tubes as well. Fill and balance the 8 tubes with high sucrose. Shake the tubes a few times and spin for 30 minutes at 6000 rpm (Sorvall floor centrifuge, SS34 rotor).

e) ROS floats in the high sucrose solution and will be stuck to the tube wall opposite the pellet. ROS is in the supernatant and cell debris + ROS are in the pellet.

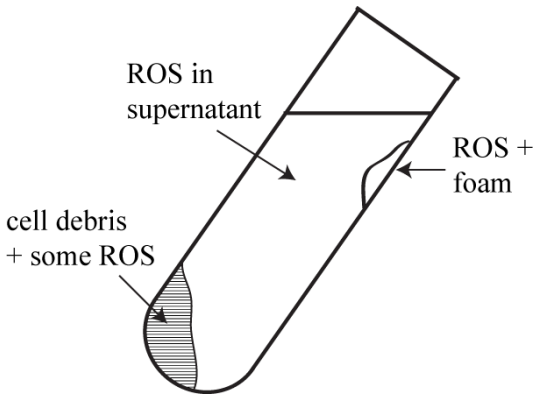

Scrape the foam with a rubber policeman; do not disturb the pellet. Pour the supernatant of the 8 tubes into 12 tubes. Dilute the supernatant 1:1 with MOPS buffer. Balance and spin the first set of 6 tubes at 18000 rpm for 20 minutes. Repeat for the second set of 6 tubes.

f) If necessary, the 8 tubes of pellets can be re-suspended in high sucrose for a second vortex, or combined into 4 tubes and stored at -80°C for vortexing at a later time. When you are ready to start the 2nd vortex, go back to step c.

g) After spinning, ROS will be in a pellet. Pour out the supernatant without disturbing the pellet. Check the supernatant in white light to make sure that all the ROS has been spun down; the supernatant will be pink/peach in color.

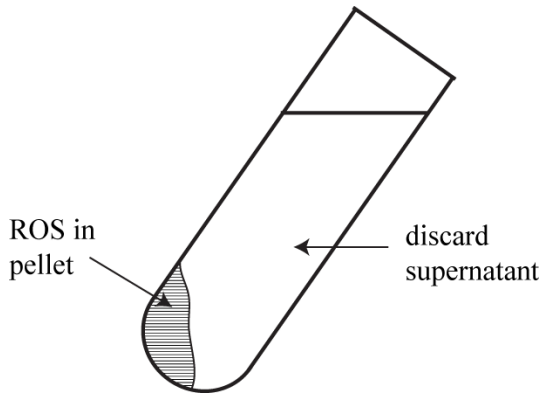

Scrape the bottom of each of the 12 tubes with a rubber policeman and collect the pellets into 4-6 tubes – the pellet volume should be no more than 15 mL per tube. Fill these tubes with MOPS buffer and spin at 18000 rpm for 20 minutes.

h) Discard the supernatant (pale pink/yellow in color) and combine the pellets into 2-3 tubes. Spin these tubes at 18000 rpm for 20 minutes.

i) Discard the supernatant and collect the pellets into 1 tube. If the volume is too large to collect into 1 tube, collect into 2 tubes. Fill with MOPS buffer and repeat the spin (18000 rpm for 20 minutes). Discard supernatant. Repeat until the supernatant is clear.

j) At this point there should be two ROS pellets – one from the first vortex and one from the second vortex. Keep them separate, as they will be loaded onto separate sucrose gradients. Store at -80°C until ready to load onto gradients.

2. Sucrose gradient

Prepare 6 sucrose gradients for each pellet. This should be done in the dark room at 4°C.

Prepare the ultracentrifuge: Place the SW28 rotor into the ultracentrifuge and cool the chamber + rotor to 4°C. This process can be expedited by storing the rotor at 4°C when not in use.

Prepare the gradients: Put a clear ultracentrifuge tube (capacity 38 mL) into each of the 6 rotor buckets and cool the containers. With all valves closed, pour 16.5 mL of LoSu into the left reservoir and 16.5 mL of HiSu into the right reservoir. Turn on the stirrer and open the LoSu valve – there should be swirls of LoSu being mixed into the HiSu solution. If not, tilt the gradient mixer to remove any air bubbles that may be trapped between the two reservoirs. Open the main valve and establish a drop speed of 1 drop/second using an external tubing clamp. The sucrose solution should run along the side of the tube, not drip directly into it. Each tube requires ~15 minutes to fill.

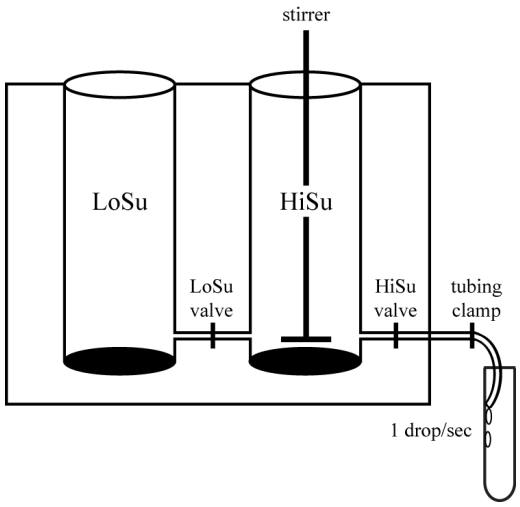

Density gradient:

a) Thaw the pellet and vortex briefly, for ~30 seconds. Divide the pellet among the 6 gradients. Pour the solution slowly over the sucrose gradient with a plastic pipette, along the side of the tube. Be careful not to disturb the gradient. Use ~5 mL of LoSu to rinse the tube after the pellet has been loaded and add this to the gradients as well. Use LoSu to balance the buckets to within +/- 0.01 g. Do not overload the gradients – the 6 ultracentrifuge tubes can accommodate a total of <20 mL of ROS. Otherwise, you will not get a good separation. Spin in the ultracentrifuge at 4°C, 25000 rpm, for 2.5 hours.

b) After centrifugation, there should be 3 bands.

Density gradient from the 1st vortex

The 3 bands should be distributed as follows:

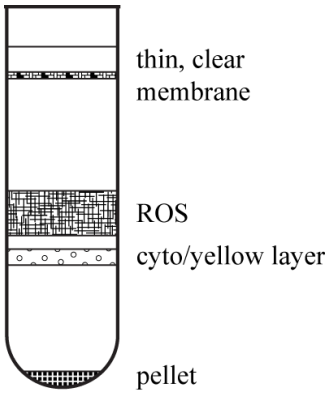

Discard the top layer with a short glass pipette, making sure that the last pipette of waste prior to starting on the ROS band is clear. Place the pipette into the middle of the ROS band and collect this layer. Collect as much as possible without pulling from the cyto band.

Density gradient from the 2nd vortex

The 3 bands should be distributed as follows:

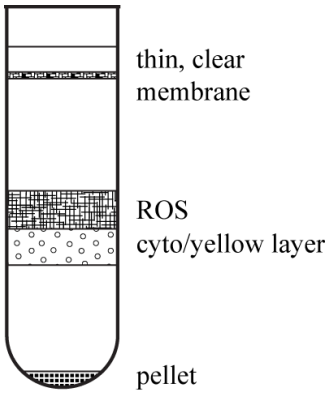

After discarding the clear top layer, begin pulling the ROS band without disturbing the cyto layer. It is very important not to pull any material from the cyto layer because it contains proteins that directly affect the pre- and post-column purity. Be conservative – it is better to have a loss in yield in order to maximize purity.

Collect the ROS bands from the sucrose gradients into 3-6 tubes and dilute 1:1 with MOPS buffer. Spin in the Sorvall at 15000 rpm for 25 minutes. Pour off the supernatant, which should be clear. Store pellets at -80°C overnight.

Solubilization

NOTE: IF YOU PLAN TO REGENERATE WITH RETINAL ANALOGS, DO NOT SOLUBILIZE THE ROS PELLET AT THIS POINT!!! SKIP TO THE NEXT PAGE.

1. Lyse Cells

a) Thaw ROS pellets from day 1 (~1/2 hour). Leave the pellets in the 3-6 tubes, add ice cold Milli-Q water and suspend the ROS with a rubber policeman. Vortex briefly. Spin for 45 minutes at 18000 rpm to lyse cells. Check the supernatant – it should be clear. Spin longer if necessary.

b) Collect the 3-6 pellets into 1 centrifuge tube and add ice cold water again. Suspend the pellet and vortex briefly. Spin for at least 45 minutes at 18000 rpm. Again, make sure everything is spun into a pellet. Remove the clear supernatant – it is best to leave as small a pellet as possible.

2. Solubilize

a) Add Ammonyx-LO to the tube with the lysed pellet and put in a small magnetic stir bar. Ideally the final solution should contain <30% Ammonyx-LO, i.e., 5 mL Ammonyx-LO into 10 mL of ROS. Stir overnight at 4°C at LOW speed to solubilize the material. There should be minimum turbulence and air bubbles.

b) Measure an absorption spectrum of the sample to check the yield. Ideally there should be ~90-110 OD·mL total from the 2 vortexes. Note the absolute OD and the R value (OD_{280}/OD_{500}). If R is very large (>4), the post-column purity will also be large (>2). If R is small (<3), the post-column yield should be optimal (1.7-2). A second indication of sample purity is the ratio OD_{400}/OD_{500}, which ideally should be 0.17-0.2 post-column.

The sample is now ready to be loaded onto the column.

Pigment Regeneration

1. Lyse cells

a) Thaw ROS pellets from day 1 (~1/2 hour). Leave the pellets in the 3-6 tubes, add ice cold Milli-Q water and suspend the ROS with a rubber policeman. Vortex briefly. Spin for 45 minutes at 18000 rpm to lyse cells. Check the supernatant – it should be clear. Spin longer if necessary.

b) Collect the 3-6 pellets into 1 centrifuge tube and add ice cold water again. Suspend the pellet and vortex briefly. Spin for at least 45 minutes at 18000 rpm. Again, make sure everything is spun into a pellet. Remove the clear supernatant – it is best to leave as small a pellet as possible.

2. Regeneration

Make a stock solution of retinal in dry benzene, which can be stored under dry nitrogen at -80°C.

a) Suspend pellet in exactly 25 mL of buffer C. Suspend pellet and vortex briefly.

b) Determine ROS yield:

- Vortex ROS/buffer solution for ~90 seconds. Take a 200 μL aliquot of the ROS/buffer solution and suspend in ~15 mL of buffer C.
- Spin at 18000 rpm for 30 minutes. Remove clear supernatant.
- Dissolve pellet in 3 mL 30% Ammonyx-LO.
- Measure absorption spectrum and determine yield.

c) Add 100 μL 1M hydroxylamine to the ROS/buffer solution. Vortex for ~30 seconds.

d) Bleach in ambient light, for ~1 hour.

- Measure an absorption spectrum to ensure no residual absorbance at 500 nm. There should be an absorption band at 365 nm.

e) Spin for 30 minutes at 18000 rpm. Remove clear supernatant.

f) Wash pellet with 25 mL buffer C. Vortex briefly. Spin at 18000 rpm for 30 minutes. Remove clear supernatant.

g) Wash pellet again with 25 mL buffer C. Vortex briefly. Spin at 18000 rpm for 30 minutes. Remove clear supernatant.

h) Suspend pellet in exactly 25 mL buffer C. Vortex briefly.

i) Add a 3-4 molar excess of retinal analog by first removing the benzene under a stream of dry nitrogen and then dissolving in not more than 100 μL ethanol. Vortex briefly.

j) Regenerate by stirring at low speed at 4°C overnight (or at room temperature for 90 minutes).

3. Calculate regeneration yield

a) Take a 200 μL aliquot of the regenerated mixture and suspend in ~15 mL of buffer C.

b) Spin at 18000 rpm for 30 minutes. Remove clear supernatant.

c) Dissolve pellet in 3 mL 30% Ammonyx-LO.

d) Measure absorption spectrum and determine regeneration yield.

4. Solubilize

a) Spin the regenerated mixture at 18000 rpm for 30 minutes. Remove clear supernatant.

b) Loosen pellet with rubber policeman and add Ammonyx-LO. Put in a small magnetic stir bar. Ideally the final solution should contain <30% Ammonyx-LO, i.e., 4 mL Ammonyx-LO into 10 mL of pellet. Stir overnight at 4°C at LOW speed to solubilize the material. There should be minimum turbulence and air bubbles.

The sample is now ready for the column.

ROS Purification

Pour the hydroxyappatite column

Measure the appropriate amount of hydroxyapatite (HA) beads using the following guide:

<40 OD•mL: ~11 g HA beads

40-60 OD•mL: ~12 g HA beads

60-80 OD•mL: ~13 g HA beads

80-100 OD•mL: ~14 g HA beads

a) The yellow Bio-Rad econo-column has a capacity of ~120 mL. Weigh 11-14 g of HA and pour it into 150 mL of start buffer under SLOW and GENTLE swirling. Do not use a stirring rod as this will destroy the beads. Let it settle for at least 10 minutes and decant the clear supernatant. Add 150 mL start buffer and repeat. Swirl the remaining beads and pour into the column in the dark room refrigerator (use a funnel with a wide mouth and do this in a single motion to prevent channels from forming within the column). Let the column settle. Once it has settled ~1 inch, let it settle completely under low flow of start buffer (1 drop per 3 seconds). Do this until the HA beads no longer move downward. NEVER LET THE COLUMN GO DRY. Once the HA beads are packed, check to make sure there are no channels in the column.
b) Wash the column with 125 mL start buffer (<1 drop/second) using a peristaltic pump or gravity. The pump is a much more reliable method since it maintains a constant flow rate.

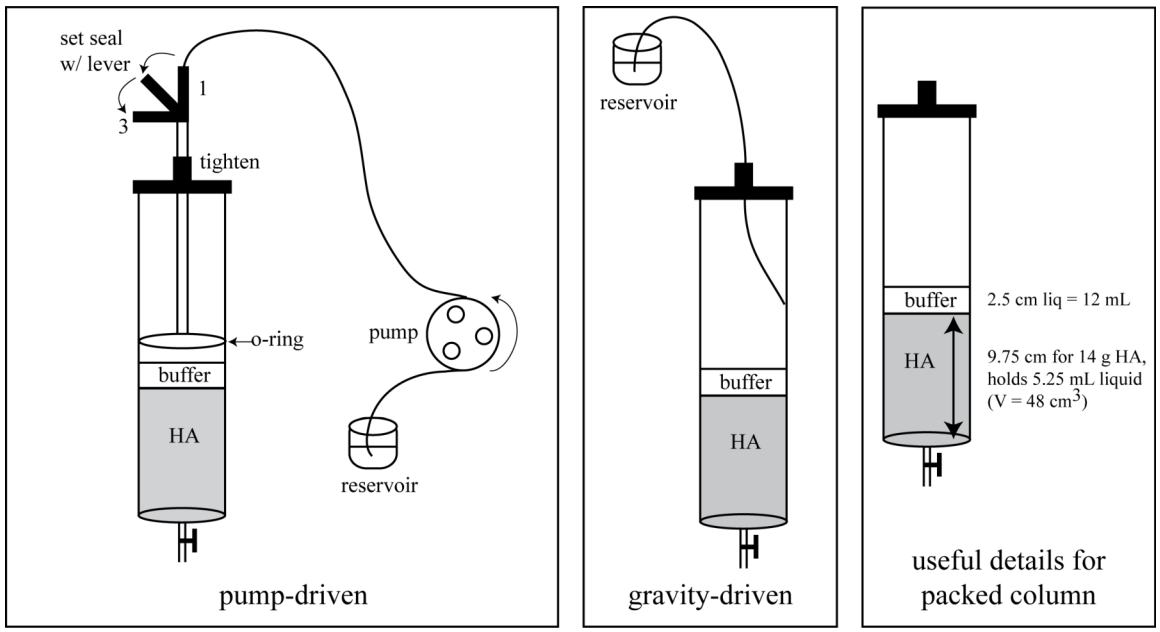

To use the pump, position the O-ring portion of the flow tube adapter to the appropriate location in the column (~2 mm above liquid), tighten the knob to lock the O-ring position and pull the lever down from position 1 to position 3 to set the O-ring seal. Once the seal is set, open the stopcock completely and confirm that there is no leak, i.e., buffer should not drip from the column. When the seal has been confirmed, start the pump and set it to the drip rate of <1 drop/second to wash the beads with start buffer.

c) After 125 mL has passed through the column, let the start buffer drain until there is only ~3 mm of liquid on top of the HA beads. If you are going to leave the column in the refrigerator overnight, leave at least 1 inch of start buffer on top of the beads.

Load ROS onto column

a) Slowly add the solubilized ROS along the side of the column, using a glass pipette. Let the ROS solution drain VERY SLOWLY (<1 drop per 3 seconds). Close the exit when there is ~4 mm liquid on top of the HA beads. Add a layer (1 inch) of start buffer on top and let this layer also drain.

b) Add another 1 inch of start buffer onto the HA beads and connect the column to the buffer A reservoir (150 mL). Collect 4 mL fractions at a rate of ~1 drop/second. I collect the fractions into 13 × 100 mm disposable test tubes. Collect 16 fractions. Change the reservoir to buffer B and collect an additional 32 fractions. Measure an absorption spectrum of each tube – there will likely be two populations of rho, one

from the buffer A fractions and the other from the buffer B fractions. Pool the fractions based on purity.

c) You will likely collect 50-90 mL pure rho from the column. Concentrate the sample using Amicon centrifugal filter units, 10 kDa MWCO, to the desired OD.